

**VALIDATION OF TSUNAMI DESIGN
GUIDELINES FOR COASTAL BRIDGES**

Final Report

PROJECT TPF 5(307)



Oregon Department of Transportation

VALIDATION OF TSUNAMI DESIGN GUIDELINES FOR COASTAL BRIDGES

Final Report

PROJECT TPF 5(307)

by

Patrick Lynett - University of Southern California
Hong Kie Thio - AECOM
Michael Scott - Oregon State University
Tom Murphy - Modjeski & Masters`
Tom Shantz - CalTrans
Jian-Dzwan Shen - FHWA

for

Oregon Department of Transportation
Research Section
555 13th Street NE, Suite 1
Salem OR 97301

and

Federal Highway Administration
1200 New Jersey Avenue SE
Washington, DC 20590

January 2021

1. Report No. FHWA-OR-RD-21-09		2. Government Accession No.		3. Recipient's Catalog No.	
4. Title and Subtitle Validation of Tsunami Design Guidelines for Coastal Bridges				5. Report Date January 2021	
				6. Performing Organization Code	
7. Author(s) Patrick Lynett - https://orcid.org/0000-0002-2856-9405 Hong Kie Thio - https://orcid.org/0000-0002-9051-9601 Michael Scott - http://orcid.org/0000-0001-5898-5090 Tom Murphy - https://orcid.org/0000-0002-1474-9181 Tom Shantz - https://orcid.org/0000-0002-0534-3024 Jian-Dzwan Shen - https://orcid.org/0000-0001-6982-7290				8. Performing Organization Report No. TPF 5(307)	
9. Performing Organization Name and Address Oregon Department of Transportation Research Section 555 13 th Street NE, Suite 1 Salem, OR 97301				10. Work Unit No. (TRAIS)	
				11. Contract or Grant No.	
12. Sponsoring Agency Name and Address Oregon Dept. of Transportation Research Section 555 13 th Street NE, Suite 1 Salem, OR 97301				13. Type of Report and Period Covered Final Report	
				14. Sponsoring Agency Code Federal Highway Admin. 1200 New Jersey Avenue SE Washington, DC 20590	
15. Supplementary Notes Abstract: This paper details a Transportation Pooled Fund Study, TPF-5(307), that included Alaska, California, Hawaii, Oregon (lead state), Washington, and the Federal Highway Administration. The research goal was to update guidelines as a foundation for review by the respective AASHTO sub-committee(s). This report focused on bridges for the Western United States. Five major efforts were completed: <ol style="list-style-type: none"> 1. Updated probabilistic tsunami hazard mapping to include wave-heights, velocities, and inundation levels at the 1000-year recurrence interval. This was completed for all aforementioned states at varying detail (10m through 60m); 2. Uncertainties and bias between models were examined to find areas where they agree and potential areas where the study could identify conservative estimates for optimization. 3. Analysis of site-specific tsunami hazards was developed. Two methods (level 1 and level 2) are presented to detail local tsunami hydrodynamics; 4. Loading are detailed and recommendations for equations presented based on research findings. Three load cases, including conditions showing upward lift were modeled and equated. Bridge skew, slope, and super-elevation were examined. Debris was considered. 5. Geotechnical considerations were also discussed. 					
17. Key Words: Tsunami, tsunami loads, tsunami load calculations, tsunami loading on bridges			18. Distribution Statement: Copies available from NTIS, and online at www.oregon.gov/ODOT/TD/TP_RES/		
19. Security Classification (of this report) Unclassified		20. Security Classification (of this page) Unclassified		21. No. of Pages 133	22. Price

SI* (MODERN METRIC) CONVERSION FACTORS

APPROXIMATE CONVERSIONS TO SI UNITS					APPROXIMATE CONVERSIONS FROM SI UNITS				
Symbol	When You Know	Multiply By	To Find	Symbol	Symbol	When You Know	Multiply By	To Find	Symbol
<u>LENGTH</u>					<u>LENGTH</u>				
in	inches	25.4	millimeters	mm	mm	millimeters	0.039	inches	in
ft	feet	0.305	meters	m	m	meters	3.28	feet	ft
yd	yards	0.914	meters	m	m	meters	1.09	yards	yd
mi	miles	1.61	kilometers	km	km	kilometers	0.621	miles	mi
<u>AREA</u>					<u>AREA</u>				
in ²	square inches	645.2	millimeters squared	mm ²	mm ²	millimeters squared	0.0016	square inches	in ²
ft ²	square feet	0.093	meters squared	m ²	m ²	meters squared	10.764	square feet	ft ²
yd ²	square yards	0.836	meters squared	m ²	m ²	meters squared	1.196	square yards	yd ²
ac	acres	0.405	hectares	ha	ha	hectares	2.47	acres	ac
mi ²	square miles	2.59	kilometers squared	km ²	km ²	kilometers squared	0.386	square miles	mi ²
<u>VOLUME</u>					<u>VOLUME</u>				
fl oz	fluid ounces	29.57	milliliters	ml	ml	milliliters	0.034	fluid ounces	fl oz
gal	gallons	3.785	liters	L	L	liters	0.264	gallons	gal
ft ³	cubic feet	0.028	meters cubed	m ³	m ³	meters cubed	35.315	cubic feet	ft ³
yd ³	cubic yards	0.765	meters cubed	m ³	m ³	meters cubed	1.308	cubic yards	yd ³
~NOTE: Volumes greater than 1000 L shall be shown in m ³ .									
<u>MASS</u>					<u>MASS</u>				
oz	ounces	28.35	grams	g	g	grams	0.035	ounces	oz
lb	pounds	0.454	kilograms	kg	kg	kilograms	2.205	pounds	lb
T	short tons (2000 lb)	0.907	megagrams	Mg	Mg	megagrams	1.102	short tons (2000 lb)	T
<u>TEMPERATURE (exact)</u>					<u>TEMPERATURE (exact)</u>				
°F	Fahrenheit	(F-32)/1.8	Celsius	°C	°C	Celsius	1.8C+32	Fahrenheit	°F

*SI is the symbol for the International System of Measurement

ACKNOWLEDGEMENTS

The authors would like to thank the Oregon Department of Transportation (ODOT) for leading and contributing to this pooled-funded project. Other contributors to the pool fund include the Federal Highway Administration, Alaska DOT, Hawaii DOT, Washington DOT, and CalTrans. The author and team would like to thank all the Technical Advisory Committee (TAC) participants for their diligence, patience, and perseverance over this five year project. The team wants to recognize the passing of Dr Stephen Mahin during this project, which was a great loss to the team, community, and all who knew him.

DISCLAIMER

This document is disseminated under the sponsorship of the Oregon Department of Transportation and the United States Department of Transportation in the interest of information exchange. The State of Oregon and the United States Government assume no liability of its contents or use thereof.

The contents of this report reflect the view of the authors who are solely responsible for the facts and accuracy of the material presented. The contents do not necessarily reflect the official views of the Oregon Department of Transportation or the United States Department of Transportation.

The State of Oregon and the United States Government do not endorse products of manufacturers. Trademarks or manufacturers' names appear herein only because they are considered essential to the object of this document.

This report does not constitute a standard, specification, or regulation.

TABLE OF CONTENTS

EXECUTIVE SUMMARY	XI
1.0 PROBABILISTIC TSUNAMI HAZARD MAPS FOR THE WESTERN UNITED STATES.....	1
1.1 PROBABILISTIC TSUNAMI HAZARD ANALYSIS (PTHA) BASICS	2
1.2 EPISTEMIC UNCERTAINTY AND ALEATORY VARIABILITY	4
1.3 OVERVIEW OF THE PTHA METHODOLOGY.....	4
1.4 SOURCE CHARACTERISTICS	5
1.4.1 <i>Source geometry</i>	5
1.4.2 <i>Source complexity</i>	5
1.5 SPECIFIC SOURCES	5
1.5.1 <i>Cascadia subduction zone</i>	6
1.5.2 <i>Alaska subduction zone</i>	8
1.5.3 <i>Other sources</i>	8
1.6 TSUNAMI PROPAGATION MODELING	9
1.6.1 <i>Algorithms</i>	10
1.6.2 <i>Elevation models</i>	10
1.7 OFFSHORE TSUNAMI HAZARD.....	10
1.8 INUNDATION COMPUTATION	12
1.8.1 <i>Inundation scenario probabilities</i>	13
1.8.2 <i>On-land hazard curves</i>	15
1.9 INUNDATION GRIDS	15
2.0 QUANTIFICATION AND INCLUSION OF UNCERTAINTIES IN ONSHORE TSUNAMI PROPAGATION.....	19
2.1 BACKGROUND.....	19
2.2 METHODOLOGY: FIELD MEASUREMENTS AND OBSERVATIONS	19
2.3 METHODOLOGY: TSUNAMI MODELING.....	20
2.4 RESULTS: INTER-MODEL COMPARISON	22
2.5 MODEL VARIABILITY AND UNCERTAINTIES.....	27
2.6 SUMMARY AND MAIN CONCLUSIONS FROM MODEL COMPARISONS.....	31
3.0 EVALUATION OF SITE-SPECIFIC TSUNAMI HAZARD	33
3.1 METHODOLOGY: INUNDATION DATABASE.....	33
3.2 LEVEL 1 ANALYSIS: TRANSECT APPROACH.....	34
3.3 DEVELOPMENT OF TRANSECT CALCULATION TOOL.....	38
3.4 GENERAL CONFIGURATION GUIDELINES FOR LEVEL 2 ANALYSIS.....	40
3.5 ESTIMATION OF FLOW DIRECTION.....	41
3.6 RECOMMENDED LOAD CASES	42
3.7 SITE-SPECIFIC HAZARD DETERMINATION EXAMPLES: HAWAII	42
3.8 SITE-SPECIFIC HAZARD DETERMINATION EXAMPLES: ALASKA.....	44
3.9 SITE-SPECIFIC HAZARD DETERMINATION EXAMPLES: WASHINGTON	46
3.10 SITE-SPECIFIC HAZARD DETERMINATION EXAMPLES: OREGON	48
3.11 SITE-SPECIFIC HAZARD DETERMINATION EXAMPLES: CALIFORNIA.....	50
3.12 SUMMARY OF SITE-SPECIFIC HAZARD METHODOLOGY.....	52
4.0 LITERATURE REVIEW: TSUNAMI LOADING ON BRIDGES.....	53

4.1	EXPERIMENTAL DATA	53
4.2	NUMERICAL SIMULATION SOFTWARE	58
5.0	RECOMMENDATIONS FOR LOADING CALCULATIONS	61
5.1	NOMENCLATURE FOR LOAD EQUATIONS	61
5.2	LOAD CASES	62
5.2.1	<i>Load Case 1</i>	62
5.2.2	<i>Load Case 2</i>	63
5.2.3	<i>Load Case 3</i>	63
5.3	SUMMARY OF LOAD CASES.....	63
5.4	HORIZONTAL LOAD ESTIMATE.....	64
5.5	UPWARD LOAD ESTIMATE	65
5.6	DOWNWARD LOAD ESTIMATE.....	66
5.7	BRIDGE DECK ORIENTATION	67
5.7.1	<i>Skew</i>	67
5.7.2	<i>Superelevation</i>	69
5.7.3	<i>Slope</i>	70
5.8	DEBRIS71	
6.0	GEOTECHNICAL CONSIDERATIONS	73
6.1	DESIGN ISSUES	73
6.1.1	<i>Foundations and abutments</i>	73
6.1.2	<i>Approach embankments</i>	73
6.2	PERFORMANCE GOALS	74
6.3	FOUNDATION TYPE SELECTION	75
6.3.1	<i>Deep foundation</i>	75
6.3.2	<i>Shallow foundation</i>	75
6.4	LOAD CASES.....	75
6.5	EVALUATION OF FOUNDATION RESISTANCE	75
6.5.1	<i>Deep foundations</i>	75
6.5.2	<i>Shallow foundations</i>	76
6.6	SCOUR AND EROSION	77
6.7	RAPID DRAWDOWN.....	77
7.0	REFERENCES	79
	APPENDIX A: SOURCE CODE FOR MATLAB TRANSECT TOOL.....	A-1
	APPENDIX B: EXAMPLE BRIDGE LOADING CALCULATIONS	B-1
	APPENDIX C: DEFINITIONS AND NOTATIONS.....	C-1

LIST OF FIGURES

Figure 1.1:	Source-zones around the Pacific Ocean that are included in this work.	2
Figure 1.2:	Vertical displacement field (res=uplift) for two scenarios. Top is a full rupture earthquake, bottom is a partial rupture, each shown three times with different asperity locations. 6	
Figure 1.3:	Logic tree for the Cascadia subduction zone (adapted from the 2014 USGS National Seismic Hazard Map, Petersen et al., 2014). The smaller segmented ruptures have longer return	

times than the full rupture, and therefore the hazard in Cascadia is dominated by the full rupture model for most return periods.....	7
Figure 1.4: Segmentation models for the Alaska/Aleutian subduction zone (top) and the Japan/Kurile/Kamchatka subduction zone (bottom).....	9
Figure 1.5: 1000 yr offshore exceedance amplitudes for the five western states.	11
Figure 1.6: Source disaggregation for a site in southern California (top left), Hawaii (top right), Oregon (bottom left) and Washington (bottom right) showing the relative contributions to the hazard at those particular sites.	11
Figure 1.7: Comparison for the 2475 year Humboldt Bay probabilistic flow depth maps for a model using the full event set (Left) and only the far-field event set (right). The overall inundation pattern appears quite stable.	13
Figure 1.8: Schematic example of the relationship between the offshore hazard curve (blue line) and the probabilities of the reduce event set (circles, color coded according to source zone). Note that the event probability of the largest amplitude is equal to the exceedance probability of the offshore hazard curve.	14
Figure 1.9: Example of a 1000 yr map of flow depths for the Cannon Beach, OR, area. Resolution is 10m.....	16
Figure 1.10: Areas covered in this study. Blue outlines indicate 10m grids, red outlines indicate 60m grids.....	17
Figure 1.11: Example of time series (vertical amplitude, horizontal flow velocity) for a site in Oregon.....	18
Figure 2.1: Maximum tsunami amplitudes (m) predicted by MOST (left panel) and GeoClaw (right panel) in the Sendai plain.....	23
Figure 2.2: Comparison of runup height measurements and inundation line between data, MOST and GeoClaw during the 2011 Tohoku event in the Sendai plain.	24
Figure 2.3: Comparison of the runup heights probability density functions between the interpolated field data, MOST and GeoClaw models.	24
Figure 2.4: Estimated differences between field data runup heights and the topographic elevations from the numerical grid at the location of the runup measurement	25
Figure 2.5: Maximum flow velocities predicted by MOST (left panel) and GeoClaw (right panel).....	26
Figure 2.6: Comparison of maximum flow velocities at the Sendai plain between Koshimura and Hayashi (2012) measurements (gray triangles), MOST predictions (circles) and GeoClaw predictions (squares). The vertical bars on the model data provide the standard deviation of the predictions in the measurement window. At F2, two measurements were taken.....	26
Figure 2.7: (Top panel) Comparison between GeoClaw and MOST probability density functions of maximum shoreline flow velocities and (bottom panel) 1 meter depth maximum flow velocities at the Sendai plain.	27
Figure 2.8: Comparison of the runup heights probability density functions between the 4 different grid resolutions using MOST.	28
Figure 2.9: (Top panel) Comparison of the maximum shoreline flow velocities probability density functions and (bottom panel) 1 meter depth maximum flow velocities probability density functions between the 4 different grid resolutions using MOST.....	29
Figure 2.10: Mean flow velocity at different flow depths. The 6 meter flow depth corresponds approximately to the shoreline. The thick black line represents the calculated mean flow velocities using a Froude number of 1.	30

Figure 2.11: Inland maximum flow velocities across shore in the Sendai plain, (top panel) comparison of the average flow velocities between GeoClaw and the 4 different grid resolutions using MOST, (bottom left panel) comparison of peak flow velocities and (bottom right panel) comparison of standard deviations.....	30
Figure 3.1: Illustration of energy method across inundated transect; incident tsunami flow is from left to right (from Kriebel et al., 2017).....	38
Figure 3.2: EGL transect analysis example for a location in Hawaii.	43
Figure 3.3: EGL transect analysis example for a location in Alaska.	45
Figure 3.4: EGL transect analysis example for a location in Washington.....	47
Figure 3.5: EGL transect analysis example for a location in Oregon.....	49
Figure 3.6: EGL transect analysis example for a location in California.....	51
Figure 5.1: Variables that describe load estimation equations for deck-girder bridges.....	62
Figure 5.2: Three descriptors of bridge deck orientation: (a) superelevation, (b) skew, and (c) slope.	67
Figure 5.3: Plan view of skewed bridge analyzed by Motley et al (2016)]. Corners of the superstructure are identified: front acute (FA); front obtuse (FO); back acute (BA); and back obtuse (BO).....	68
Figure 5.4: Effect of skew angle on horizontal tsunami forces: (a) impact and (b) steady state. (Image from Motley et al (2016)).	68
Figure 5.5: Effect of skew angle on vertical tsunami forces: (a) uplift impact and (b) downward steady state. (Image from Motley et al (2016)).	69
Figure 5.6: Modification of total bridge force, compared to the non-skew case, based on skew angle: (a) horizontal force, (b) vertical force.....	70
Figure 5.7: Super elevation angle relative to tsunami flow: (a) negative; (b) positive.	70
Figure 5.8: Multiplier of total bridge force based on superelevation: (a) horizontal force, (b) uplift force, and (c) downward force.....	71
Figure 6.1: Tsunami induced foundation loading on a) deep foundations and b) shallow foundations.	73

LIST OF TABLES

Table 2.1: Field Data Measurements not used in this Study	22
Table 2.2: Average Inundation Distance from Field Measurements and Models	22
Table 4.1: Summary of Experiments for Validation of Numerical Simulation Models.	57
Table 5.1: Summary of Three Load Cases for Bore Attack on a Bridge Superstructure using Maximum Flow Speed and Flow Depth Determined from Site-specified PTHA.	63
Table 5.2: Coefficients for Steady State Horizontal Load Equation	64
Table 5.3: Coefficients for Horizontal Impact Load.....	65
Table 5.4: Coefficient C_1 for upward load equation.	65
Table 5.5: Coefficients for C_4 Clearance Factor in Upward Load Equation.....	66
Table 6.2: Design Requirements for Approach Embankments.	74

EXECUTIVE SUMMARY

Although the 2004 Indian Ocean tsunami exposed the vulnerability of coastal infrastructure in Southeast Asian countries, the 2011 Japan tsunami reinforced the fact that countries with well-designed coastal infrastructure and lifelines are at significant risk for damage and total loss from tsunami inundation. Geologic conditions similar to those found off the east coast of Japan are also present off the west coast of the United States. The Cascadia subduction zone (CSZ) poses a direct threat for a major tsunami that could impact the coastlines of Alaska, Hawaii, Canada, Oregon, Washington, and northern California. The CSZ last triggered an earthquake and subsequent tsunami about 400 years ago and has a high probability of unleashing a similar event in the next 100 years. Alaska and Hawaii have endured more recent tsunami events and remain at risk for future events. The design, protection, mitigation, and simulation of structures subjected to tsunami loading has thus been thrust to the forefront of structural engineering research.

Numerical models are a key component for methodologies used to estimate tsunami risk and model predictions are essential for the development of Probabilistic Tsunami Hazard Assessments (PTHA). By better understanding model bias and uncertainties and, if possible, minimizing them, a more reliable PTHA will result. In this study we compare runup height, inundation lines and flow velocity field measurements between GeoClaw and the Method of Splitting Tsunami (MOST) model predictions in the Sendai plain. Runup elevation and average inundation distance is in general over-predicted by the models. However, both models agree relatively well with each other when predicting maximum sea surface elevation and maximum flow velocities. Furthermore, to explore the variability and uncertainties in numerical models, MOST is used to compare predictions from 4 different grid resolutions (30m, 20m, 15m and 10m). Our work shows that predictions of statistically stable products (runup, inundation lines and flow velocities) do not require the use of high resolution (less than 30m) Digital Elevation Maps (DEMs) at this particular location. In addition, the Froude number variation in overland flow is presented. While it is noted that the results presented herein are specific to the models and areas tested, we find that

- Different models, with identical initial and boundary conditions, provide spatial-mean runup elevations to within 10% of each other
- Expected local errors in maximum overland flow velocity are likely to be in the range of 1-3 m/s, which for the data available equates to errors of 10-80% of the measured value
- Different models, with identical initial and boundary conditions, provide spatial-mean maximum speeds to within 30% of each other; however local correlation shows a variability on the same order as the error, or 10-80%.

The results provided in this paper will help understand the uncertainties in model predictions and locate possible sources of errors within a model.

For this project, a map of probabilistic offshore tsunami wave-heights at the 1000-year recurrence interval is created using a Green's function summation approach. This approach

enables the integration over a wide range of source zones and magnitudes and the inclusion of epistemic uncertainties that describe our incomplete knowledge and understanding of natural processes, and aleatory variability, which expresses the randomness in natural processes. The methodology is similar to the common approach in Probabilistic Seismic Hazard Analysis (PSHA). Both methods use an integration over a range of earthquake magnitudes and locations. While PSHA uses Ground Motion Prediction Equations (GMPEs) to compute the ground motion amplitude at a site, in our approach of PTHA we use numerical models to predict the wave-heights and inundation areas.

This report presents a methodology to provide site-specific tsunami hazard information in a format useful for prescriptive bridge loading calculations. This document outlines two different methodologies, or “Levels”, for determination of site-specific hazard. A Level 1 analysis methodology is developed in order to provide a relatively simple, rapid, and conservative estimate of the local tsunami hydrodynamics. A Level 2 approach is also provided, which permits the user to employ state-of-the-art numerical simulation tools. A Level 1 analysis is based on transect analysis, wherein the Energy Grade Line method is used to predict the evolution of tsunami flow depth and speed from the pre-tsunami shoreline to the inundation limit. The Level 1 approach initiates with accessing data from the tsunami inundation database developed by H. K Thio (AECOM), and extracting the relevant data nearest to the design site, or site of interest. A Matlab-based software program has been created to perform the transect analysis, and examples for the Pacific states are provided. Finally, two different load cases are recommended to be evaluated during the bridge design process, a case where the maximum speed occurs at 2/3 of the maximum flow depth, and a case where the maximum flow depth occurs at 80% of the maximum speed.

The loads acting on a bridge during tsunami inundation depend on several factors, each with significant uncertainty. In addition to flow depth and speed based on probabilistic tsunami hazard analysis (PTHA), the factors such as bridge deck orientation and debris in the flow contribute to the tsunami-induced loads on bridges. The basic approach to estimating tsunami loading is to compute reference horizontal, uplift, and downward forces based on two-dimensional equations. The flow depth and speed used in these equations will be based on site-specific PTHA. Then, simulation-based factors based will account for three-dimensional effects of skew and superelevation. Allowances for debris are also included.

1.0 PROBABILISTIC TSUNAMI HAZARD MAPS FOR THE WESTERN UNITED STATES

In this report, we describe the process for producing the 1,000 year probabilistic tsunami hazard maps developed for the five Pacific Ocean bounding states (California, Oregon, Washington, Alaska and Hawai'i). This effort has been commissioned by the Oregon Department of Transportation with additional funding of the other states through the Pacific Earthquake Engineering Research Center (PEER) and builds on previous work supported by the United States Geological Survey (USGS), PEER, the California Department of Transportation (Caltrans), the California Geological Survey (CGS) and American Society of Civil Engineering (ASCE).

The methodology and results presented in this report are the culmination of several successive and parallel projects originating with the initial development of the offshore probabilistic tsunami hazard analysis supported by the U.S. Geological Survey (USGS) under the National Earthquake Hazards Reduction Program (NEHRP) program (Thio et al., 2007). In this work, we developed the method of using tsunami Green's function summation to efficiently compute tsunami waves from sources around the Pacific Ocean (Figure 1-1) used for the development of models of probabilistic offshore waveheight exceedance. This methodology was further developed and applied to California probabilistic inundation hazard by Thio et al. (2010), funded by Caltrans through PEER. A major improvement in that study included the inclusion of aleatory variability in the tsunami calculations and the computation of probabilistic inundation anchored on the offshore exceedance amplitudes. This analysis was further developed and applied for CGS, with the development of probabilistic inundation maps for multiple return periods for California, and ASCE, for the development of 2,500 year inundation maps for the five western states, including significant improvements in source characterization, on-shore model resolution (10m for inundation), characterization of aleatory variability and epistemic uncertainty and updated methodologies and algorithms for inundation modeling. The current project builds directly on the ongoing CGS study and the ASCE 7-16 funded work. All these features will be described in more detail in the CGS report and Thio et al. (2017, 2018).

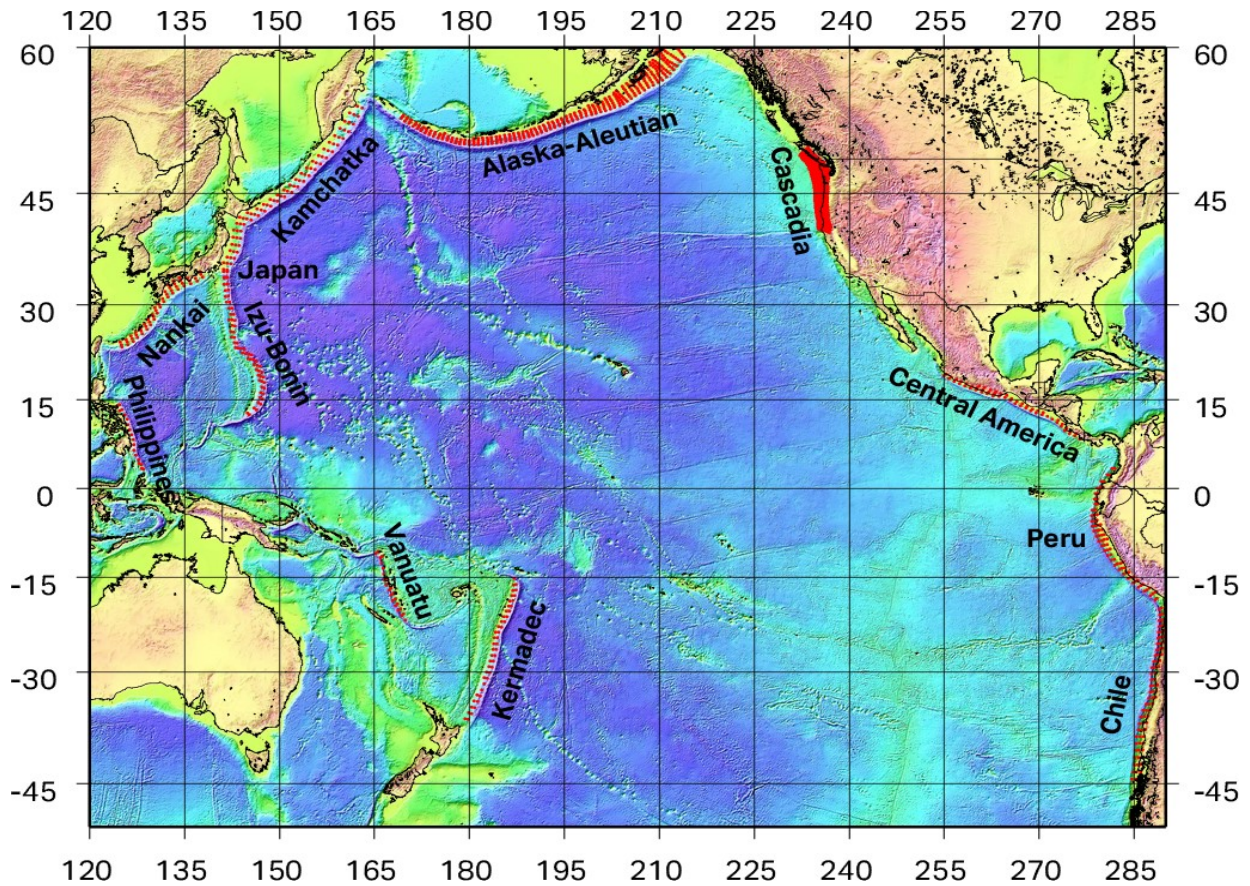


Figure 1.1: Source-zones around the Pacific Ocean that are included in this work.

1.1 PROBABILISTIC TSUNAMI HAZARD ANALYSIS (PTHA) BASICS

In an earlier project, URS (Thio et al., 2010) created a map of probabilistic offshore tsunami wave-heights by using a Green’s function summation approach. This approach enabled the integration over a wide range of source zones and magnitudes and the inclusion of epistemic uncertainties that describe our incomplete knowledge and understanding of natural processes, and aleatory variability, which expresses the randomness in natural processes. The methodology is similar to the common approach in Probabilistic Seismic Hazard Analysis (PSHA). Both methods use an integration over a range of earthquake magnitudes and locations. While PSHA uses Ground Motion Prediction Equations (GMPEs) to compute the ground motion amplitude at a site, in our approach of PTHA we use numerical models to predict the wave-heights and inundation areas.

For PTHA, the most obvious metric is the exceedance of a water level, wave amplitude or flow depth, as these are the most visible and recorded aspects of tsunami waves. There are, however, other metrics that may be more suited for certain purposes, such as flow velocities in ports and harbors or momentum flux for impact on structures.

The probabilities are computed in terms of the annual rate of exceedance, which, if we assume that the event occurrence follows a Poissonian (i.e. time-independent) distribution, can be translated into probability of exceedance in a certain amount of time through:

$$P = 1 - e^{(-\gamma t)} \tag{1-1}$$

Where:

P is the probability of exceedance in a time period t (also called exposure time), and γ the annual rate of exceedance. In engineering applications, we are usually interested in certain probability levels that are expressed in terms of P , such as a 2% (0.02) probability of exceedance in 50 years used in ASCE 7-16 (ASCE, 2017), where 50 years is the exposure time t . Inverting the above equation as:

$$\gamma = \frac{-\ln(1 - P)}{t} \tag{1-2}$$

We can then calculate the corresponding annual rate of exceedance as $0.00040405 \text{ year}^{-1}$, or a recurrence time, often referred to as Average Return Period (ARP), of 2475 years. Other return periods of engineering interest are 50%, 10% and 5% in 50 years, which correspond to 72, 475 and 975 years ARP respectively. In comparison, in flooding hazard the 100, 200 and 500 year ARP's are common. In this report, we have produced maps for all these probability levels and the 3000 year ARP as well.

The annual rate of exceedance is calculated as follows:

$$\phi(s) = \sum_{i=1}^{Faults} \left(\iint_{m,r} f(m)P(A > s|m,r)P(r|m)dm dr \right)_i \tag{1-3}$$

Where:

$f(m)$ = probability density function for annual rate of earthquakes of magnitude m

$P(A > s|m,r)$ = probability that tsunami amplitude A exceeds s given magnitude m and source at r

$P(r|m)$ = probability for a source at location r , given a source of magnitude m .

The earthquake recurrence rate is of course an important and directly relatable parameter with regards to the tsunami exceedance rates, but it is only one of several parameters which contribute

to the ultimate tsunami probabilities. A probabilistic analysis is an integration over a potentially large number of tsunamigenic events on different faults, but also includes the effect of natural variability (or aleatory uncertainty) of physical processes. Extreme outcomes have a low, but finite probability, and since we are determining the exceedance of a certain hazard parameter (such as maximum wave amplitude), the hazard will continue to increase with decreasing probability as we are sampling further into the tail ends of the aleatory variability distributions.

1.2 EPISTEMIC UNCERTAINTY AND ALEATORY VARIABILITY

Probabilistic tsunami hazard analysis, like its seismic counterpart, follows a dualistic approach to probability. Whereas some aspects are defined in the familiar terms of frequency of occurrence (such as intermediate earthquake recurrence, magnitude distribution), others are more based on judgment, which is a subjective approach (Vick, 2002). This is implemented through the use of logic trees, which express alternative understandings of the same process, e.g. large earthquake recurrence models, weighted by the subjective likelihood of that alternative model (“degree of belief”), where the weights of the alternatives sum to unity.

All aspects of earthquake occurrence and effects contain a measure of natural randomness, even if certain average behavior and measures are clearly identified. This is called aleatory variability and is usually expressed in terms of distribution functions around the mean and are included in a PTHA by sampling or integrating over this distribution function.

1.3 OVERVIEW OF THE PTHA METHODOLOGY

In order to ensure consistency with seismic practice, the AECOM approach closely follows, where possible, the PSHA practice. For instance, the overall framework and inputs remain quite similar to facilitate model exchange between the PSHA and PTHA. There are however some important differences between PSHA and PTHA. The most important difference between the two is the impracticality of using something similar to GMPEs in tsunami hazard due to the very strong dependence of tsunami wave-heights on bathymetry, which precludes the use of simple magnitude distance relations. Fortunately, since the global bathymetry is relatively well constrained and computational algorithms are sufficiently accurate and efficient, it is possible to replace the GMPE-type relations with actual computed tsunami waveforms. We can summarize the methodology with the following list of steps, with details discussed in later sections:

1. Identification and setup (subfault partitioning) of earthquake sources;
2. Computation of fundamental Green’s functions for every subfault to near-shore locations;
3. Definition of earthquake recurrence model;
4. Generation of a large set of scenario events that represents the full integration over earthquake magnitudes, locations and sources, for every logic-tree branch;
5. Computation of near-shore probabilistic wave-height exceedance rates;
6. Identification of dominant sources through source dis-aggregation;

7. Computation of probabilistic inundation hazard using a non-linear runup model anchored by offshore wave-heights.

In practice, the main process can conveniently be divided into generation, propagation, and inundation models. Steps 1-5 in the above scheme were already carried out for the ASCE 7-16 and CGS projects (Thio et al., 2017). The offshore exceedance amplitudes are therefore considered given in this study and this part of the process will only briefly be discussed further.

1.4 SOURCE CHARACTERISTICS

For the offshore probabilistic exceedance amplitudes, we have included megathrust sources from around the Pacific (Figure 1.1). The source characterization for the tsunami models consists of a geometrical characterization of the subduction interface (Hayes et al., 2012), recurrence models for earthquakes that define magnitudes (e.g. Murotani et al., 2008), their recurrence rate (either based on plate convergence rates or directly observed), and a generation mechanism for slip distribution on the fault (Thio et al., 2017).

1.4.1 Source geometry

The geometries of the different subduction zones are from Hayes et al. (2012) who developed curved surfaces of the top of the subducting slabs based on the earthquake catalog locations. These surfaces, representing the megathrusts, were discretized in subfaults with dimensions of 100 x 50 km for distant sources and 30 x 15 km for the Alaska and Cascadia, since small-scale details can be important in the near-field hazard.

The geometry of the Cascadia subduction has been analyzed in several papers (e.g. Fluck et al., 1997; Wang et al., 2003; McCrory et al., 2006) and we have adapted the latter in this study. Our model consists of quasi-rectangular subfaults, which follow the contours of the McCrory et al. (2012) model. For the main slab interface we have defined 480 subfaults, but it should be noted that in the current analysis many of these subfaults are not used because they are more than 50% in area outside the limit of the seismogenic zone. It is however conceivable that they will be used in future models for alternative logic tree branches.

1.4.2 Source complexity

Murotani et al. (2008) studied the slip distributions of several subduction zone earthquakes and found a ratio of maximum slip over average slip of 2.2. In the nearfield, such variability of slip has significant consequences; while the long-term slip on a megathrust maybe uniform, between events there will be large variations, which affect the probabilistic analysis. To include this aleatory slip variability, we used variable slip rupture models with one third of the rupture as an asperity with twice the average slip and the other two-thirds of the rupture at half the average slip. In order to achieve uniform long-term slip, we computed a total of three scenarios (Figure 1.2) for each event where the asperity occupies every part of the rupture once, minimizing the risk that in some areas the hazard is over- or under-estimated due to incomplete or overlapping asperity coverage.

1.5 SPECIFIC SOURCES

1.5.1 Cascadia subduction zone

The Cascadia subduction zone is used in a slightly different manner than the distant sources, since for Northern California this source is local and causes significant co-seismic uplift or subsidence, which needs to be considered when computing the inundation. Also, since it is a local source, details in the source geometry and slip distribution are more important than in the distant sources.

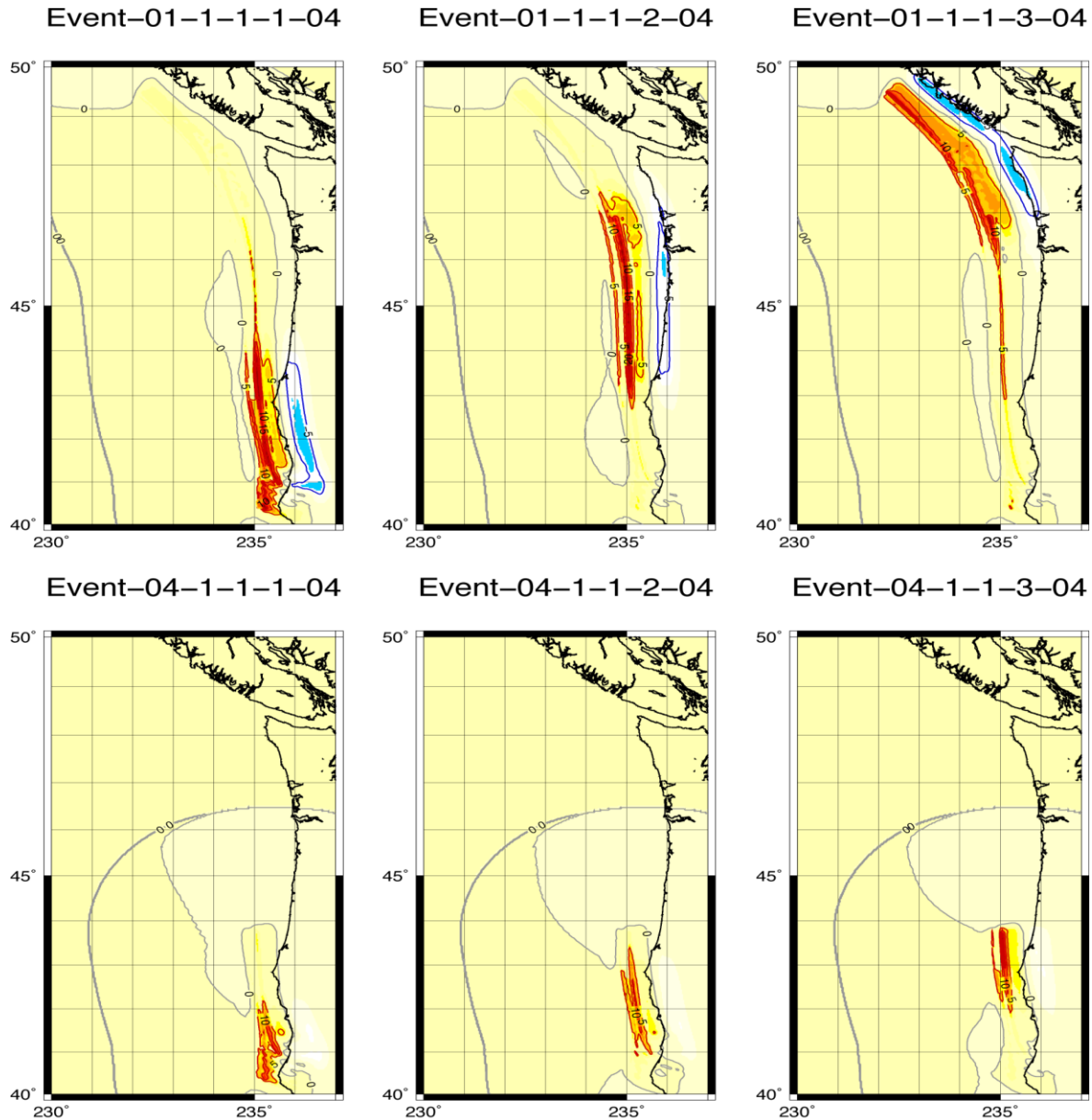


Figure 1.2: Vertical displacement field (res=uplift) for two scenarios. Top is a full rupture earthquake, bottom is a partial rupture, each shown three times with different asperity locations.

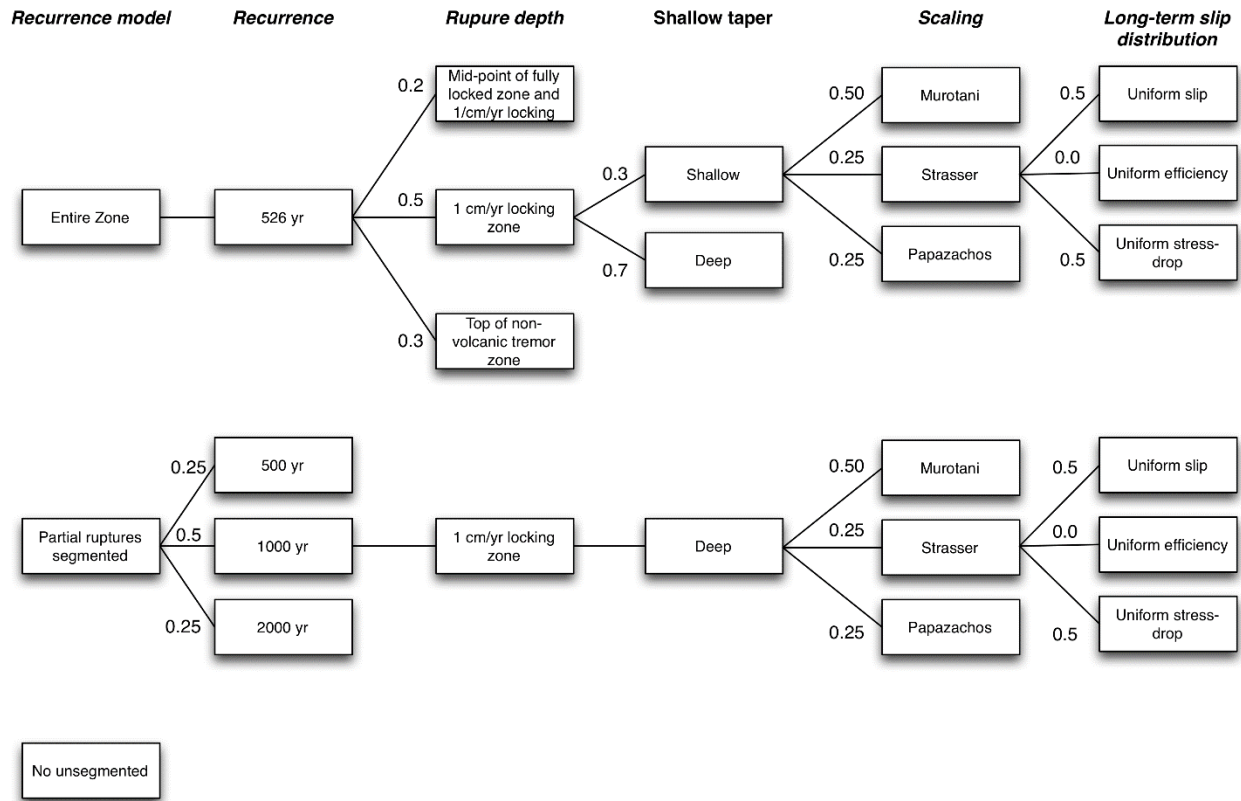


Figure 1.3: Logic tree for the Cascadia subduction zone (adapted from the 2014 USGS National Seismic Hazard Map, Petersen et al., 2014). The smaller segmented ruptures have longer return times than the full rupture, and therefore the hazard in Cascadia is dominated by the full rupture model for most return periods.

We adopted the recurrence model and geometry from the 2014 revision of the National Seismic Hazard Maps (Petersen et al., 2014, updated by Chen et al., 2014) for the Cascadia subduction zone. This model has gone through a thorough review process with input from experts in the field over several years. It is constrained by various types of data, such as geodetic data (GPS) and long-term tide records, which reveal interseismic uplift or subsidence, that identify the extent of the locked zone of the megathrust and thus future rupture extent. Uncertainties in the physical models (epistemic uncertainties) are included through weighted logic tree branches (Figure 1.3), which include alternative branches for segmentation, down dip termination of the rupture zone, scaling relations, up-dip slip tapering, and long-term slip distribution. Apart from the latter two, all the other branches and recurrence rates were taken un-changed from the USGS model.

The convergence rate across the Cascadia subduction zone provides a constraint on the recurrence relations, since the total slip rate is an upper bound to the event recurrence rate times the slip per event. Most models of the Cascadia subduction zone predict an increase of convergence rate from the south to the north. McCrory et al. (2012) show the convergence rate increasing from 29 mm/yr in northern California to 45 mm/yr at Vancouver Island. Since little is known about the seismic efficiency along the Cascadia subduction zone compared to the amount

of data on recurrence times of events, we are using the event recurrence times as our primary input to the probabilistic models, and will only use the plate rates as a check afterwards.

Our current implementation of the recurrence model yields a maximum displacement rate of 20 mm/yr, which is well below the plate convergence rate in the north, and implies a seismic efficiency of 0.5, i.e. half of the convergence rate is accommodated by mechanisms other than earthquakes in the north. To the south, the convergence rate is actually more similar to our slip rate.

Frankel and Petersen (2012) presented an earlier version of the Cascadia earthquake recurrence model as a source element to the National Seismic Hazard Maps (Petersen et al., 2014). It was decided to adopt the USGS model, which is the result of an extensive peer-review process and includes all the recent science on Cascadia earthquake source recurrence. Details and background of the model can be found in Frankel and Petersen (2012). Initially, Frankel (pers. comm., 2012) developed a set of six different rupture extents along the Cascadia subduction zone with associated average return periods based on the aforementioned work of Goldfinger et al. (2011) and other studies. Most of these were used in the 2014 NSHM and the final model scenarios were provided to us by Chen (pers. comm, 10/1/2013). These ruptures, which are only defined in terms of length segments along the Cascadia zone form the basis of our source model, are further defined in a logic tree framework (Figure 1-3) that addresses the epistemic uncertainties in fault width, splay faulting, and aleatory uncertainties such as slip variability.

1.5.2 Alaska subduction zone

The USGS Seismic Hazard map for Alaska was developed more than a decade ago (Wesson et al., 2007), and since that time considerable paleo-seismic work in the Aleutians has yielded significant amounts of data that have shed new light on the occurrence of large earthquake in the region (Witter et al., 2016). Also, the 2007 USGS maps only considered segmented ruptures whereas for the tsunami we have to take into account the occurrence of multi-segment ruptures (Shannon et al., 2009). The segmentation model that we developed in-house for the Alaska subduction zone is shown in Figure 1.4.

1.5.3 Other sources

In Figure 1.4 we also show the source model for the Kuriles. This map shows the segmented model that is used in seismic hazard studies (Earthquake Research Committee, 2005), and which are one principal branch on our logic tree. The other principal branch contains multi-segment ruptures. These are typically events that have not been observed (in historical times) but for which no good reason exists to preclude them from our model. For tsunami generation, these models are very significant since tsunamis scale directly with slip, whereas such models would only have limited impact on seismic hazard analysis due to the saturation of ground motions with magnitude. The recurrence models for the remaining circum-Pacific sources (Figure 1.1) have the following general characteristics:

- Epistemic branches include a full rupture across the entire fault zone, with weights determined from the literature

- Recurrence rates are based on plate convergence rates, with several branches for seismic coupling.
- Source geometry is taken from Hayes et al. (2012)

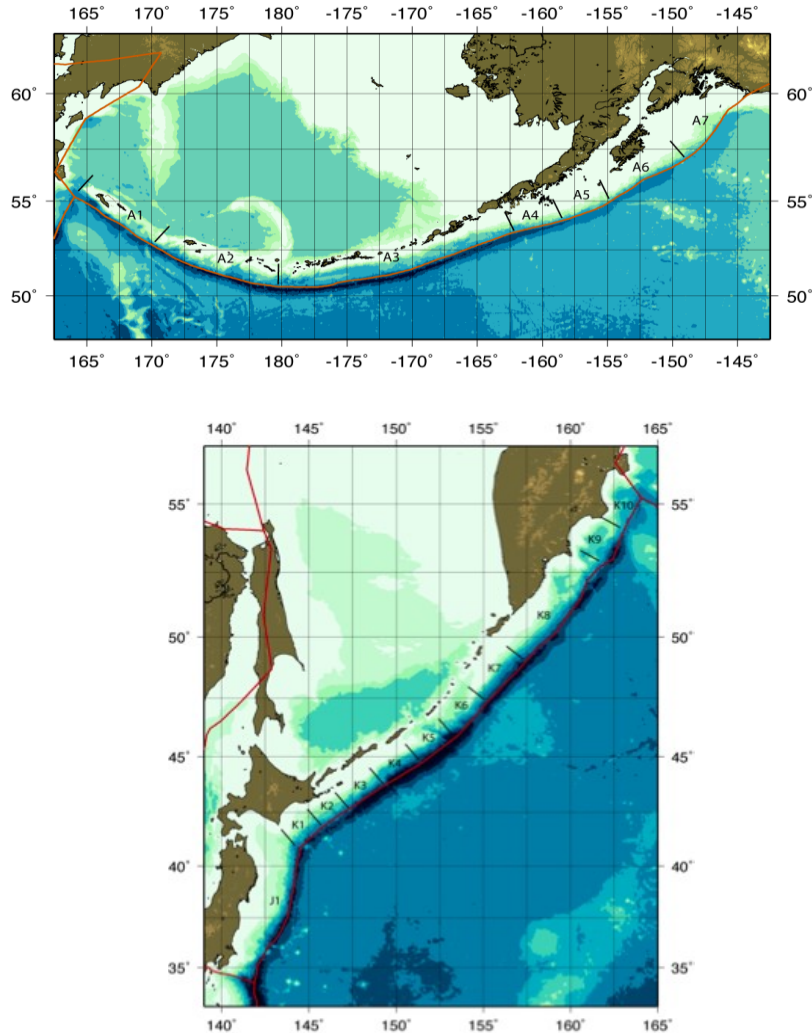


Figure 1.4: Segmentation models for the Alaska/Aleutian subduction zone (top) and the Japan/Kurile/Kamchatka subduction zone (bottom).

1.6 TSUNAMI PROPAGATION MODELING

Contrary to traditional seismic practice, the actual propagation term in the hazard equation for tsunamis is solved using numerical models rather than empirical relationships. This is due to: 1) the very strong lateral heterogeneity in the propagating medium (the oceans) which limits the usefulness for simple empirical relationships; and 2) the greater accuracy in tsunami modeling compared to high-frequency seismic modeling. All tsunami simulation algorithms use the same initial condition, namely the vertical deformation, whether instantaneous or distributed over time, of the sea surface. This deformation is set equal to the deformation of the underlying seafloor.

1.6.1 Algorithms

In this project, we have used a two-dimensional (depth averaged) approximation, which is standard for tsunami modeling. Since we are computing inundation maps, a nonlinear method is necessary to compute the run-up heights correctly. We have developed an in-house code that uses the Clawpack library (Mandli et al., 2016) to solve the tsunami inundation problem. Compared to finite difference methods, the finite volume method is more accurate, especially in the presence of shockwaves, a condition that exists especially in the near-source regime. It includes several nonlinear (e.g. bottom friction, advection) effects and a moving boundary, which allows for inundation. This code allows for nested gridding, which means that we use coarse grids for deep ocean modeling and increasingly finer grids towards the coastline so that we can capture fine detail without overdue computational burden.

1.6.2 Elevation models

For the deep ocean modeling (both with the linear and non-linear codes) we have used the SRTM30+ model (Becker et al., 2009) which is a combination of satellite derived bathymetry and sounding data. For the United States coastal areas, this model is primarily based on the National Oceanic and Atmospheric Administration (NOAA) near-shore grids and thus provides an accurate, convenient and seamless model of the entire Pacific Ocean. We have used this digital elevation model (DEM) at a resolution of 30 arc-seconds (1/120 degree latitude, which is about 1 km).

For the nearshore and inundation modeling, we used higher resolution models that are based on the NOAA Tsunami Gridding Program (Eakins and Taylor, 2010) at decreasing grid sizes down to 60m for most regions and 10 m for selected areas in Oregon and most of California. At 10 m resolution, many details in the bathymetry and topography are well-resolved and the nested gridding thus provides a good trade-off between accuracy and computational feasibility.

1.7 OFFSHORE TSUNAMI HAZARD

The first step in our two-step approach, the offshore hazard, is described in Thio et al., (2017) and shown in Figure 1.5. The hazard shows an expected pattern of high hazard in Alaska and Cascadia, tapering off significantly through central and southern California. Hawaii shows an elevated hazard due to its exposure to several different subduction zones. In Figure 1.6, we present an example of two disaggregation plots for California and Hawaii, which shows the different source sensitivities for different target regions. For the production of the inundation map, these offshore hazard values, and the source disaggregation are the most important information needed.

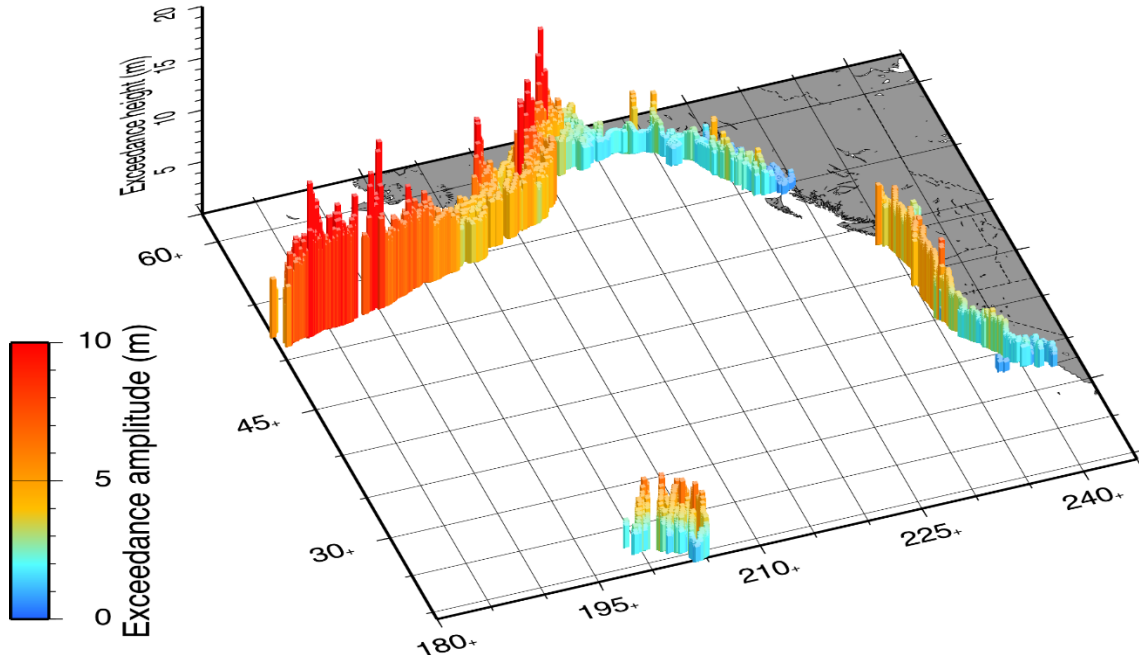


Figure 1.5: 1000 yr offshore exceedance amplitudes for the five western states.

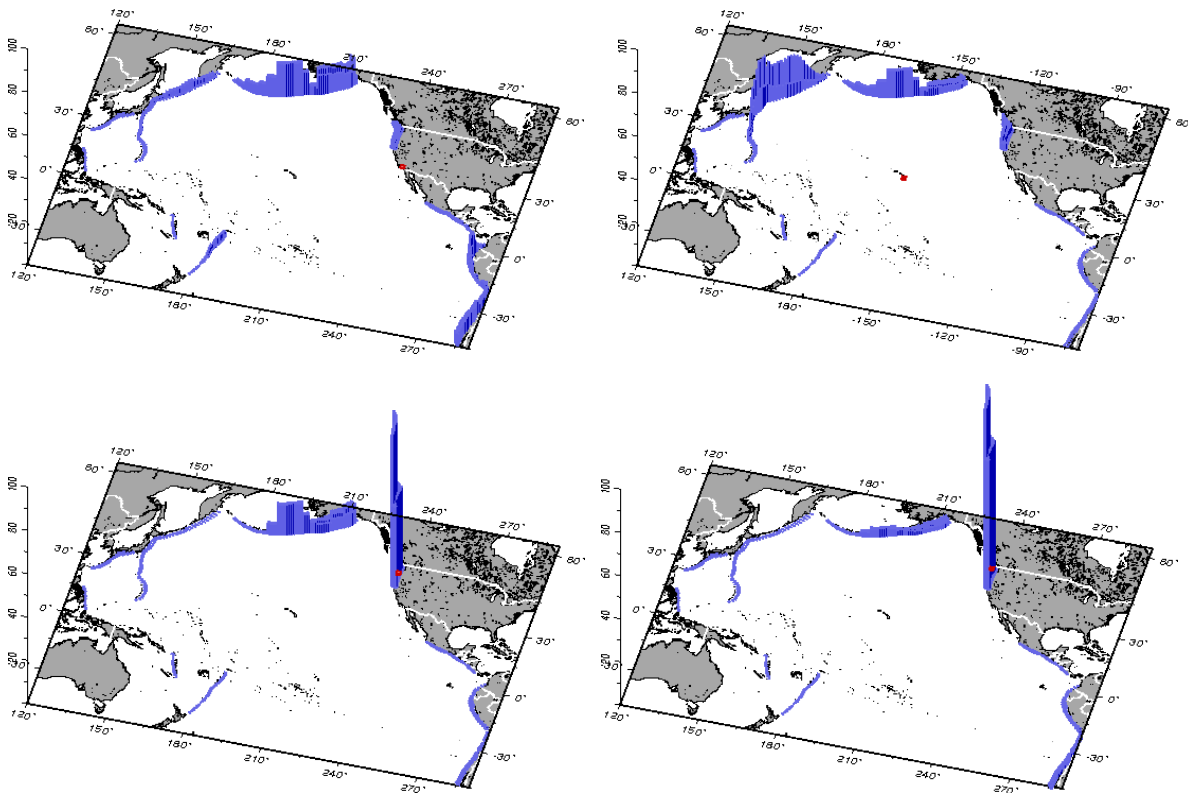


Figure 1.6: Source disaggregation for a site in southern California (top left), Hawaii (top right), Oregon (bottom left) and Washington (bottom right) showing the relative contributions to the hazard at those particular sites.

1.8 INUNDATION COMPUTATION

Using these offshore wave-heights, we compute the actual probabilistic inundation in the second stage of this project by performing fully non-linear tsunami inundation simulations for a suite of scenarios that provide offshore amplitudes that are consistent with the maps computed in the first stage. For these computations, we used the Clawpack-based code that was developed in-house. The final maps were computed for high-resolution grids (60m and 10 m horizontal) from NOAA (Eakins and Taylor, 2010) that were specifically developed for tsunami inundation modeling. These are so-called “bare-Earth” models that are stripped of any building structures and use a single Manning’s friction coefficient (0.025) for all areas.

The selection of these scenarios is based on a disaggregation analysis of the hazard (Figure 1.6), which is essentially a bookkeeping tool that shows us the relative contribution to the hazard for every source. This procedure is somewhat similar to the process of spectral matching used in seismic hazard analysis, where a seismogram is scaled up so that its spectral envelope matches the amplitudes from the probabilistic seismic hazard analysis. In both cases, the actual scenario or time series used to compute the final hazard is usually well above the mean that would be expected for the particular dominant magnitude and source location because of the contribution of the aleatory variability, which, for decreasing probabilities gives rise to an increase of the hazard. When we compute the final probabilistic inundation by computing tsunamis all the way from the source, the scaling is applied to the initial condition, which is the same as scaling the slip on the fault and thus increasing the nominal magnitude of the earthquake. The latter can thus be much larger than the magnitude one would use for a deterministic tsunami scenario. The same happens in seismic hazard, but there the effect is implicit since one scales the individual time series rather than the input earthquake.

The actual inundation maps are obtained by sampling of the offshore hazard curve, where, rather than directly matching the offshore exceedance amplitudes, we define a small but representative suite of scenarios to compute the probabilistic hazard. These events are chosen to sample the 1,000 year offshore amplitudes densely, so that the probabilistic inundation for that return periods can be computed accurately.

We have computed scenarios from Alaska, Chile and the Kuriles, the dominant distant sources along the west coast that span a range of sizes and cover the entire 1,000 year exceedance amplitudes. In addition, for the Cascadia subduction zone, we expanded this set with another 10 Cascadia scenarios. By choosing scenarios that give a close match to the offshore exceedance wave heights for the 1,000 year return period from source regions indicated by the deaggregation in Figure 1.6, we ensure that this event set is representative for the tsunami hazard in the areas covered.

Earlier tests had already established that the sensitivity to the source region for distant events is low, as long as the offshore amplitude constraint is met. In Figure 1.7, we have tested our procedures also by running the inundation hazard at Humboldt Bay (for 2,475 year ARP used in ASCE 7-16) for a combined data set and with a set only containing the distant events (even though the hazard at that return period is dominated by Cascadia events). It is clear that even between distant and local sources, the sensitivity is not that great.

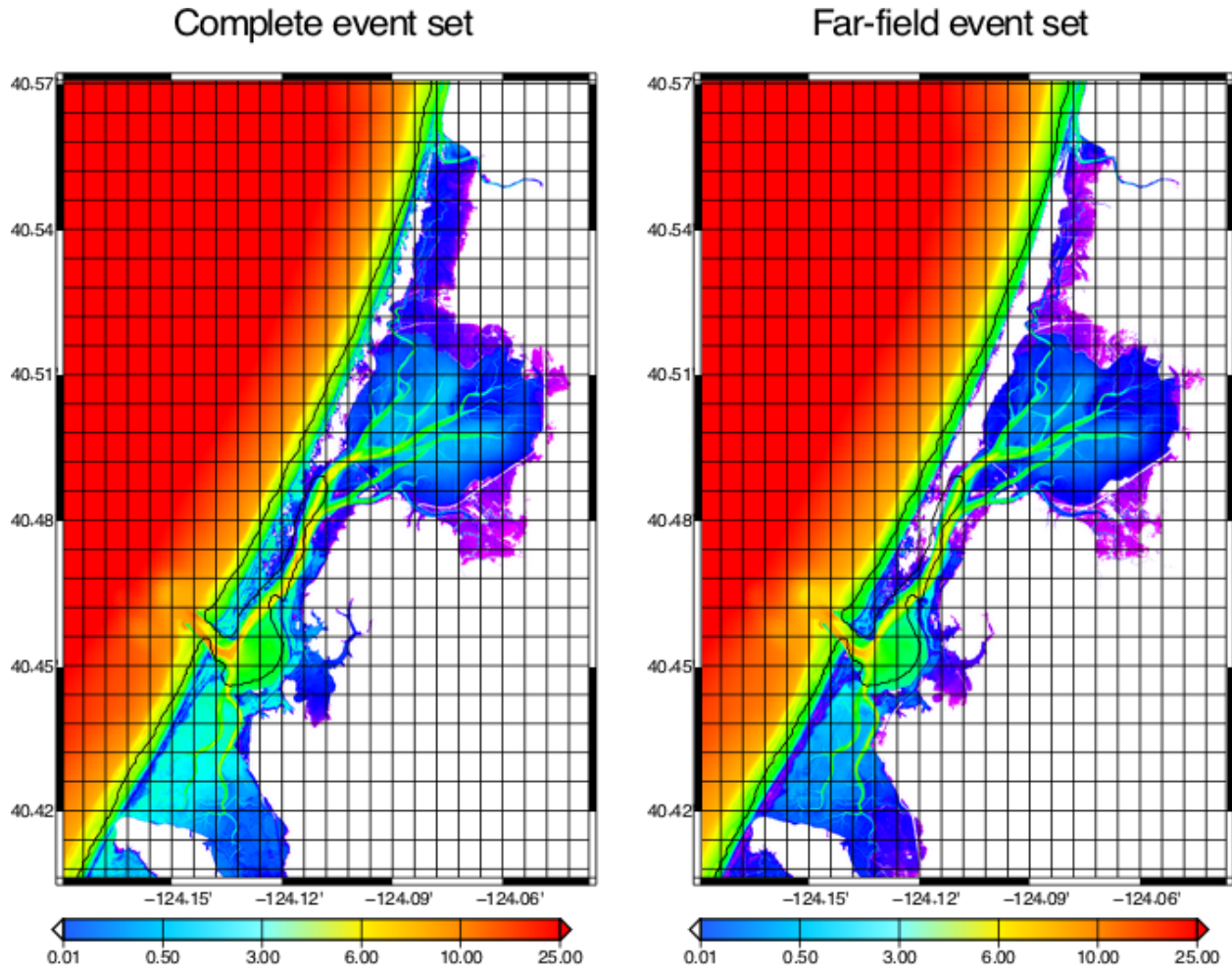


Figure 1.7: Comparison for the 2475 year Humboldt Bay probabilistic flow depth maps for a model using the full event set (Left) and only the far-field event set (right). The overall inundation pattern appears quite stable.

1.8.1 Inundation scenario probabilities

To compute the probabilistic inundation from this set, we need to determine the rate of occurrence for each scenario, i.e. the probability distribution of the representative event set.

The metrics that we use are the offshore amplitudes of these scenarios at the same locations for which we derived the offshore hazard curves. Since we are considering a discrete number of events, the probability distribution of the offshore amplitudes of the reduced set (p) is a Probability Mass Function (PMF), which can be determined from the offshore hazard curve (P), a Cumulative Density Function (CDF), since the probabilities of the reduced event set need to satisfy the offshore hazard curves (Figure 1.8).

In summary:

The probabilities are anchored to the probabilistic offshore amplitudes, so we define the probability for event i , p_i , as the probability of its offshore amplitude a_i : $p_i = p(a_i)$ events are

sorted according to their offshore amplitudes: $a_i < a_{i+1}$, with the number of events in our reduced set n .

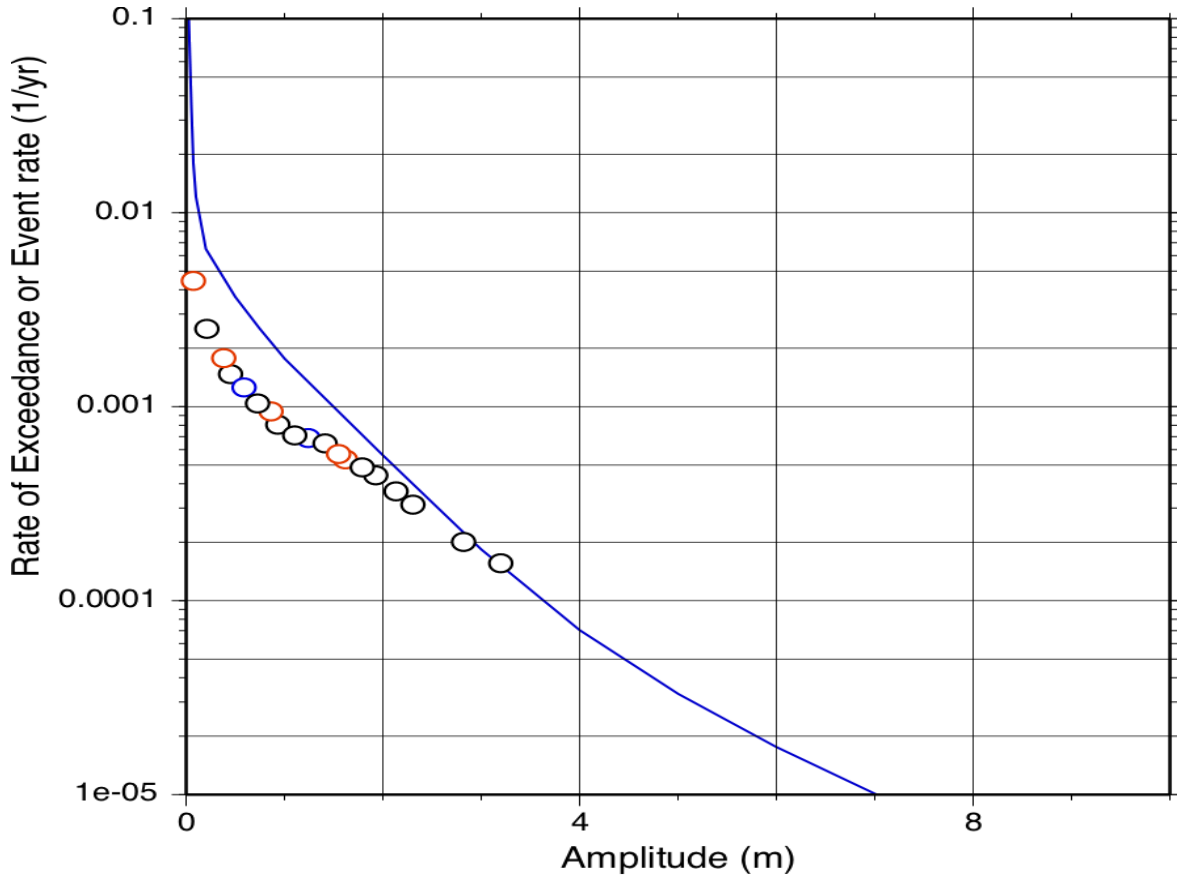


Figure 1.8: Schematic example of the relationship between the offshore hazard curve (blue line) and the probabilities of the reduce event set (circles, color coded according to source zone). Note that the event probability of the largest amplitude is equal to the exceedance probability of the offshore hazard curve.

The offshore hazard curve (CDF), expresses the probability of exceeding an amplitude A : $P(a \geq A)$. Then:

$$p_i = p(a_i) = P(a \geq a_i) - \sum_{k=i+1}^n p(a_k) \tag{1-4}$$

Note that this is essentially the inverse of the process by which the offshore hazard curves were obtained from the original, comprehensive, set of events, which was several orders of magnitude larger. As an alternative to the numerical approach, we can also obtain the rates from the slope of the hazard curve, which yields similar results, which indicates that our sampling of the hazard curve is sufficiently dense.

Once the event probabilities, or rates, have been determined, it is possible to compute the inundation hazard curves at every cell in the same way as the offshore hazard curves were computed. We note that at each cell the hazard curve is computed independently, so that in theory the inundation at the same probability level in different cells can be affected by different scenarios from the representative event set, which is preferable over the other approaches where one or two scenarios determine the inundation in the entire model. Such a situation might arise if different source regions yield very different inundation patterns. In our experience in California, this source dependence does not seem to play a large role for the distant events and even in near-source environments in Cascadia this is not a significant issue as shown in Figure 1.7.

The event rates are also used to compute the probabilistic maps for flow velocity and momentum flux. Since these parameters show a much stronger complexity and variability between scenarios compared to wave amplitudes, we believe the current method is much better suited for resolving these details than the single- or dual-scenario approaches. A more systematic analysis of these parameters is recommended for future work.

1.8.2 On-land hazard curves

The only complication when computing the hazard curves is that the on-land amplitudes are truncated by the topography (for some or all scenarios a grid point remains dry) whereas the offshore amplitudes have finite values everywhere for every event. We normally interpolate the inundation hazard curve to obtain exceedance amplitudes for specific return periods. In the case where a specific probability level falls below the lowest scenario amplitude in a cell, we can use an extrapolation of the two lowest scenario amplitudes to estimate amplitude for the target probability. If the extrapolated value falls below the topography, the flow depth is simply set to zero. Likewise, when we apply an additional aleatory variability, a scenario amplitude may be increased to the extent that it would flood cells that had remained dry. In order to solve this issue we also apply an extrapolation from a larger “wet” scenario amplitude using the amplitude ratio between the two scenarios for the nearest cell where both scenarios had non-zero amplitudes. These procedures are fully automated, and performed for every cell independently.

1.9 INUNDATION GRIDS

The resulting inundation grids that we produced are based on a combination of tele-tsunami sources (primarily Alaska and the Kuriles) and the Cascadia subduction zone. Since both the location and size of the scenarios and their relative contribution were based on the deaggregation of the probabilistic results, we simply integrated over the entire set using the return periods obtained in 6.1.1. We present an example of grid of exceedance flow depths in Figure 1.9. We have chosen flow depth as the main deliverable since the absolute wave amplitudes, in the near-source Cascadia and Alaska regions not necessarily refer to the same ground surface elevation, due to tectonic uplift or subsidence. This is different for each earthquake scenario (or zero in the case of distant sources) and used as initial condition for the finite-difference calculations and thus automatically applied during the modeling. Flow-depths on the other hand always refer to the ground surface, regardless of the absolute elevations.

We have computed grids for exceedance flow-depth, flow velocity and momentum flux. Figure 1.10 shows the complete set of 60 and 10m high-resolution inundation maps that are available.

We have also developed probabilistic subsidence maps for these areas conforming to ASCE 7-16. Finally, for many bridge locations time series for the constitutive scenarios are available from the author by request. Figure 1.11 shows an example of the vertical amplitude and horizontal flow velocities recorded for a single scenario at a location in Oregon.

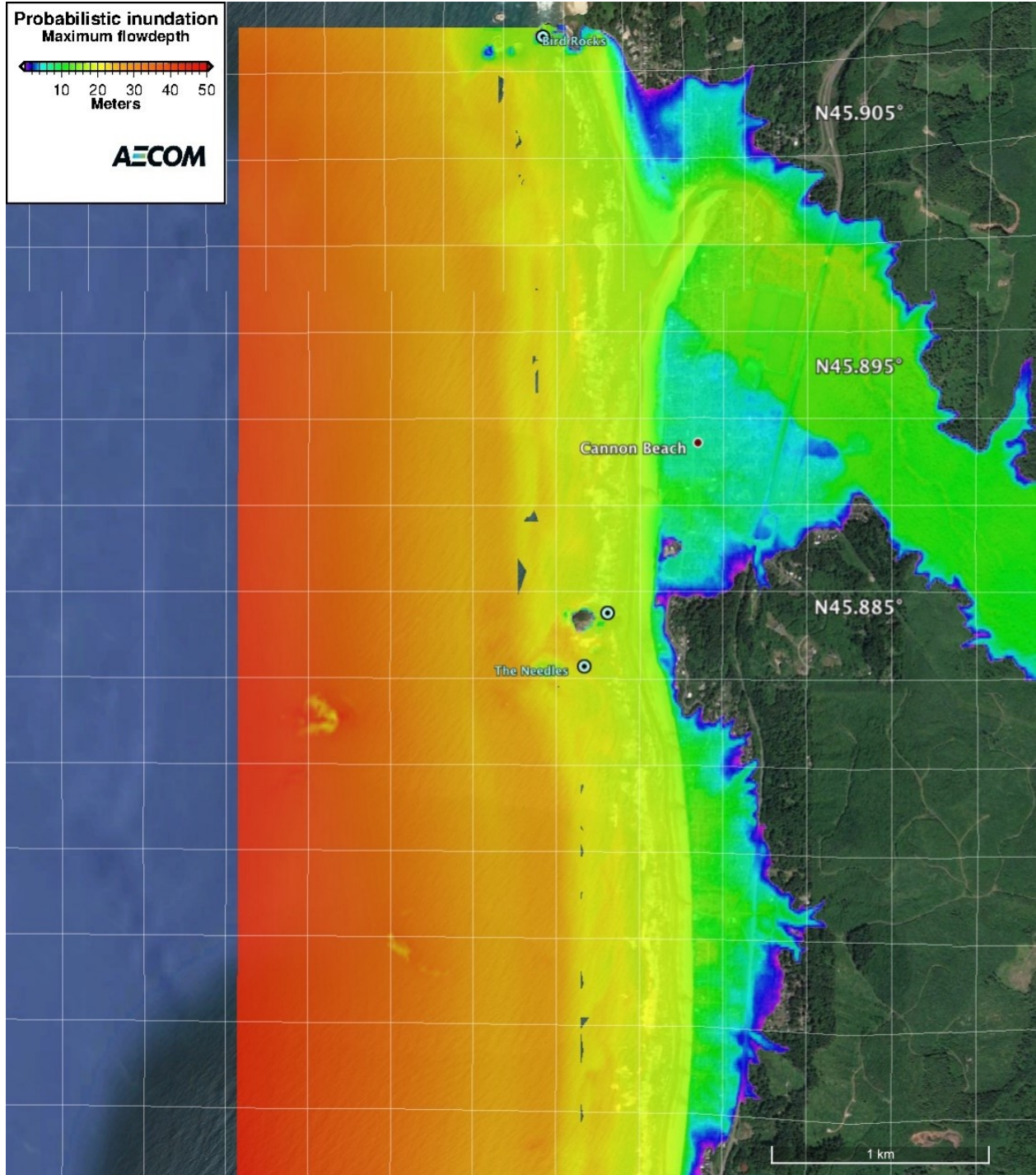


Figure 1.9: Example of a 1000 yr map of flow depths for the Cannon Beach, OR, area. Resolution is 10m.

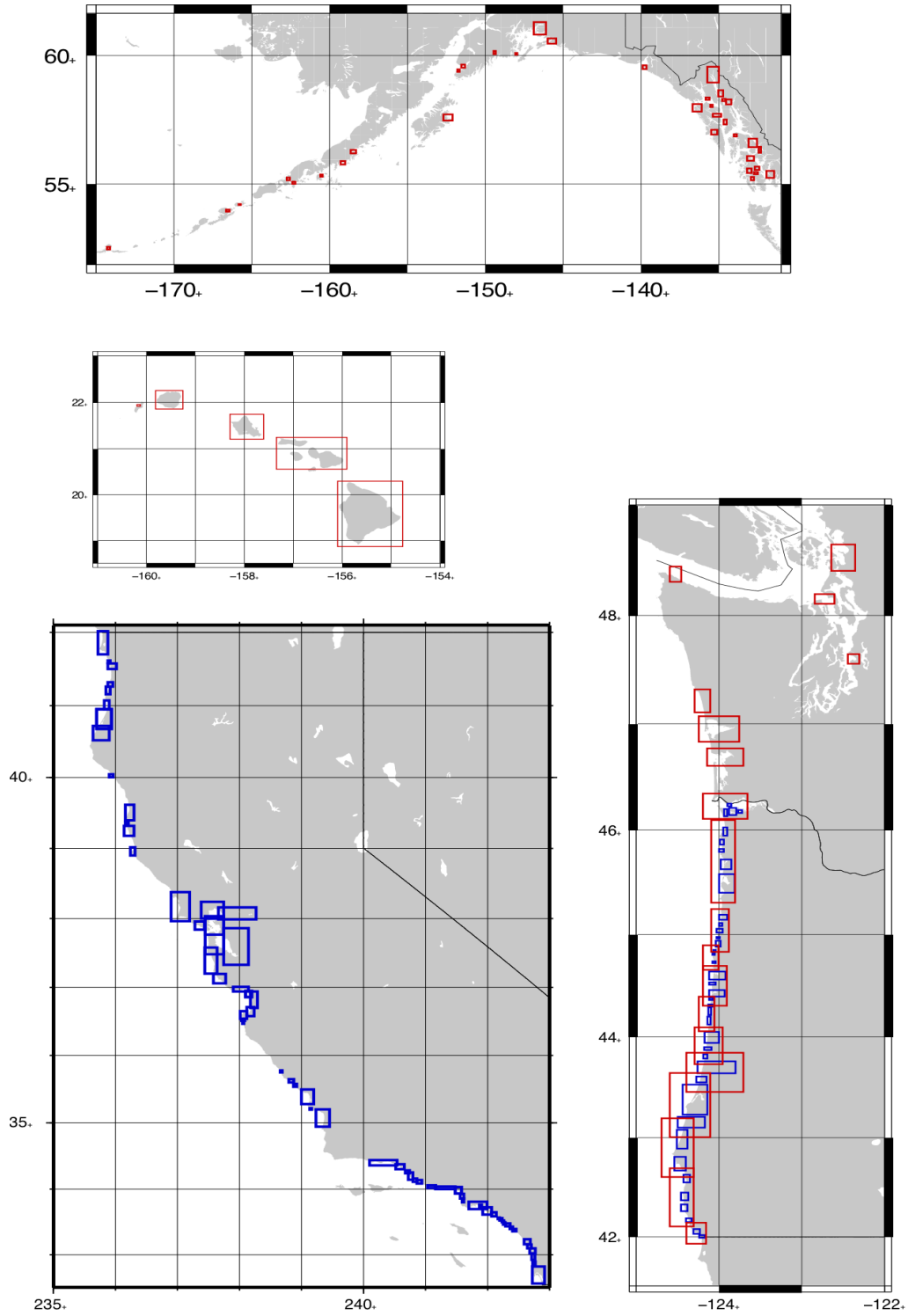


Figure 1.10: Areas covered in this study. Blue outlines indicate 10m grids, red outlines indicate 60m grids

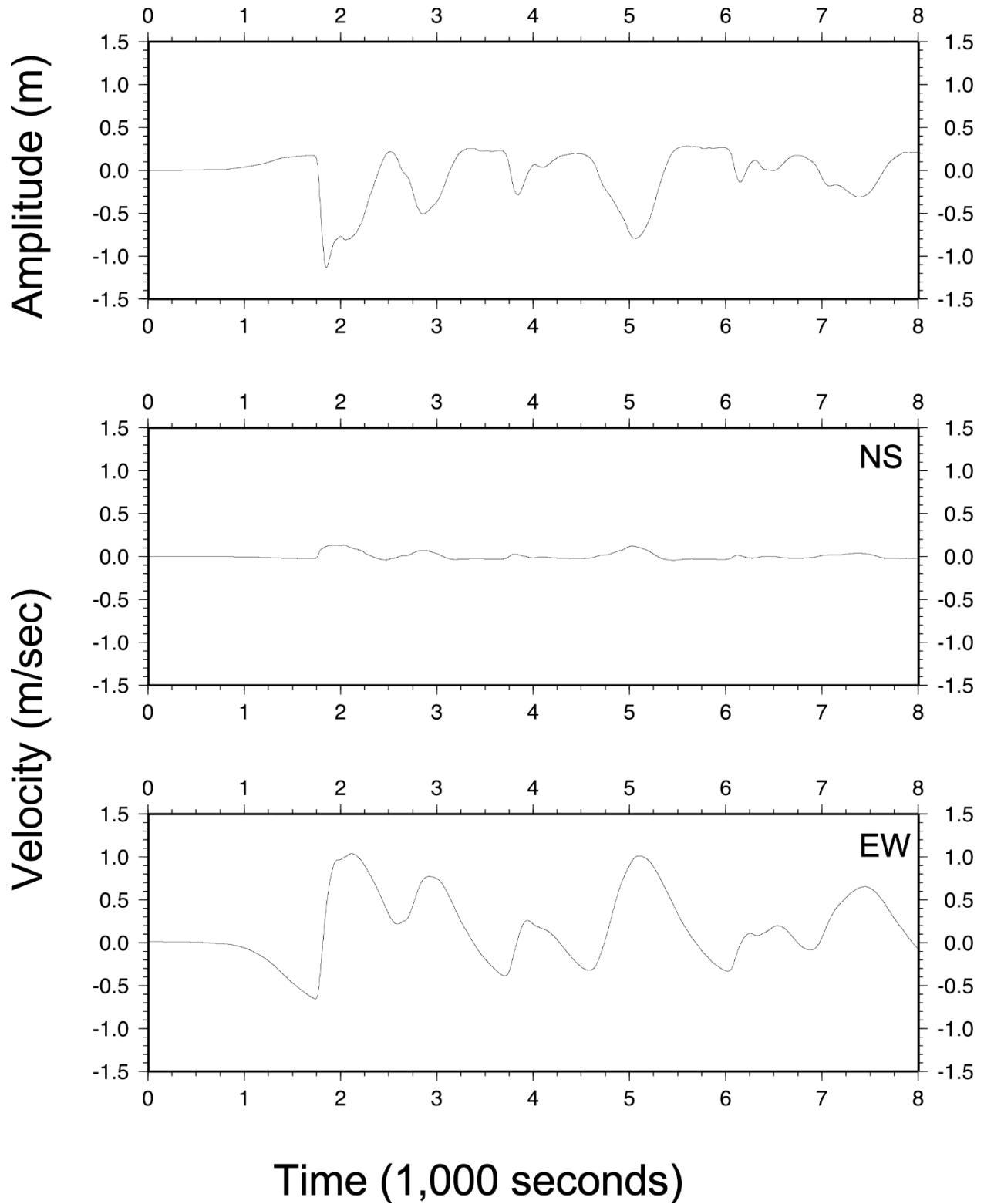


Figure 1.11: Example of time series (vertical amplitude, horizontal flow velocity) for a site in Oregon.

2.0 QUANTIFICATION AND INCLUSION OF UNCERTAINTIES IN ONSHORE TSUNAMI PROPAGATION

2.1 BACKGROUND

On March 11, 2011 a $M_w=9.0$ earthquake generated a tsunami 130 km off the coast of Sendai, Japan (Mori et al. 2011). This event is one of the worst in Japan history, killing more than 15,000 people and causing more than \$200 billion (USD) in damage. Available data shows that in some areas runup elevations reached 40 m and flow velocities reached more than 14 m/s (Mori et al. 2011, Koshimura and Hayashi 2012). This event raised the safety concerns of many coastal communities. Along the Sendai plain, the tsunami traveled more than 5 km inland with a maximum measured runup of approximately 9.4 m and an average of 2.5 m above Mean Sea Level (MSL) (Mori et al. 2011). The tsunami velocities measured by Koshimura and Hayashi (2012) at different locations on the Sendai plain ranged from 2-8 m/s. Due to the measurements collected during and after the Tohoku event, researchers are provided a great opportunity to model, study and understand the nearshore and onshore hydrodynamics of tsunamis.

Numerical model predictions are important for the development of probabilistic and deterministic methods which are used for Tsunami Hazard Assessments (THA). Generally, methodologies for Probabilistic Tsunami Hazard Assessment (PTHA) use numerical models to predict various products (runup, inundation and flow velocity) which are used to perform a statistical analysis to compute recurrence interval rates at a given location (Geist and Parsons 2006, Gonzalez et al. 2009, Thio et al. 2012 and Gonzalez et al. 2013). In a deterministic approach, worst-case scenarios are modeled by considering physical limitations of the natural occurrences (Gonzalez et al. 2007). So, by better understanding model bias and uncertainties, more accurate and reliable THA and PTHA will be developed. This will lead to improvement in risk assessment and hazard mitigation in coastal areas susceptible to tsunamis and better evacuation, maritime, land-use and construction planning can be achieved.

In the past decades numerical models have been developed that can accurately predict tsunami runup, inundation and flow velocity. Due to the surge of “state of the art” numerical models and their widespread use in this field there is a need to better understand model predictions and their uncertainties for better evacuation and construction planning. In this study The Method of Splitting Tsunami (MOST) (Titov and Synolakis, 1995 and 1998) and GeoClaw (LeVeque 1997, 2002) tsunami models are used to compare runup and flow velocity results to measured field data. Available field survey data and video footage analysis measurements are used to compare model runup and flow velocity predictions. Possible sources of error and uncertainty in their predictions are analyzed and discussed. This study includes detailed comparisons between observations and numerical simulations in Sendai, focusing on the Sendai plain area.

2.2 METHODOLOGY: FIELD MEASUREMENTS AND OBSERVATIONS

The field survey data published in Mori et al. (2011) and the flow velocity measurements from Koshimura and Hayashi (2012) are used to compare accuracy and reliability of numerical model predictions. More than 5300 measurements were recorded by a large group of scientists and researchers. A total of 63 universities and 297 people were involved in this project covering 2000 km of the Japanese coast. In Sendai the maximum measured runup elevation was 9.4 m (Mori, N., & Takahashi, T, 2012). Only 10 percent of the runup measurements were greater than 5 m. For this study we will be focusing on the Sendai plain (particularly from 38.10° N to 38.28° N). The wave front at the Sendai plain reached more than 5 km inland from the shoreline with the average being 4.2 km.

Flow velocities estimates measured by Koshimura and Hayashi (2012) were obtained from a 2-D projective transformation video analysis. One of the two locations where measurement estimates were made was the Sendai plain. The video used in the analysis was taken by a Japanese broadcasting company. Flow velocity estimates were made at four different locations within the Sendai plain. These locations are at a distance of 1000-3000 m from the coastline. The maximum measured flow velocity was 8.0 m/s.

The grids used in this study are from the M7000 digital contoured bathymetric data and the GSI 10-m digital elevation models (<http://fgd.gsi.go.jp/download/>). Five nested grids were used in the numerical models. The propagation grid, or grid A, was the coarsest grid at 3 arc-minutes. Four additional nested grids (1 arc-min, 20 arc-sec, 4 arc-sec and 1 arc-sec) were used covering the area of interest. Also, three additional grids were created (0.67 arc-sec, 0.50 arc-sec and 0.33 arc-sec) by interpolating the 1 arc-sec grid. These grids were used to analyze convergence and variability within the MOST model predictions. All the grids are referenced to Mean Sea Level (MSL) vertical datum and to the World Geodetic System of 1984 (WGS 84) horizontal datum.

2.3 METHODOLOGY: TSUNAMI MODELING

The Method of Splitting Tsunami (MOST) model was developed as part of the Early Detection and Forecast of Tsunami (EDFT) project and introduced by Titov and Synolakis (1995 and 1998). This model is currently used by NOAA for propagation and inundation forecasting (Titov, 2009). MOST has been validated and successfully tested in various studies (Synolakis et al., 2007; Titov and Synolakis, 1998; Titov and Gonzalez 1997). Wei et al. (2011) modeled the 2011 Tohoku tsunami with MOST and presented a detailed analysis of runup height and inundation along the Japanese coast. MOST solves the 2+1 nonlinear shallow water equations:

$$h_t + (uh)_x + (vh)_y = 0 \tag{2-1}$$

$$u_t + uu_x + vu_y + gh_x = gd_x - Du \tag{2-2}$$

$$v_t + uv_x + vv_y + gh_y = gd_y - Dv \tag{2-3}$$

Where:

$\eta(x, y, t)$ = wave amplitude, d is the water depth, $h(x, y, t) = \eta(x, y, t) + d(x, y, t)$, $u(x, y, t)$ and $v(x, y, t)$ are the depth-averaged velocities, and $D(h, u, v)$ is the drag coefficient computed by equation 2-4:

$$D(h, u, v) = n^2 gh^{-4/3} \sqrt{u^2 + v^2} \quad (2-4)$$

Run-up and inundation were only performed in the higher resolution grids (1 arc-sec, 0.67 arc-sec, 0.5 arc-sec and 0.33 arc-sec, or approximately 30m, 20m, 15m and 10m, respectively). A Manning coefficient of $n = 0.025$ was used in all the simulations. For a detailed description of MOST refer to Titov and Synolakis (1995 and 1998).

GeoClaw, developed by LeVeque (1997, 2002), is an open source tsunami model approved by the United States National Tsunami Hazard Mitigation Program (NTHMP). It has been validated by comparing real and artificial data (runup, inundation and flow velocity) with model results (Arcos and LeVeque 2015, Gonzalez et al. 2011, LeVeque et al. 2011, Berger et al. 2011, George 2008, and LeVeque and George 2008). GeoClaw uses the finite volume to solve the two dimensional nonlinear shallow water equations in conservative form:

$$h_t + (uh)_x + (vh)_y = 0 \quad (2-5)$$

$$(hu)_t + \left(hu^2 + \frac{1}{2} gh^2 \right)_x + (huv)_y = -ghB_x - Dhu \quad (2-6)$$

$$(hv)_t + (huv)_x + \left(hv^2 + \frac{1}{2} gh^2 \right)_y = -ghB_y - Dhv \quad (2-7)$$

Where:

$h(x, y, t)$ the fluid depth, $u(x, y, t)$ and $v(x, y, t)$ are the depth-averaged velocities, $B(x, y, t)$ is the topography or bathymetry and $D(h, u, v)$ is the drag coefficient computed by equation 2-4 with the Manning coefficient, $n=0.025$ constant throughout the grid. For a detailed description of GeoClaw refer to LeVeque (2002) and the other references provided above.

The initial condition used in both models is an initial sea-surface deformation based on Yokota et al. (2011). This source model was created by carrying out a quadruple joint inversion of the strong motion, teleseismic, geodetic and tsunami datasets. The resulting model has a maximum

co-seismic slip of approximately 35 m and a seismic moment of 4.2×10^{22} Nm, which yields $M_w = 9.0$.

2.4 RESULTS: INTER-MODEL COMPARISON

A 30m resolution grid was used for the inter-model comparison analysis. Figure 2.1 shows the maximum free surface elevation during the Tohoku tsunami event for MOST and GeoClaw. Both models predict that higher free surface elevations occur at the central part of the Sendai plain, around 38.20° N 140.975° E, with maximum wave amplitudes ranging from 8-12m. Both models agree relatively well with each other when predicting sea surface elevation near the shoreline, with MOST yielding slightly higher predictions.

For consistency purposes, 7 runup measurements from the field data were removed from the analysis, given in Table 2.1. These runup measurements were located very close to the shoreline and led to an irregular inundation line when combined with the other runup points. A total of 46 runup measurements were used from the Sendai plain in this analysis. Table 2.2 presents some statistics from the field data and model predictions. The predicted average distance the wave front traveled inland was 4460m and 4740m from MOST and GeoClaw respectively, compared to 4450m calculated from the field data. The average absolute difference between the field data and the models are also presented in Table 2.2. GeoClaw overestimates the inundation distance by 18% more than MOST in the Sendai plain.

Table 2.1: Field Data Measurements not used in this Study

Lat. ($^\circ$ N)	Lon. ($^\circ$ E)
38.1725	140.9538
38.1822	140.9583
38.2394	140.9533
38.2718	140.9981
38.2724	140.9980
38.2799	141.0506
38.2799	141.0484

Table 2.2: Average Inundation Distance from Field Measurements and Models

	MOST	GeoClaw	Field Data
Avg. (m)	4460.5	4739.3	4451.5
Max. (m)	6246.4	6562.4	5947.0
Min. (m)	1993.3	2746.9	2107.3
Avg. Abs. Diff. (m)*	525.2	644.3	N/A

*Average absolute difference, between field data and model predictions.

Figure 2.2 (left panel) shows the field data runup measurements and the predicted runup by both models. Average runup from the 44 field data measurements is 1.89 m with a standard deviation of 0.70 m while the average runup calculated by MOST and GeoClaw is 3.01 m and 3.34 m respectively. Thus, much of the model runup results lay approximately 2 to 3 standard deviations

away from the mean of the field data. The runup standard deviation for both models is 0.16 m and 0.33 m for MOST and GeoClaw respectively. Figure 2.2 (right panel) shows the inundation line predicted by both models and the field data runup height measurements at the Sendai plain (38.10° N to 38.28° N). Both models provide a reasonably accurate prediction of the inundation line. This would seem to indicate an inconsistency, in that the inundation line is well predicted, but the runup elevation is not; this will be addressed later in this section.

Figure 2.3 shows the probability density function (pdf) of the runup height from the field data and the models. This pdf, and all pdf's to be presented in this paper, are generated using all relevant field or modeled data between 38.10° N to 38.28° N along the Sendia plain. The model distributions have a similar shape with means within 10% of each other, but it can be clearly noted that they overestimate the observed runup. To further analyze the runup predicted by both models, we compared the field data runup height measurements with the elevation from the numerical topographic grid at the location of the runup measurements. The Sendai 30m resolution topography was used in this analysis. Figure 2.4 presents a histogram of the estimated differences. It shows that most of the differences range between (-3m) to (-1m). This indicates that there is some error in the topography, one that cannot be simply attributed to a datum inconsistency, due to the spread of the histogram. The differences between runup elevations and topographic grid elevations would also indicate that it should not be possible for a model to agree with both the inundation line and the runup elevation when using this GSI topography data. Such errors are particularly significant for flat coastal areas such as the Sendia Plain.

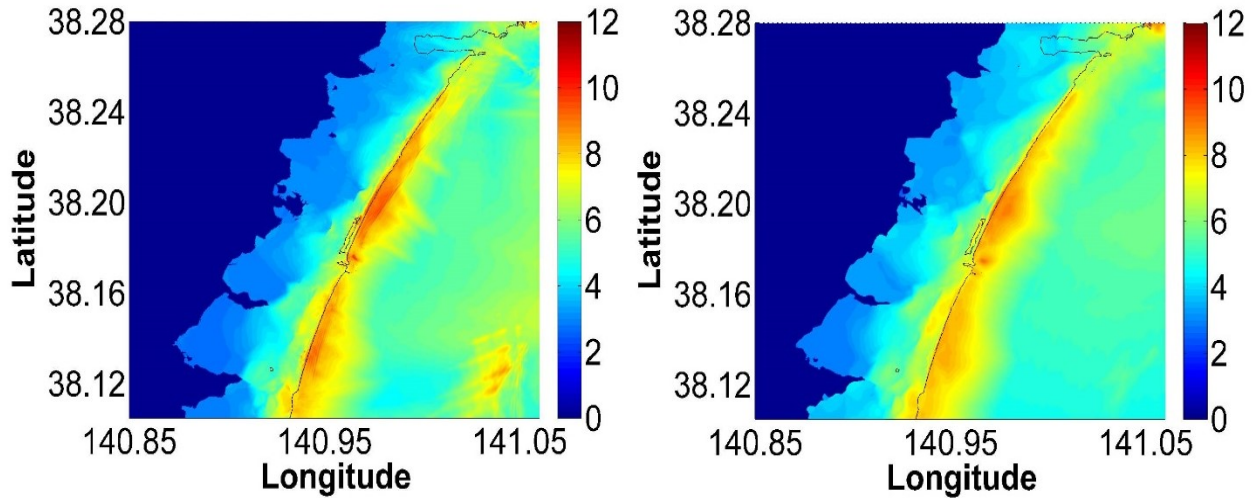


Figure 2.1: Maximum tsunami amplitudes (m) predicted by MOST (left panel) and GeoClaw (right panel) in the Sendai plain.

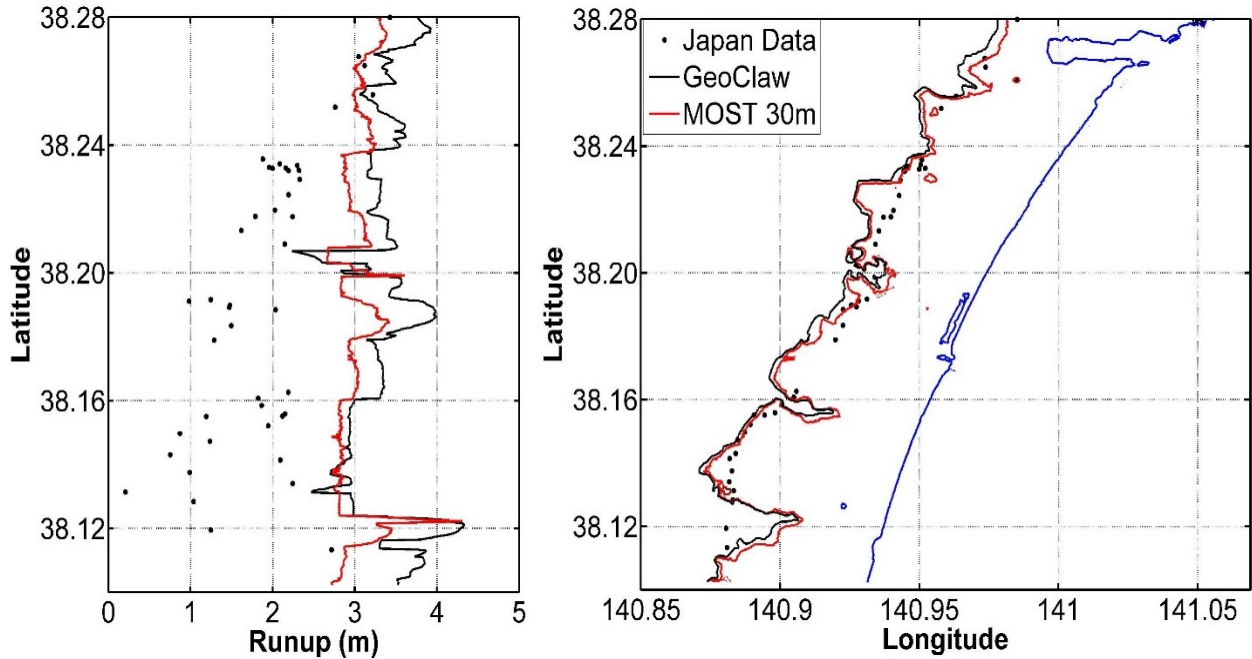


Figure 2.2: Comparison of runup height measurements and inundation line between data, MOST and GeoClaw during the 2011 Tohoku event in the Sendai plain.

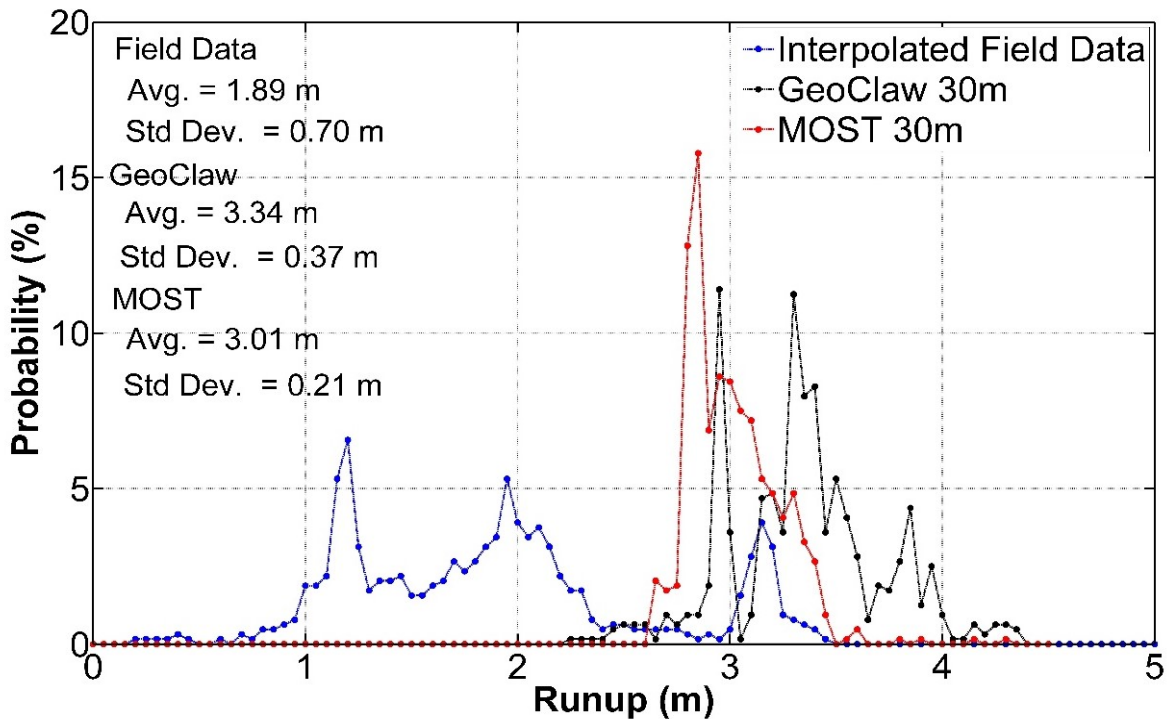


Figure 2.3: Comparison of the runup heights probability density functions between the interpolated field data, MOST and GeoClaw models.

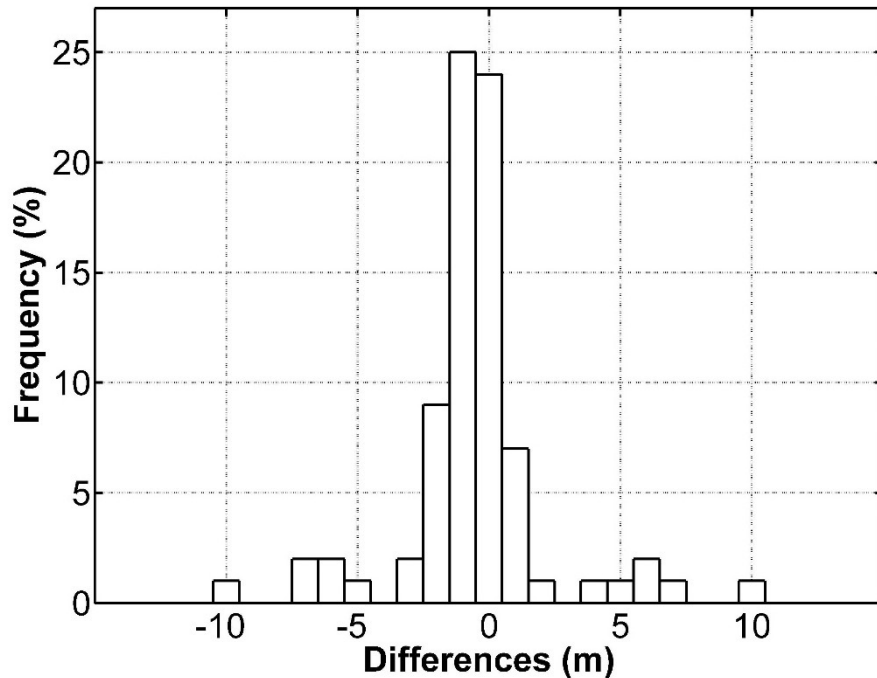


Figure 2.4: Estimated differences between field data runup heights and the topographic elevations from the numerical grid at the location of the runup measurement

In addition to flow depths, tsunami flow velocities have to be analyzed to understand the tsunami hazard at a particular location. For example, Synolakis (2004) stated that currents are more destructive than wave height amplitudes during many tsunami events. Figure 2.5 presents the maximum flow velocities predicted by MOST and GeoClaw, respectively, in the Sendai plain. Both models agree on their predictions and locations of high flow velocities. They also both show a rather complex profile of overland flow velocity, with a number of local maxima. These local maxima are due to topographic features and properties of the incident wave form.

Koshimura and Hayashi (2012) measured the tsunami flow velocities at 4 different locations in the Sendai plain. Figure 2.6 shows the modeled tsunami flow velocities and the field measurements at these locations. Both models under-predict the flow velocity at F1 which is close to the coastline and over predict at Y1 and K3 which are further inland. Some of the reasons that may cause a numerical model to overestimate or underestimate flow velocity measurements are: complex and unresolved bathymetry/topography, improper friction coefficients, no inclusion of tides, and numerical dispersion and dissipation errors. A higher friction coefficient, perhaps more appropriate to rice paddies (e.g. $n=0.035$), would likely decrease flow speeds further inland, which is the area with largest model-data discrepancy.

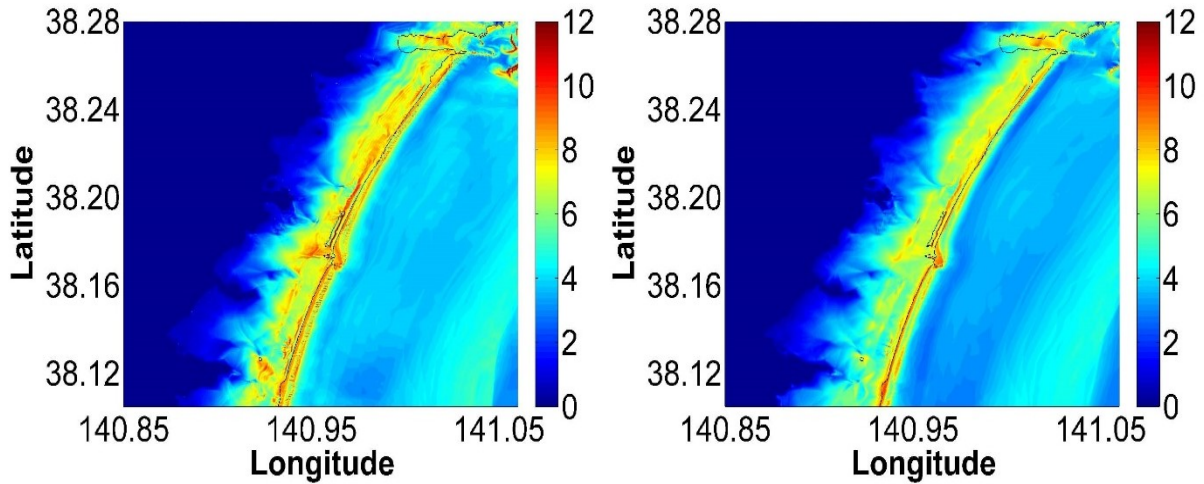


Figure 2.5: Maximum flow velocities predicted by MOST (left panel) and GeoClaw (right panel).

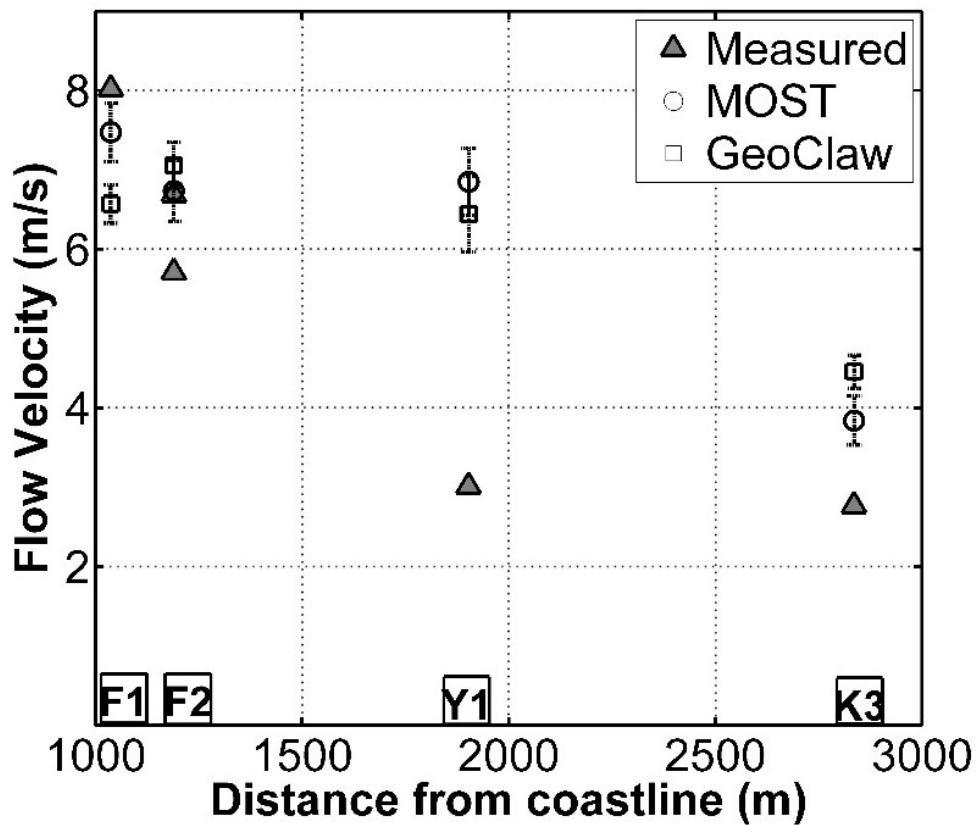


Figure 2.6: Comparison of maximum flow velocities at the Sendai plain between Koshimura and Hayashi (2012) measurements (gray triangles), MOST predictions (circles) and GeoClaw predictions (squares). The vertical bars on the model data provide the standard deviation of the predictions in the measurement window. At F2, two measurements were taken.

Figure 2.7 shows a comparison of the probability density functions of modeled maximum shoreline flow velocity and flow velocity at the 1 meter inland flow depth. These two locations are meant to represent limits of the overland flow area; one comparison at the shoreline and another near the inundation limit, but still at a significant flow depth. Since there is no available data at these locations it is very difficult to assess the model accuracy. Many of the model velocity predictions at the shoreline are between 5-9 m/s, with means of 7.30 and 7.34 m/s for GeoClaw and MOST respectively. The shapes of the shoreline flow velocity pdfs tend to agree well with small differences in their means. Figure 2.7 (bottom panel) shows that both models agree well when predicting the maximum flow velocities at the 1 meter flow depth. The peak of the GeoClaw distribution is located around 1.63 m/s and with a mean of 1.60 m/s while the distribution peak for MOST is located around 1.20 m/s with a mean of 1.63 m/s.

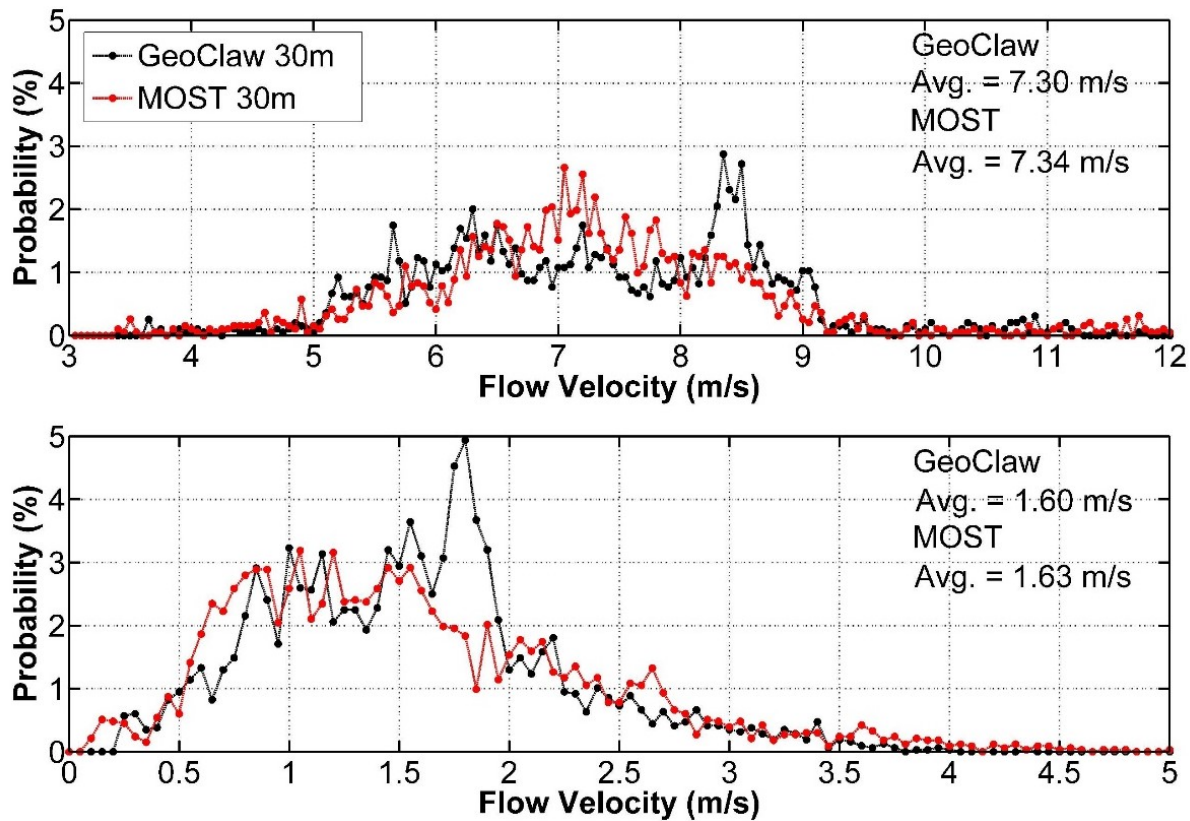


Figure 2.7: (Top panel) Comparison between GeoClaw and MOST probability density functions of maximum shoreline flow velocities and (bottom panel) 1 meter depth maximum flow velocities at the Sendai plain.

2.5 MODEL VARIABILITY AND UNCERTAINTIES

Unquantified uncertainties and variabilities within a model can lead to unknown errors in a THA. In this section, we use MOST to further explore and understand the possible sources of error within a model. For this part of the analysis, 4 inundation grids (1 arc-sec, 0.67 arc-sec, 0.50 arc-sec and 0.33 arc-sec) were used to compare inundation, runup and velocity predictions made by the MOST model. As was previously mentioned, finer grids were created by interpolating the 1

arc-sec topography data. Figure 2.8 shows a pdf of the runup height calculations from the different grids. Both runup and inundation line predictions numerically converge within the tested grid sizes. There are small deviations in the inundation line and runup calculations when using different grid resolutions (30m-10m). In this case, it would seem reasonable to conclude that there is no need to use inundation grids finer than 30m when calculating runup and inundation lines.

Figure 2.9 shows a comparison of maximum shoreline flow velocity pdf's and 1 meter flow depth maximum velocity pdf's for the different grid resolutions. Averages for shoreline velocities are around 7.50 m/s and for 1 meter flow depth, velocities are around 1.70 m/s. While there appears to be numerical convergence between the 30m, 20 m, and 15 m resolution simulations at the shoreline, the 10m resolution grid diverges, with an average maximum velocity of 8.03 m/s. While this divergence is relatively small with a change of 7% in mean values between the 15 m and 10 m results, it is a difference that is not easy to reconcile. From inspection of the results, this variance between the 15 m and 10 m results appears to be driven by a difference in the prediction of the steep front of the incoming bore, and with the understanding that breaking in this model is controlled through numerical dissipation, it is difficult to assess whether this variance is physical (better resolution of the process) or numerical (different numerical errors). Stable numerical results were not achievable for grid sizes less than 10 m. Such a divergence with finer resolutions is not found at the inland location.

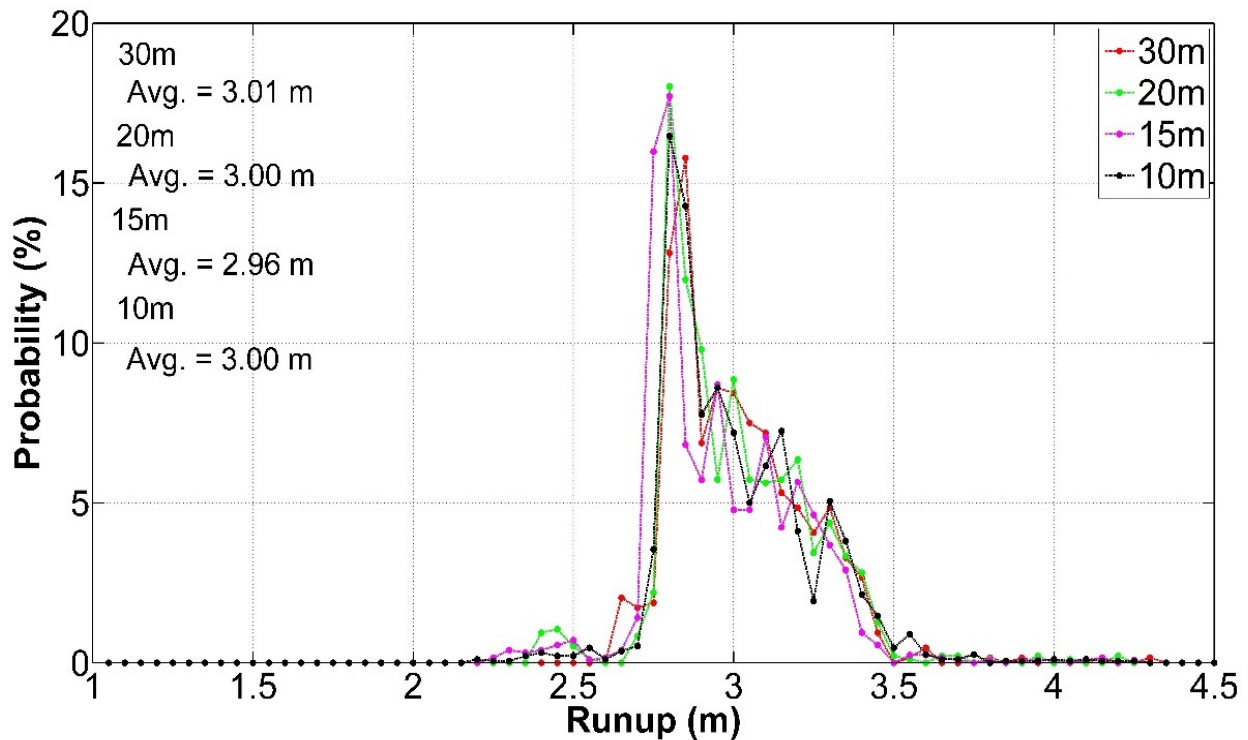


Figure 2.8: Comparison of the runup heights probability density functions between the 4 different grid resolutions using MOST.

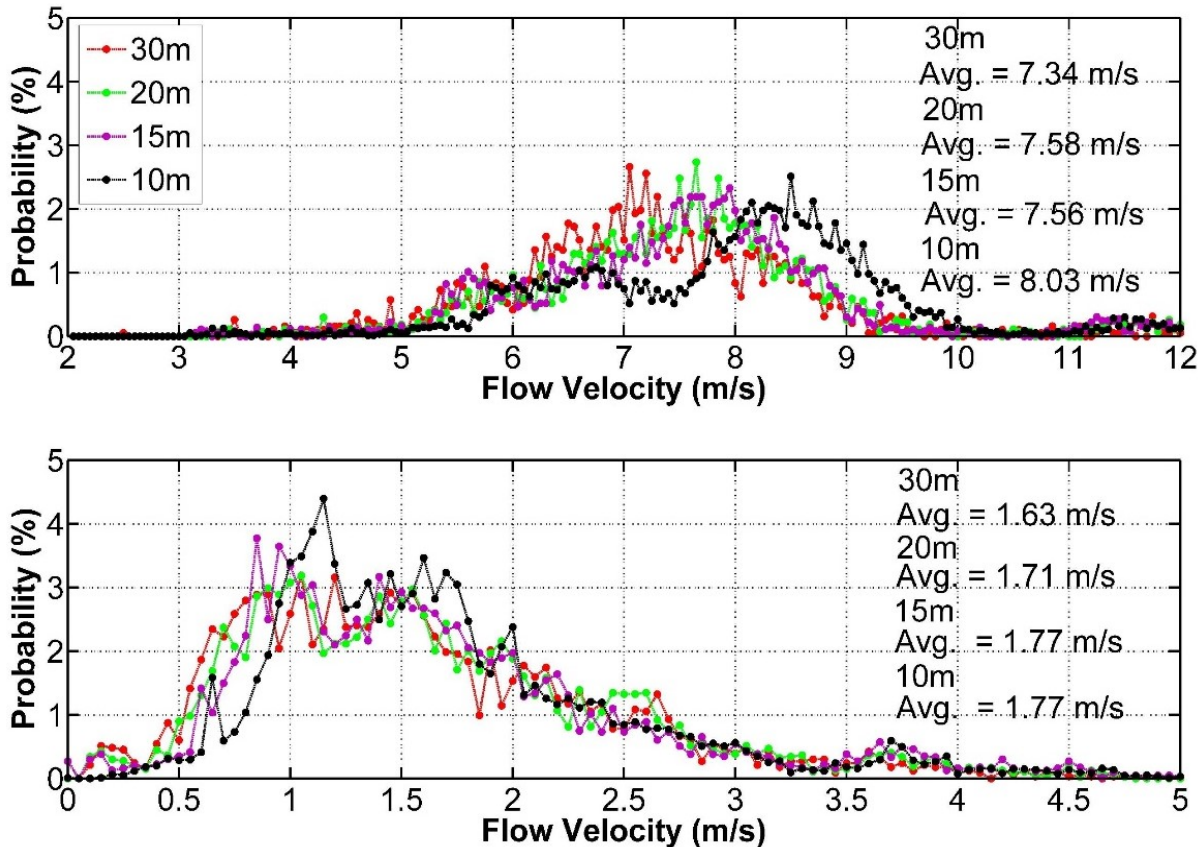


Figure 2.9: (Top panel) Comparison of the maximum shoreline flow velocities probability density functions and (bottom panel) 1 meter depth maximum flow velocities probability density functions between the 4 different grid resolutions using MOST.

Figure 2.10 shows the calculated mean flow velocity at 6 different flow depths (where 6m corresponds to approximately the shoreline). It is very interesting to note that the means seem to converge at lower flow depths. Also, the greatest increase in flow velocity between flow depths was found to be from 2 to 3 meters with an average increase of 2.69 m/s for the tested grids. It is commonly assumed that the Froude number (Fr) is near 1.0 at the shoreline and decreasing inland, but Figure 2.10 shows an irregular Fr profile. The Fr is very near one at the shoreline, greater than 1 (supercritical flow) at flow depths of 3-5 meters and less than 1 (subcritical flow) at flow depths of 1-2 meters.

It is reasonable to expect a steady decrease in velocity, if using the assumption of a simple beach, as the wave front makes its way inland; however the simulation results provided in Figure 2.11 (top panel) show otherwise. Between 400m-1200m inland, maximum velocities (again the mean of the maximum velocities across the studied Sendia Plain) appear to be constant. After analyzing numerical output, we observe that small bathymetry/topography features can cause large changes in predicted flow velocities, producing secondary peaks. Further inland, results from MOST show a steady decline in velocity from 1200m-2800m with a negative slope of about 0.002 for all grid resolutions. Peak flow velocities fluctuate from 6-17 m/s and standard deviations from 0.9-1.7 m/s.

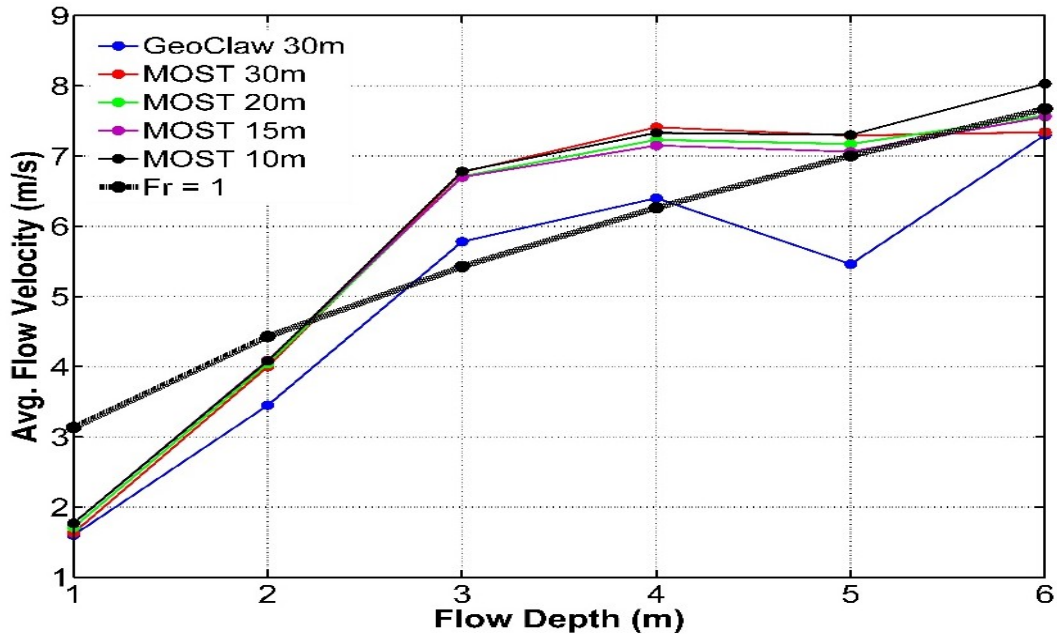


Figure 2.10: Mean flow velocity at different flow depths. The 6 meter flow depth corresponds approximately to the shoreline. The thick black line represents the calculated mean flow velocities using a Froude number of 1.

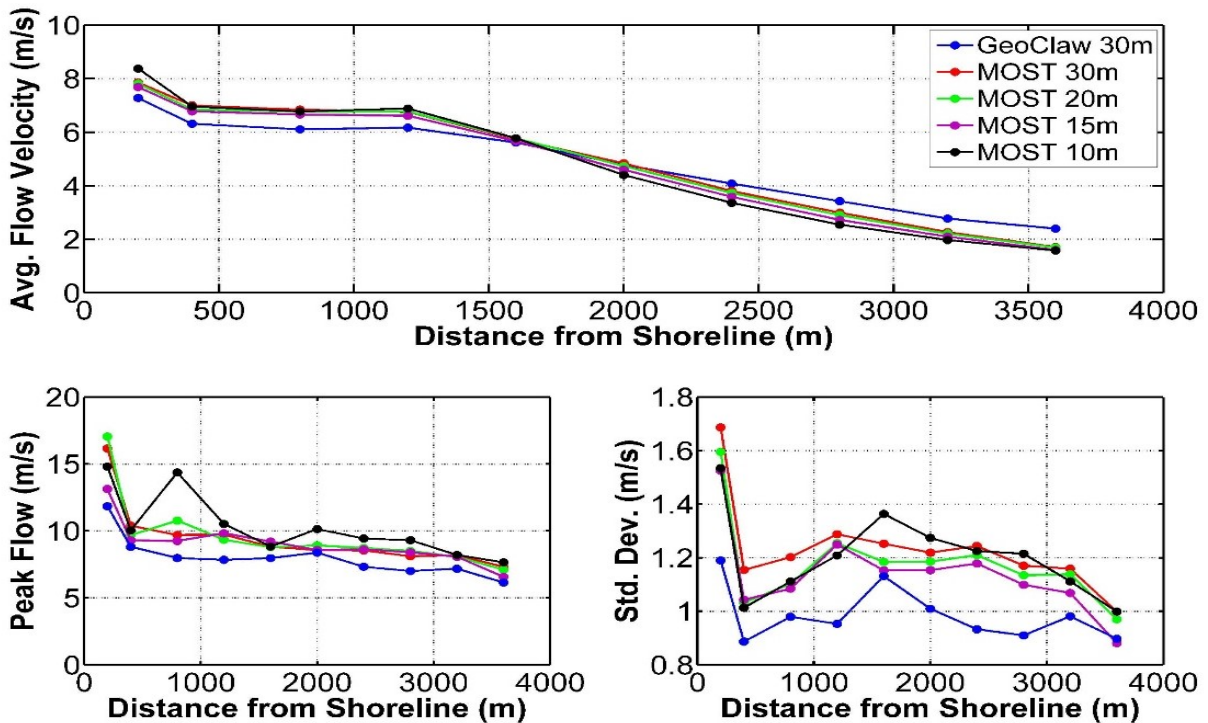


Figure 2.11: Inland maximum flow velocities across shore in the Sendai plain, (top panel) comparison of the average flow velocities between GeoClaw and the 4 different grid resolutions using MOST, (bottom left panel) comparison of peak flow velocities and (bottom right panel) comparison of standard deviations.

2.6 SUMMARY AND MAIN CONCLUSIONS FROM MODEL COMPARISONS

This study presents a comparison between field data and model predictions of the 2011 Tohoku tsunami. Runup elevation was, in general, over predicted by the models. On the other hand, the inundation line predicted by the modeling was in good agreement with the observed, and this inconsistency can be attributed to errors in the topographical data. By comparing observed runup elevation measurements to DEM elevations at the same location, the topography bias ranged from (-3m) to (-1m). This bias is very significant for this particular location since the Sendai Plain is, of course, relatively flat. Thus, with this topography it should not be possible to get both the runup elevation and inundation line correct. For inter-model agreement, both numerical models, MOST and GeoClaw, agree relatively well with each other when predicting maximum sea surface elevation and maximum velocities, with MOST yielding slightly higher predictions for both. Also, it is important to note that the two models predict similar maximum velocity at the shoreline, which is typically the most important place to do so.

When predicting runup heights and inundation lines with MOST, numerical convergence was achieved using the 30m resolution inundation grid. It can be suggested that grids finer than 30m resolution are not necessary when calculating these products at this particular location. Generally, when trying to simulate velocities, it is recommended to use higher resolution topography as small local changes in bathymetry/topography can cause similarly large local changes in the speed. Predictions of overland flow showed that the Froude number varies at different flow depths, contrary from what is commonly assumed. At flow depths of 3-5m the flow is considered supercritical, which indicates that speed would increase in the presence of buildings or structures. Finally, it was expected that the maximum flow velocity would decrease as the wave makes its way inland, but this pattern was not obvious between the 400m and 1200m contour lines, as complexities in the topography and flooding waves obscure this idealized expectation.

3.0 EVALUATION OF SITE-SPECIFIC TSUNAMI HAZARD

In order to determine the hydrodynamic loads on a structure, the site-specific hazard (SSH) must be provided and presented in a format consistent with the loading calculation approach. The SSH analysis provides hydrodynamic flow properties that are needed in the loading calculations, such as maximum flow depth, maximum flow speed, and the time evolution (or time series) of flow depth and flow speed. The general procedure for determining SSH is as follows:

1. A location (or locations) of interest must be specified where SSH hydrodynamic properties are desired
2. Using the tsunami inundation database, information regarding the 1000-yr return period tsunami hazard in the vicinity of the location is found; this information may include inundation limits, offshore tsunami properties, and subsidence values
3. With the database information, SSH can be determined

This document outlines two different methodologies, or “Levels”, for determination of SSH. A Level 1 analysis methodology is developed in order to provide a relatively simple, rapid, and conservative estimate of the local tsunami hydrodynamics. A Level 2 approach is also provided, which permits the user to employ state-of-the-art numerical simulation tools. The decision of which Level of SSH to use for a project is given as:

1. A Level 1 analysis should be performed for the design location
2. If the user desires a more refined estimate of the SSH, a Level 2 analysis may be utilized. The hydrodynamic predictions of a Level 2 analysis shall replace without limit the predictions of a Level 1 analysis. If the Level 2 SSH effects are more severe than the Level 1 effects, then the Level 2 results must be used.

General details of the two “Levels” are provided in this Chapter.

3.1 METHODOLOGY: INUNDATION DATABASE

An inundation database has been created as part of this TPF project, specifically as the deliverable in Task WG1.1. In this task, offshore probabilistic hazard is determined at the 1000-year return period, and inundation scenarios at this hazard level are performed. The simulations use a variant of the model GeoClaw. GeoClaw, developed by LeVeque (1997, 2002), is an open source tsunami model approved by the United States National Tsunami Hazard Mitigation Program (NTHMP). It has been validated by comparing real and artificial data (runup, inundation and flow velocity) with model results (Arcos and LeVeque 2015, Gonzalez et al. 2011, LeVeque et al. 2011, Berger et al. 2011, George 2008, and LeVeque and George 2008). GeoClaw uses the finite volume method to solve the two dimensional nonlinear shallow water equations in conservative form:

$$h_t + (uh)_x + (vh)_y = 0 \quad (3-1)$$

$$(hu)_t + \left(hu^2 + \frac{1}{2}gh^2\right)_x + (huv)_y = -ghB_x - Dhu \quad (3-2)$$

$$(hv)_t + (huv)_x + \left(hv^2 + \frac{1}{2}gh^2\right)_y = -ghB_y - Dhv \quad (3-3)$$

Where:

$h(x, y, t)$ is the fluid depth, $u(x, y, t)$ and $v(x, y, t)$ are the depth-averaged velocities, $B(x, y, t)$ is the topography or bathymetry and $D(h, u, v)$ is the drag coefficient:

$$D(h, u, v) = n^2 gh^{-4/3} \sqrt{u^2 + v^2} \quad (3-4)$$

In the inundation database simulations, the drag is computed with the Manning coefficient $n=0.025$ constant throughout the grid. For a detailed description of GeoClaw refer to LeVeque (2002) and the other references provided above. Complete details of the inundation database are provided in a companion technical report, as part of the Task WG1.1 deliverable.

3.2 LEVEL 1 ANALYSIS: TRANSECT APPROACH

To provide a relatively simple, prescriptive-type approach to determine the SSH, the transect analysis is adopted. In general, the transect approach is described by the following steps:

1. Creation of a bathymetric transect bounded at a minimum by the pre-tsunami shoreline and the point of maximum inundation, and including the site of interest
2. Use of an approximate hydrodynamic model to determine tsunami properties (flow elevation and speed) at all points along the transect, using information from the tsunami inundation database to initialize the transect calculations. The specific hydrodynamic model used controls how the tsunami properties are calculated.
3. Extraction of tsunami properties at the site

Naturally, any transect analysis will neglect two-dimensional focusing, and any other two-dimensional topographical effect on the tsunami inundation. Therefore, any transect approach must be designed to be conservative. Here, we employ the Energy Grade Line Analysis (EGL) (Kriebel et al., 2017) to predict the tsunami properties across the transect. The EGL has been adopted as the prescriptive approach in ASCE7-16 Chapter 6, and has undergone considerable testing. Statistically, the EGL provides accurate estimates of both maximum flow depth and flow

speed in the statistical mean sense, although the precision of the EGL estimates is ~10% for flow depth and ~2 m/s for flow speed (Kriebel et al., 2017).

The maximum velocity and maximum inundation depth along the ground elevation profile up to the inundation limit shall be determined using the Energy Grade Line Analysis. The orientations of the topographic transect profiles used shall be determined considering discussion in Section 3.3. The ground elevation along a transect, provided at the Mean High Water (MHW) datum in the inundation database, shall be represented as a series of linear sloped segments. The ground elevation should be adjusted to account for subsidence, in the cases that the tsunami is generated by a local earthquake. If using a subsidence value, the runup elevation remains as the value found in the inundation database; the runup elevation (in the Mean High Water, or other, datum) is not changed by the subsidence. Each segment of the transect should be assigned a Manning's coefficient consistent with the equivalent terrain macro-roughness friction of that terrain segment. The Energy Grade Line Analysis shall be performed incrementally in accordance with Eq. (3-5) across the topographic transect in a stepwise procedure. Eq. (3-5) shall be applied across the topographic transect from the runup where the hydraulic head at the inundation limit, X_r , is zero, and the water elevation is equal to the runup, R , by calculating the change in hydraulic head at each increment of terrain segment toward the shoreline until the site of interest is reached, as shown in Figure 3.1 and following the equation:

$$E_{i+1} = E_i - (\phi_i + S_i) \Delta X_i \tag{3-5}$$

Where:

$$E_i = \text{Hydraulic Head at point } i = h_i + U_i^2/2g$$

$$\phi_i = \text{Average ground slope between points } i \text{ and } i+1$$

$$\Delta X_i = X_{i+1} - X_i$$

$$S_i = \text{Friction slope of the energy grade line between points } i \text{ and } i+1 \text{ derived from the Manning equation in inch-pound units, } = (U_i)^2 / ((1.49/n)^2 h_i^{4/3}) =$$

$$g F_n^2 / ((1.49/n)^2 h_i^{1/3}) \quad \text{U.S units}$$

$$g F_n^2 / ((1.00/n)^2 h_i^{1/3}) \quad \text{metric units}$$

In Figure 2.1, the following variables are described:

$$R = \text{Mapped tsunami runup above MHW datum}$$

$$X_r = \text{Mapped inundation distance inland from MHW shoreline}$$

$$x = \text{Horizontal distance inland from MHW shoreline}$$

$$h_i = \text{Inundation depth at point } i$$

$$U = \text{Maximum overland flow velocity}$$

$$F_r = \text{Froude Number} = U/(gh)^{1/2}.$$

Throughout the transect, if any ground elevation between the pre-tsunami shoreline and the inundation limit exceeds the runup elevation, that ground elevation shall be lowered to the runup elevation. This ad-hoc procedure is necessary due to limits in both the transect approach and the EGL calculation procedure.

Velocity shall be determined as a function of inundation distance and flow depth, calibrated to the prescribed Froude number as given by

$$F_r = \alpha \left(1 - \frac{x}{X_r}\right)^{0.5}$$

(3-6)

Where:

A value of the Froude number coefficient, α , of 1.0 shall be used for all cases. The Froude number is a dimensionless hydrodynamic parameter that provides a relative speed of the flow; values above 1.0 indicate highly energetic flow and a flow with a Froude number of 0 is stationary.

Bed roughness in the EGL analysis shall be prescribed using the Manning coefficient “n”. It shall be permitted to use the values listed below or other values based on terrain analysis in the recognized literature.

- Coastal waters, nearshore: $n=0.025-0.03$
- Open land or fields: $n=0.025$
- Buildings of at least urban density: $n=0.04$
- All other cases: $n=0.03$

The user shall perform an EGL analysis across four different transects:

1. A straight-line transect as judged to be orthogonal to the shoreline in the general direction of expected tsunami approach
2. A straight-line transect rotated 10 degrees clockwise about the design location
3. A straight-line transect rotated 10 degrees counter-clockwise about the design location
4. A “riverine” or flow channel-path transect, composed of an arbitrary number of connected, but different orientation segments. The purpose of this transect is to best represent, in the users judgement, the most likely flow path of energy from the pre-tsunami shoreline to the design site. This transect should terminate at the nearest runup point inland of the design site.

The purpose of utilizing four different transects is to partially capture the potential variability of the EGL approach outputs. We have found from testing many different cases that the output of the EGL transect is sensitive to the precise orientation of the line, the runup at the end of the transect, and the relative position of the design location to the shoreline and runup points. For example, it is common to find 25-50% differences in EGL flow speeds at the design location due to a 10 degree rotation of the transect. We propose that the design values of maximum flow depth and maximum flow speed be taken as the average of the middle two values from the four transects. For example, if the site predictions of flow depth and elevation from the four transects are, respectively: [2.0 m, 6.0 m, 7.0 m, 8.0 m] and [2.4 m/s, 7.5 m/s, 4.0 m/s, 2.0 m/s], the design values to be used in the loading calculations would be:

- Design maximum flow depth (m) = $[6.0 + 7.0] / 2 = 6.5$
- Design maximum flow speed (m/s) = $[2.4 + 4.0] / 2 = 3.2$

While this procedure is not likely to represent a statistically robust representation of the median or mean hazard, it does represent a practical and reasonable approach to eliminate obvious outliers from the EGL results. Furthermore, through a great deal of testing, this simple “middle two” approach was also found to prevent the manipulation of a single transect orientation in order to provide the lowest (or greatest) hazard level. Other options for providing a useful EGL approach are listed below, along with the reasons they were not chosen:

- Averaging results from all four of the transects: this option was not chosen as it is common to have a significant outlier (>100% flow depth for example) among the four results, which was a distant estimate from both the other transect results and the database output. Employing an averaging approach that simply discarded such an outlier was desired.
- Adding additional transects, such as having the Matlab code automatically calculate ~100 different transects between the +/- 10 degree sector: while such an approach did appear to add robustness to the result, it was deemed impractical for users. Such an approach should be revisited when/if an online web transect tool is developed.
- Weighting different transects results unequally: while it could be argued, for example, that the riverine transect is the most physically reasonable flow path for the design tsunami, it was decided against recommending weightings for specific transects. In particular, such a weighting approach is difficult to reconcile with the “middle two” approach, which tend to be any two random transects out of four.

In general, other options that added some layer of logic or complexity were considered undesirable, given the highly simple and physically-coarse nature of the EGL model itself. Directing users to calculate four transects and use a straightforward “middle” value, provided an acceptable compromise of output stability and implementation simplicity.

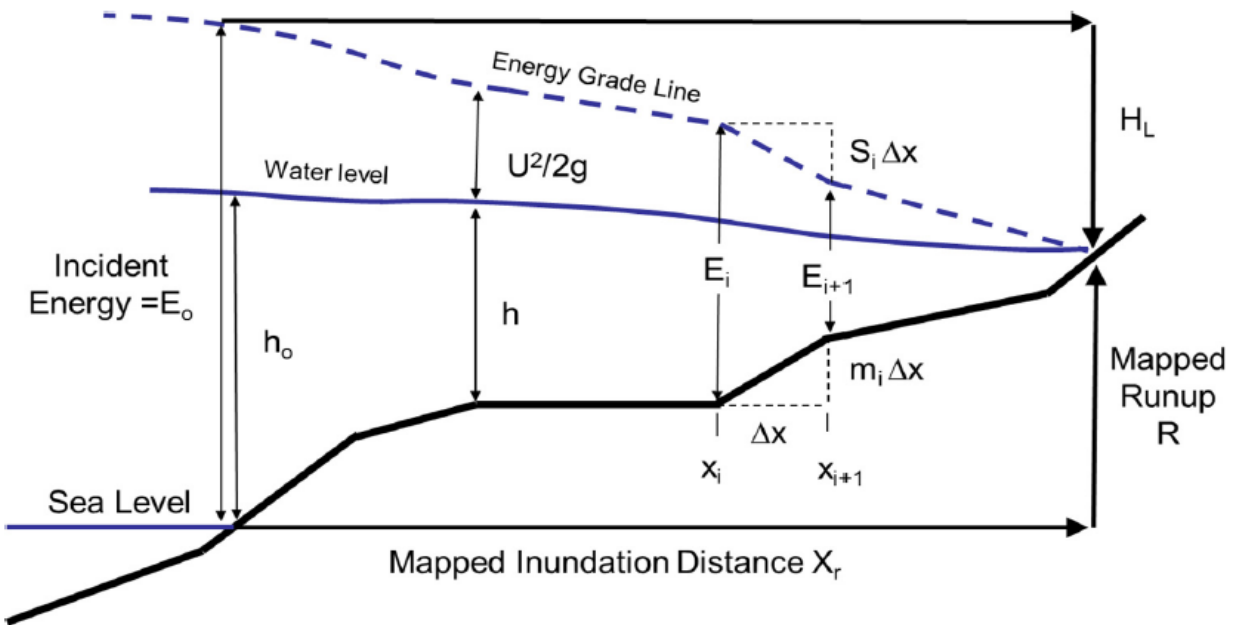


Figure 3.1: Illustration of energy method across inundated transect; incident tsunami flow is from left to right (from Kriebel et al., 2017).

3.3 DEVELOPMENT OF TRANSECT CALCULATION TOOL

In order to facilitate the use of the EGL transect analysis approach, we have developed a Matlab-based program (Lynett and Thio, 2020). This software is included as a Digital Appendix, and can be downloaded here: <https://www.doi.org/10.9753/TPF.suppl.1>.

The file in the link above is a “RAR” file compression archive with a total size of 4.6 GB. The archive contains the following:

- master.m: The main script used to execute the EGL Transect Tool. User would edit this script to examine coordinates of the design site. Script is heavily commented, but would require significant experience in Matlab to fully understand the code.
- check_transects.m, create_transects.m, deg2utm.m, run_EM.m: scripts and function files needed by master.m to run. All files are well commented.
- \runup_data: directory that contains all of the inundation database files. In this directory, the *.xyz files are the raw model output files provided by H.K. Thio, the *.mat files are the Matlab-converted database files, and load_database_files.m is the Matlab script used to convert the .xyz files to .mat files.

To use the Matlab transect software, the user should first open the file “master.m” in the Matlab Editor. Near line 11 in this code, the user will see the following code block:

```
% structure location - input Latitude (degrees North) and
Longitude (degrees East; values will be between -180 and 0 for
US)
```

```

%xs=-124.057108; % longitude CA
%ys=41.556267; % latitude CA
%xs=-122.4350; % longitude CA
%ys=37.47; % latitude CA
%xs=-157.9450; % longitude OAHU
%ys=21.330; % latitude OAHU
%xs=-146.2500; % longitude AK
%ys=61.09; % latitude AK
%xs=-122.4100; % longitude WA
%ys=48.545; % latitude WA
%xs=-124.0660; % longitude OR
%ys=43.7049; % latitude OR

% or, have Matlab prompt for the design site location
disp('USER INPUT: Specify the site information');
ys=input('USER INPUT: Enter site latitude (degrees N, 0-90): ');
xs=input('USER INPUT: Enter site longitude (degrees W, -180-0): ');
');

```

When running this Matlab script, the program will prompt the user to enter the latitude and longitude. Here, the user should set the latitude (variable “ys”) and longitude (variable “xs”) of the design site. Note that the coordinate locations listed above (and in the master.m script) correspond to the example locations discussed later in this report in Section 3. With the desired location assigned to the “xs” and “ys” variables known, the user should run the master.m script.

First, the software searches the inundation database, and attempts to find the finest resolution grid that contains the design site location. The program will either display the name of the found inundation grid, or it will terminate the program with the error:

```

ERROR: Structure location does not exist within the bounds of
      any database grid.

```

If this error appears, the design site location is not included in the inundation database, and some other means of obtaining tsunami hazard information must be sought.

With a found inundation grid that includes the design site location, the software next checks to determine whether the location is in the inundation zone. If the location is found to be outside of the inundation zone (remains dry during the tsunami event), the message

```

ERROR: Structure location is not in tsunami inundation zone

```

is provided and the program terminates. In this case, as the site remains dry, no tsunami hazard and loading calculations would be required.

Next, the user is prompted to generate the “riverine transect”, which is the piecewise-linear transect composed of an arbitrary number of segments. The aim of the riverine transect is to allow the user some flexibility or customization in their expectation of the likely tsunami flow pathway. As the focus of our applications will be for bridges, our sites will tend to be near, or in, channelized, preferential flow pathways. As this is a user-generated transect, some level of local

knowledge of the topography is required. Ideally, the user is familiar with the locale, and can readily identify a likely channel or pathway that the tsunami flow might follow. In the absence of this familiarity, the user should inspect the Matlab-plotted topography surface for any evident channels. If no channels appear to exist in the plotted topography data and no knowledge of preferential pathways exists, the user should then use a single linear segment to connect the site to the nearest shoreline. In the Matlab figure, the inundation grid is plotted showing the ground elevation, as well as the pre-tsunami shoreline (red line) and the tsunami inundation limit (black line). The user should start the riverine transect by left-clicking on a point just offshore of the pre-tsunami shoreline. Then, the user can click on as many points as desired; the transect will be generated by linearly connecting these clicked points. To “snap” a point to the design site, the user should right-click. After snapping to the design site location, the transect should be terminated by clicking on the nearest dry area (inland of the black line). The riverine transect should cross the pre-tsunami shoreline only once and should cross the inundation limit only once. It is noted that the generation of this riverine transect is not unique, in that different users will certainly create different transects. Thus, the user must be guided by some level of expert judgement, and be able to justify the configuration of the riverine transect based on physical inspection of the topography.

Following the creation of the riverine transect, the straight-line transects are generated. The user will be prompted to:

Click on Open Ocean Shoreline Location to be used to Generate
Straight Transects

and should click on a location offshore of the pre-tsunami shoreline. A linear transect will be generated which passes through this clicked point and the design site location; additionally, the two +/- 10 degree transects will be constructed automatically as well.

At this point, the orientation for all four transects is known, and ground elevation profiles along the transects can be generated. The Matlab code also checks the ground elevation along the transect relative to the runup elevation, and makes any needed modifications in accordance with Section 2.2. At this time, subsidence is not included in any of the Matlab calculations, as these values have not been provided. Finally, the EGL calculations can proceed along the four transects.

The results of the EGL calculations are displayed on the Matlab figure, showing maximum flow depth, elevation, and speed for each transect. The design values for each parameter (middle two average) is shown as well. If the user is content with the orientation of the straight-line transects, then the user has completed the Level 1 tsunami hazard assessment. If the user would like to alter the straight-line transect orientation, they should click on another location offshore of the pre-tsunami shoreline, and the EGL calculations will update.

3.4 GENERAL CONFIGURATION GUIDELINES FOR LEVEL 2 ANALYSIS

A Level 2 analysis requires the use of a detailed hydrodynamic model which has been verified for use with tsunami mapping studies. Specifically,

- The inundation model shall be validated using the certification criteria of the National Tsunami Hazard Mitigation Program (NTHMP) by providing satisfactory performance in a series of benchmark tests of known data sets designated by the Tsunami Model Validation Advisory Group in NOAA Technical Memorandum OAR PMEL-135, Standards, Criteria, and Procedures for NOAA Evaluation of Tsunami Numerical Models.

For a Level 2 analysis to be valid, the bathymetry/topography and hydrodynamic flow must be adequately resolved. The numerical resolution for the finest resolution grid covering the design location must be 10-m (or 1/3 arcsec) or less. Bathymetry/topography should not include structures in the elevation data; these datasets should be “bare-earth” elevations. Buildings, vegetation and other roughness elements that may exist in the inundation area may be approximated through a Mannings “n” Roughness coefficient, following those given in Section 2.2. Unless otherwise determined for the site, a default “n” value of 0.025-0.030 shall be used for the ocean bottom and on land.

A Level 2 analysis should start with the specification of a scenario earthquake, or a set of scenario earthquakes. The earthquake properties should be used to specify the initial tsunami, and for a local earthquake values of subsidence. The resulting initial tsunami condition must provide a hazard that is consistent with the 1000-year return period level as given in the inundation database. This hazard-consistency requires that

- The incident maximum tsunami crest elevation and characteristic period of the waveform with the maximum crest elevation at the 100-m offshore depth contour be equal to or exceed those used to generate the tsunami inundation database, or
- In the case that the offshore hazard is unavailable or otherwise inapplicable, the runup elevations in the vicinity of the site must be equal to or exceed the corresponding values from the tsunami inundation database

In addition to providing documentation that the Level 2 analysis is hazard-consistent with the tsunami inundation dataset, output from a Level 2 analysis should at a minimum include values of maximum flow depth and flow speed at the site. Other details of simulation configuration not specifically discussed in this section, such as appropriate vertical datum and incorporation of subsidence, follow that provided in Section 2.2.

3.5 ESTIMATION OF FLOW DIRECTION

When determining the forces and moments on a bridge, the direction of the flow relative to the bridge deck is an important parameter. In general, there will be two potential approaches for determining the flow direction angle:

1. The user has performed a Level 2 analysis, and has saved the flow directions, in addition to the other necessary hydrodynamic information. In this case, the user shall take the design flow direction angle to be the flow direction angle at the time of maximum currents. Flow direction angle is defined as the angle of the vector composed of the u and v velocity components.

2. The user has performed a Level 1 analysis and/or has performed a Level 2 analysis but flow direction has not been saved. In this case, two different flow direction angles shall be examined:
 - a) The shore-normal direction; the orientation judged to be orthogonal to the shoreline in the general direction of expected tsunami approach. If a Level 1 analysis has been performed, this angle would be equal to the angle of the shore-orthogonal, straight-line transect.
 - b) The along channel direction; the orientation judged to be parallel to the banks of the channel over which the bridge is constructed. If the bridge has no obvious channel associated with its purpose, then this angle need not be used for any calculations.

3.6 RECOMMENDED LOAD CASES

As a minimum, the following two Inundation Load Cases shall be evaluated:

1. Load Case 1: Depth at two-thirds of maximum inundation depth when the maximum velocity shall be assumed to occur in either incoming or receding directions.
2. Load Case 2: Maximum inundation depth when velocity shall be assumed at 80% of maximum in either incoming or receding directions.

The maximum inundation depth and velocity are taken from either the Level 1 or Level 2 analysis. If time history records of flow depth, speed, and direction are available from a Level 2 analysis at the site, those records may be used to generate a loading time record for the entire event, and may be used in place of the two Load Cases noted above.

3.7 SITE-SPECIFIC HAZARD DETERMINATION EXAMPLES: HAWAII

This example looks at the southern coastline of Oahu, with coordinates:

- Latitude: -157.945
- Longitude: 21.33

Figure 3.2 summarizes the transect analysis. In this figure, the pre-tsunami shoreline is shown by the red dots, and the 1000-yr tsunami inundation limit is given by the black dots. The output from the transect analyses are given on the right side of the figure. For this location, the inundation database does NOT contain high-resolution mapping results (<30 m resolution), and thus the noted “Database Design Values” SHOULD NOT be used instead of the EGL transect results.

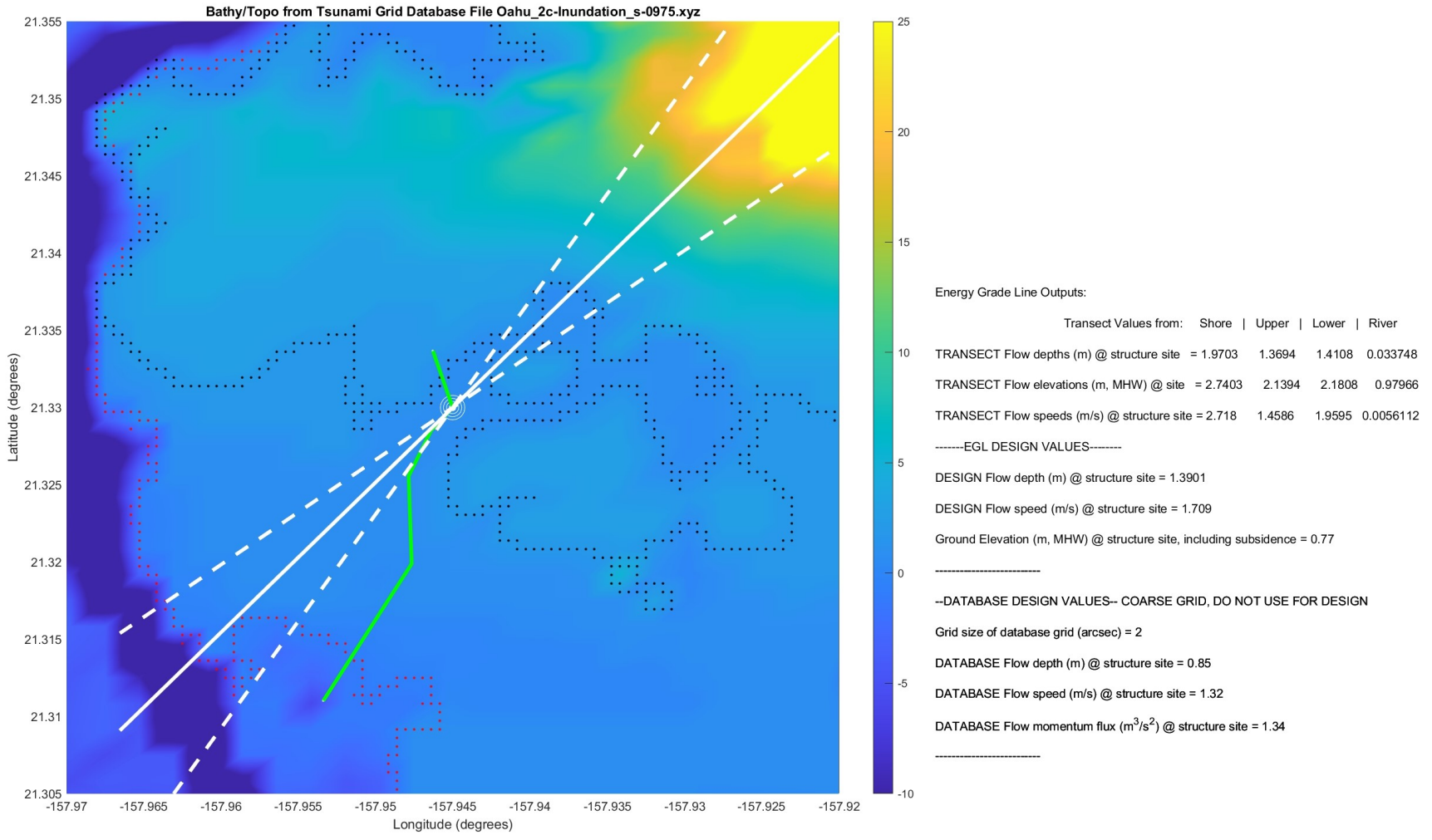


Figure 3.2: EGL transect analysis example for a location in Hawaii.

3.8 SITE-SPECIFIC HAZARD DETERMINATION EXAMPLES: ALASKA

This example looks at a segment of coastline near Valdez, with coordinates:

- Latitude: 213.75
- Longitude: 61.09

Figure 3.3 summarizes the transect analysis. In this figure, the pre-tsunami shoreline is shown by the red dots, and the 1000-yr tsunami inundation limit is given by the black dots. The output from the transect analyses are given on the right side of the figure. For this location, the inundation database does NOT contain high-resolution mapping results (<30 m resolution), and thus the noted “Database Design Values” SHOULD NOT be used instead of the EGL transect results.

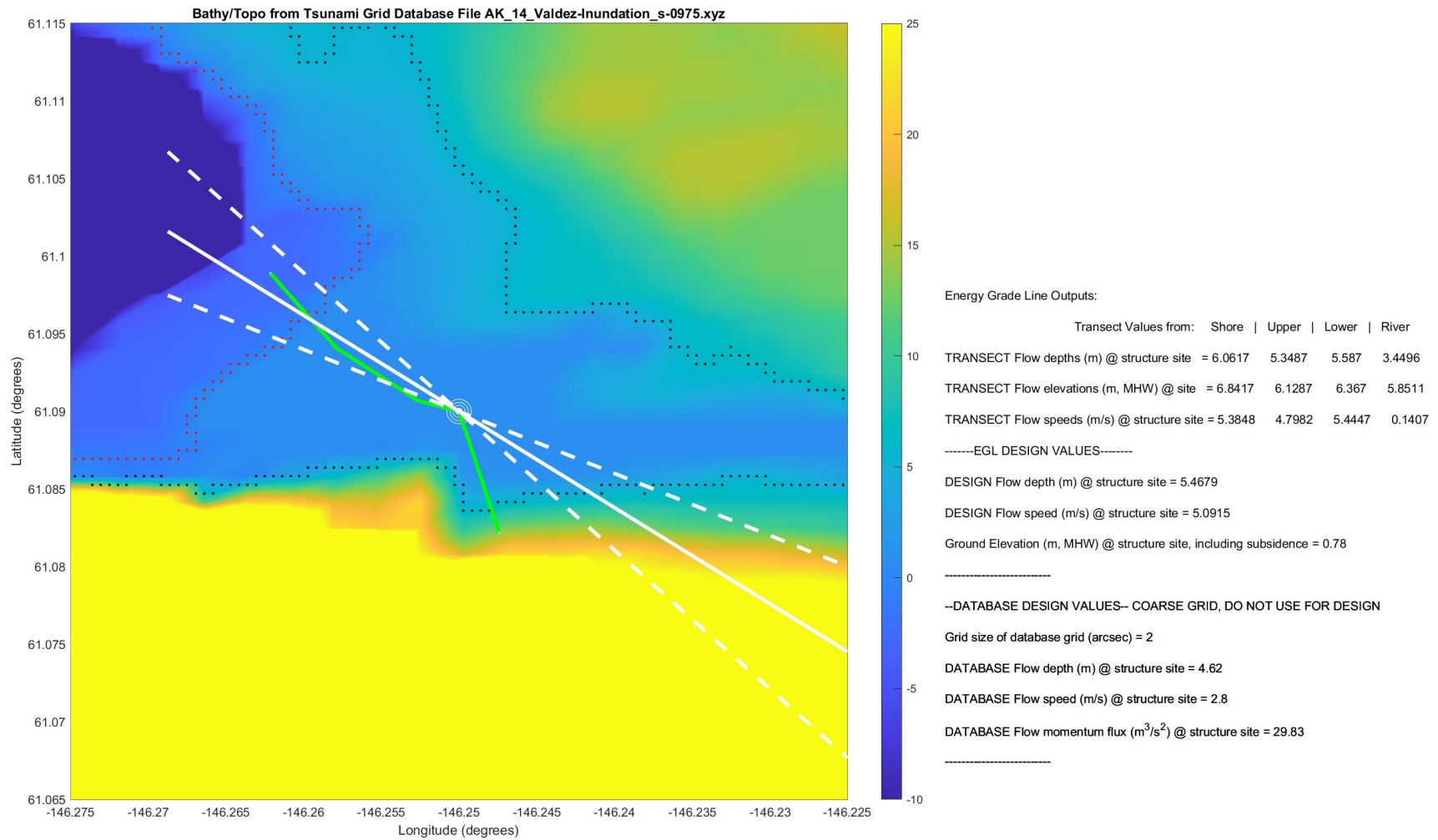


Figure 3.3: EGL transect analysis example for a location in Alaska.

3.9 SITE-SPECIFIC HAZARD DETERMINATION EXAMPLES: WASHINGTON

This example looks at the coastline of Washington, with coordinates:

- Latitude: -122.41
- Longitude: 48.545

Figure 3.4 summarizes the transect analysis. In this figure, the pre-tsunami shoreline is shown by the red dots, and the 1000-yr tsunami inundation limit is given by the black dots. The output from the transect analyses are given on the right side of the figure. For this location, the inundation database does NOT contain high-resolution mapping results (<30 m resolution), and thus the noted “Database Design Values” SHOULD NOT be used instead of the EGL transect results.

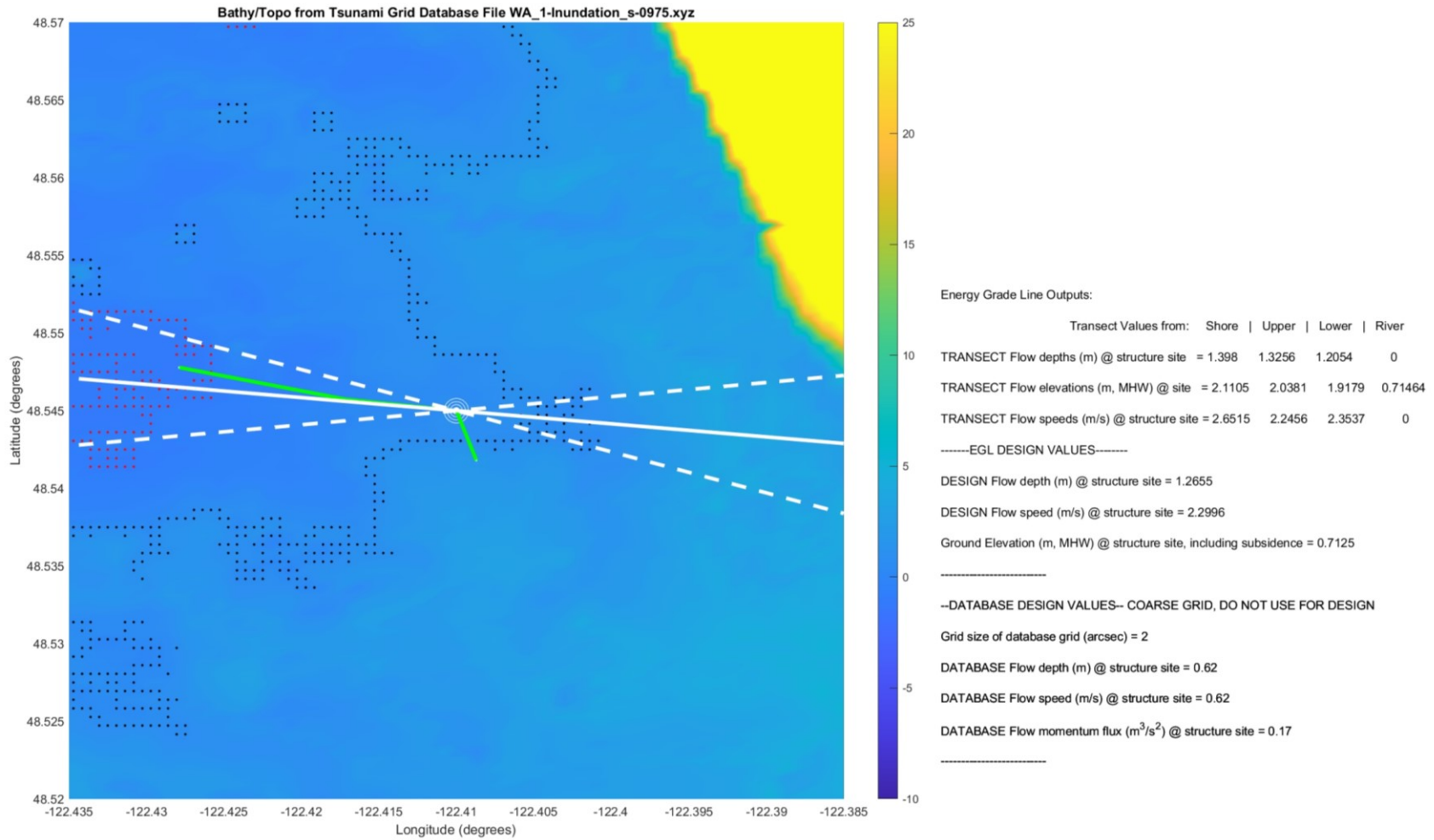


Figure 3.4: EGL transect analysis example for a location in Washington

3.10 SITE-SPECIFIC HAZARD DETERMINATION EXAMPLES: OREGON

This example looks at the coastline of Oregon near Reedsport, with coordinates:

- Latitude: -124.066
- Longitude: 43.7049

Figure 3.5 summarizes the transect analysis. In this figure, the pre-tsunami shoreline is shown by the red dots, and the 1000-yr tsunami inundation limit is given by the black dots. The output from the transect analyses are given on the right side of the figure. For this location, the inundation database does contain high-resolution mapping results (<30 m resolution), and thus the noted “Database Design Values” SHOULD be used instead of the EGL transect results.

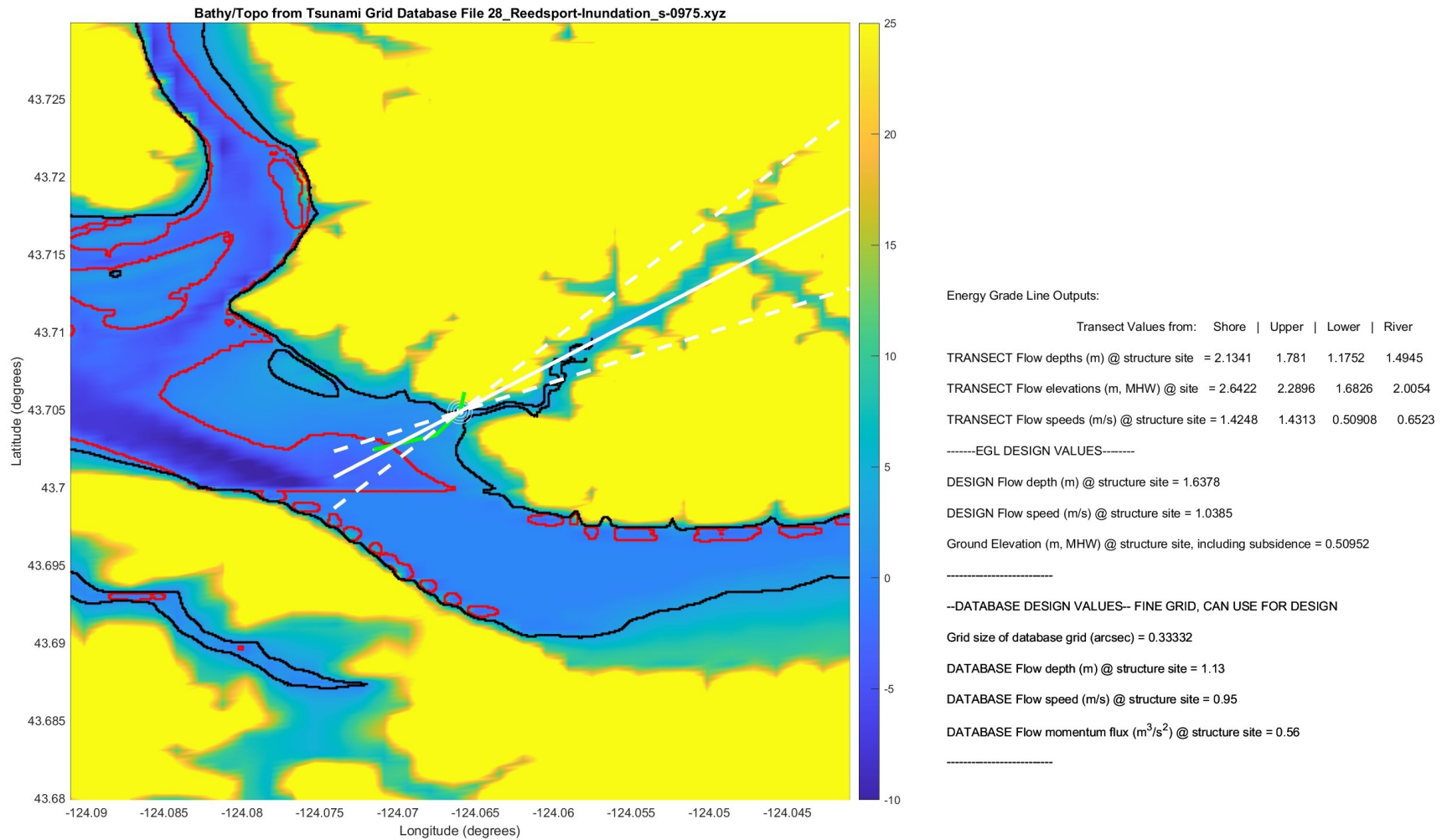


Figure 3.5: EGL transect analysis example for a location in Oregon

3.11 SITE-SPECIFIC HAZARD DETERMINATION EXAMPLES: CALIFORNIA

This example looks at the coastline of California near Half Moon Bay, with coordinates:

- Latitude: -122.4350
- Longitude: 37.47

Figure 3.6 summarizes the transect analysis. In this figure, the pre-tsunami shoreline is shown by the red dots, and the 1000-yr tsunami inundation limit is given by the black dots. The output from the transect analyses are given on the right side of the figure. For this location, the inundation database does contain high-resolution mapping results (<30 m resolution), and thus the noted “Database Design Values” SHOULD be used instead of the EGL transect results. Note that at this location, the Level 2 flow depth and speed are larger than the Level 1 estimates; the Level 2 values should be used for design.

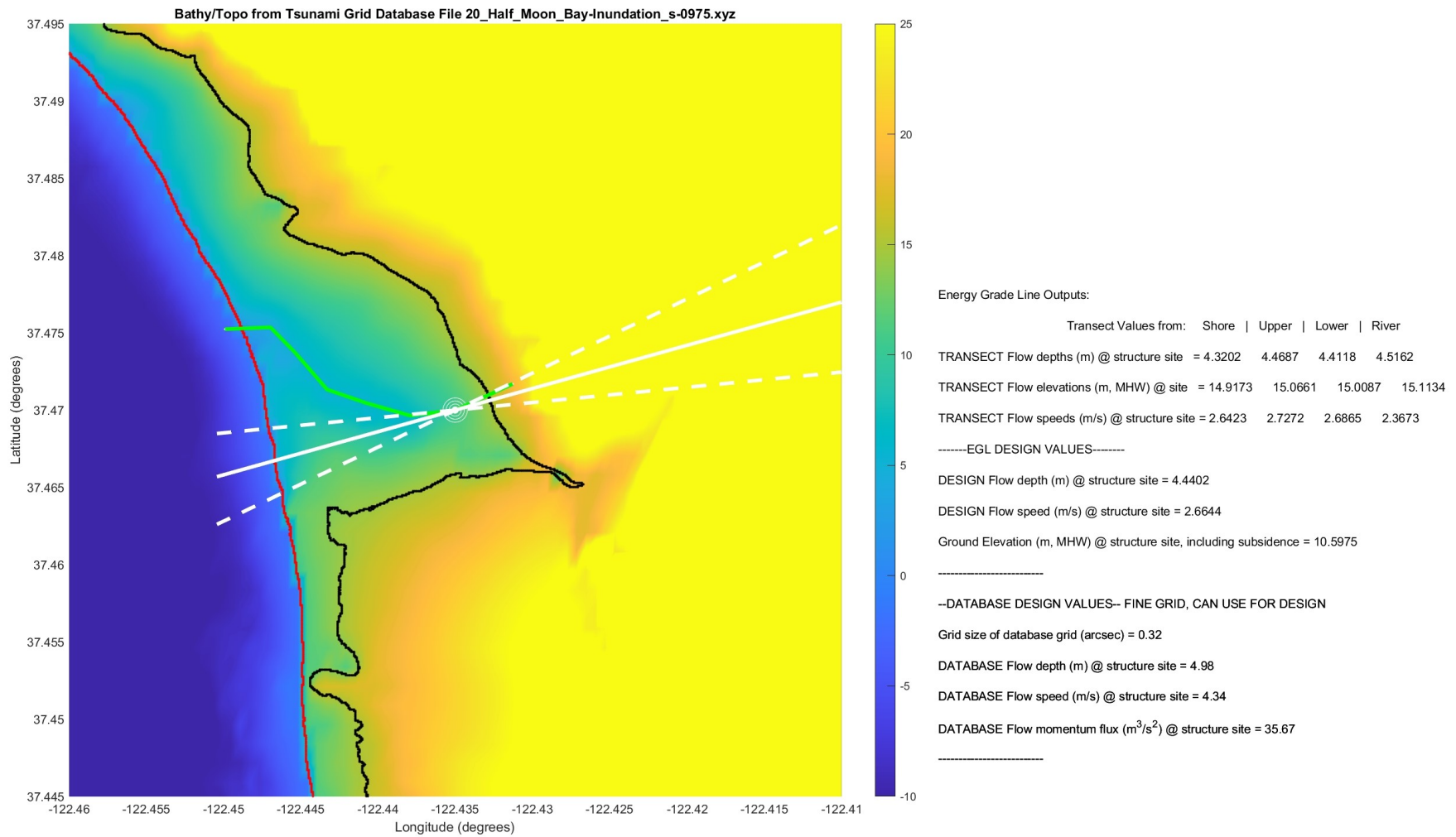


Figure 3.6: EGL transect analysis example for a location in California

3.12 SUMMARY OF SITE-SPECIFIC HAZARD METHODOLOGY

This study presents a methodology to provide site-specific tsunami hazard information in a format useful for prescriptive bridge loading calculations. The user shall use either a Level 1 or a Level 2 analysis, with the former being simpler and expectedly more conservative, and the latter representing the state-of-the-art approach. A Level 1 analysis is based on transect analysis, wherein the Energy Grade Line method is used to predict the evolution of tsunami flow depth and speed from the pre-tsunami shoreline to the inundation limit. The transect approach will naturally neglect any two-horizontal dimensional effects, and we recommend that four different transects be analyzed and inspected in order to predict the site specific tsunami hazard. The Level 1 approach initiates with accessing data from the tsunami inundation database developed by H. K Thio (AECOM), and extracting the relevant data nearest to the design site, or site of interest. A Matlab-based software program has been created to perform the transect analysis, and examples for the Pacific states are provided.

4.0 LITERATURE REVIEW: TSUNAMI LOADING ON BRIDGES

Although the 2004 Indian Ocean tsunami exposed the vulnerability of coastal infrastructure in Southeast Asian countries, the 2011 Japan tsunami reinforced the fact that countries with well-designed coastal infrastructure and lifelines are at significant risk for damage and total loss from tsunami inundation. Geologic conditions similar to those found off the east coast of Japan are also present off the west coast of the United States. The Cascadia subduction zone (CSZ) poses a direct threat for a major tsunami that could impact the coastlines of Oregon, Washington, and northern California. The CSZ last triggered an earthquake and subsequent tsunami about 400 years ago and has a high probability of unleashing a similar event in the next 100 years. Alaska and Hawaii have endured more recent tsunami events and remain at risk for future events.

In addition to the adaptation of design codes for mitigating the effects of tsunami loads on the built environment, numerical simulation of tsunami loading is also evolving within the structural engineering community in order to address the challenges of the estimating the effects imparted on structures due to hydrodynamic loading. The design, protection, mitigation, and simulation of structures subjected to hydrodynamic loading has thus been thrust to the forefront of structural engineering research. In parallel to the attention paid to tsunami loads, hydrodynamic loads brought on by wind storms has taken on paramount importance after the 2012 Superstorm Sandy. Many of the simulation methods used to predict wind-induced wave loads on structures are similar to those used for tsunami-induced loads.

This chapter reviews the current state of the art on numerical simulation methods and available validating experimental data for tsunami-induced hydrodynamic loading. Particular attention is paid to bridge structures; however, review is also made for buildings and for experiments focusing on wind-induced hydrodynamic loads as these data sets offer additional opportunities for validation of numerical models. Recent experiments with data available for validation of numerical simulation models are summarized in Table 4.1.

4.1 EXPERIMENTAL DATA

An experimental setup for a large-scale bridge superstructure model subjected to waves was developed by Bradner et al (2011). The model was a 1:5 scale reinforced concrete bridge superstructure. The bridge model is subjected to a wide range of wave conditions at multiple water levels. The experiments measured pressures, forces, and dynamic response of the bridge model using strain gauge, displacement sensors, and accelerometers.

The experiments were conducted in the large wave flume at OSU. The test specimen is based on prototype dimensions of the I-10 Bridge over Escambia Bay in Florida. The experiment had three phases. Phase 1 models a rigid structure where the specimen was bolted to the bent caps and each bent cap was then connected to an end anchorage block via a load cell. Phase 2 simulated a flexible

substructure using soft springs. Phase 3 was designed to simulate the response of the bridge span upon failure of the bent cap connections. The sensor suite was designed to measure wave conditions, forces and pressures acting on the specimen. Data were collected with a sampling rate of 250 Hz.

The analysis data shows a close second-order relationship between force and wave height for both regular and random waves. Large amplitude spike has little effect on horizontal and vertical reaction forces. The dynamic setup consisting of low—friction linear guide bearings on rails combined with different springs to account for different substructure flexibilities worked as intended to represent overall elastic structural dynamic properties and allows characterization of dynamic structure-fluid interaction.

Performance of highway bridge girder anchorages under simulated hurricane wave induced loads was conducted by Lehrman et al (2012). The research examines the performance three commonly used connection details for AASHTO Type III prestressed concrete girders: headed studs (HS), through bolts (TB), and clip bolts (CB). The load effects considered included vertical uplift force, lateral force, combined lateral and vertical forces, and dynamically applied wave force time histories.

All of the connections were used to anchor common AASHTO Type III bridge girders to the pile cap beam. The girders use prestressing and mild steel reinforcing and were detailed according to Escambia Bay Bridge. A survey of state transportation agencies was conducted to determine the most commonly used anchorages in coastal bridge infrastructure. The most common anchorages found to be headed studs, through bolts, and clip bolts.

The research found that the headed stud anchorage exhibited the most robust performance of the three considered anchorages. Failure of the HS anchorage was controlled by the performance of the steel stud. The clip bolt anchorage did not prove sufficient strength to resist wave loads produced by a storm with the intensity of hurricane Katrina. The through-bolt has a greater resistance for loads than the CB anchorage. The CB and TB anchorages exhibited concrete cracking and strand slip prior to failure.

Experiments were conducted at OSU by Istrati et al (2016) to investigate bridge deck to substructure connection forces during tsunami inundation. Models designed to 1:5 scale were tested in a 2D wave flume for both broken and unbroken waves on I-girder bridges with cross frames, solid diaphragms, and soffit slab. In addition to total horizontal and vertical forces imparted on the bridge models, the experiments also sought the distribution of these forces to the connections and the substructure as well as the influence of flexibility of the connections (bearings and shear keys) and substructure (columns and pier walls) on the distribution of forces. Venting to reduce uplift forces magnified by trapped air and forces in bridge decks skewed 45° relative to the flow direction were also investigated. For these experiments, it was found that the total horizontal and vertical forces exceed the weight of the bridge, and their maximum values occur nearly simultaneously (about 0.5 sec apart) with the maximum horizontal force occurring at initial impact and the maximum vertical force when the wave passes the middle of the bridge deck. Four phases were identified in the time histories of vertical force. In phase 1 (first impact) with uplift forces on the seaward side of the bridge, there is a rotational mode that coincides with the maximum vertical

connection forces. Maximum tension in the landward bearings occurs in Phase 3. The seaward girder and overhang experienced pressures (forces) several times larger than those of the internal girders. Flexible connections reduced the tension in the seaward bearings by about 50% (compared to “rigid” steel connections) in one case while substructure flexibility reduced the total horizontal force in most cases, up to about 50% compared to the “rigid” substructure case. Additional publications are forthcoming from this set of experiments.

In the second part of a companion set of papers, Hayatdavoodi et al (2014) describe experimental results and computational simulation for solitary wave loads on deck-girder bridges. The experiments were conducted on 1:35 scale bridge models for a wide range of water depths, wave amplitudes, submergence depths, and elevations. In the first paper of the companion set (Seiffert et al., 2014), the authors investigated a flat plate (slab) bridge deck for many of the same cases to determine if the forces on a flat plate could be used to predict the forces on a deck-girder bridge. In addition, the authors investigate the effect of trapped air on wave forces of the deck-girder bridge models in the second paper.

The experiments showed trends in the peak values of horizontal and vertical forces imparted by solitary waves on submerged and elevated bridge decks. Compared to the flat plate model, the presence of girders has a minor effect on forces in submerged cases. As a result, for submerged bridge decks only, the relationship between solitary wave load and wave amplitude, submergence depth, and number of girders can be generalized to prototype scale using Froude’s law in order to estimate design forces.

This scaling law does not apply for elevated bridge decks where air entrapment and vorticity have a significant influence on the deck forces. Although not shown in the paper, the authors mention that comparisons of the loads imparted on fully elevated models show that the number of girders has a significant effect on the forces. The effect was found to be random owing to the wave breaking process of the girders. Entrapped air was found to increase the vertical uplift force compared to models with air relief openings in the deck, but not to have a significant influence on horizontal forces. The effect was found to not only be hydrostatic, but also dynamic in that the entrapped air modifies the wave and the wave-induced forces.

Wave flume experiments were conducted by Hoshikuma et al (2013) at PWRI in Japan on 1:20 scale models of various bridge deck configurations. The tests were designed for a prototype bridge with 2 m (6.5 ft) clearance attacked by a tsunami with wave height reaching the top of the bridge deck. Cases of full inundation were not investigated in this suite of tests. Tests were performed for six bridge superstructure models: two slab and four deck-girder. Among the four deck-girder models, variations in deck overhang, number of girders, and girder spacing were considered.

Horizontal and vertical reaction forces were measured at the bearing supports. Horizontal reactions were due to impact of the tsunami wave while the vertical reactions consisted of buoyant force, vertical hydrodynamic forces, and rotation of the superstructure from the overturning effect of the horizontal wave loading. Trapped air was observed in the experiments of the deck-girder bridges, which tended to increase the uplift force. Uplift forces on the seaward side of the bridge were larger for models with longer deck overhang, leading to more significant overturning effects. For

models with two girders, closer spacing of the girders was found to lead to larger uplift forces compared to models with more spacing.

Additional PWRI experiments were conducted to examine protective strategies for the mitigation of tsunami-induced forces on bridge superstructures (Nakao et al., 2013). The first mitigation strategy was the attachment of fairings on the seaward side of the bridge in order to deflect wave energy. Semicircular and triangular fairings were considered. The second protective approach was the placement of frontage road bridges on the seaward side of the main bridge. Slab and deck-girder (two girders) frontage road bridges were considered. Experimental results showed that the presence of fairings reduced the horizontal and vertical forces at the bearing support. In addition, frontage road bridges also reduced the bearing forces, but only if the frontage bridge survived the initial tsunami attack.

Table 4.1: Summary of Experiments for Validation of Numerical Simulation Models.

Organization	Year	Structure	Scale	Hazard	Data	Reference
PWRI	2012	Bridge Deck	1:20	Tsunami	Yes	J. Hoshikuma
Hawaii	2014	Bridge Deck	1:35	Tsunami	TBD	M. Hayatdavoodi
UNR/OSU	2016	Bridge Deck	1:5	Tsunami	June 2016	I. Buckle, S. Yim
UW	2017	Bridge Deck	TBD	Tsunami	TBD	M. Motley
UW	2004	Bridge Column		Tsunami	Yes	H. Yeh
OSU	2016	Building	1:1 (dynamic)	Tsunami	TBD	D. Borello
OSU	2011	Bridge Deck	1:5	Storm Surge	Yes	D. Cox, C. Higgins

4.2 NUMERICAL SIMULATION SOFTWARE

The simulation of bridge response to tsunami loading will play a critical role in the development and validation of loading calculations. Various software can be used to simulate fluid-structure interaction with varying formulations of both the fluid and structural response, as well as the effects of trapped air.

CFD analysis of bridge deck failure due to tsunami loading was conducted by Bricker et al (2012). Analyses were performed with Reynolds-averaged Navier-Stokes (RANS) models through the Open-FOAM fluid dynamics computational program. The effects of lift, drag, and moment on a typical bridge deck were examined. The analysis considers two types of tsunami behaviors. In shallow offshores, tsunami approaches shore as a surge or bore. In deeper off shore, tsunami appears as a smoothly rising water surface.

Two dimensional model of a bridge deck was generated using OpenFOAM to simulate tsunami interaction for the Utatsu highway bridge in Minamisanriku, Japan. The bridge was a concrete girder bridge about 8 m above water level with an incline of 3 degrees upward on the seaward. The full domain spans 110 m horizontally and 20 m vertically for the rising free surface simulations and 30 vertically for surge and steady flow simulations. The bridge had an incline of 3 degrees upward on the seaward side. The bridge deck width is 7.9 m and thickness is 0.5m.

Based on the OpenFOAM simulations, deck failure resulted from lift force and overturning moment. The results show that a surge tsunami wave can cause the bridge to fail. A sub-critical, smoothly rising water surface would not cause a bridge the size of the Utatsu Bridge deck to fail because accelerated flow under the bridge deck causes a negative lift. When the deck becomes submerged with flow, vortex shedding and free-surface fluctuation can cause the deck to overturn.

A systematic integration of numerical models for tsunami generation, propagation, and inundation at specific bridge sites was developed by Azadbakht and Yim (2016). Horizontal and vertical loads and overturning moment were computed based on tsunami propagation and runup following a hypothetical CSZ event for four deck-girder bridges (Schooner Creek Bridge, Drift Creek Bridge, Siletz River Bridge, and Millport Slough Bridge) along the Oregon coast in the Siletz Bay area.

Using site specific flow height and velocity from the numerical simulation of tsunami generation and propagation, bridge forces were computed using the LS-DYNA finite element analysis code. Simulations of bridge response were performed (as separate analyses) for two stages of tsunami loading: 1) initial impact and overtopping and 2) full inundation. It is noted that none of the six CSZ scenarios postulated by the authors resulted in tsunami flow reach the Siletz River Bridge. Based on the numerical simulations, the authors found that the maximum horizontal and downward vertical forces occur approximately simultaneously and that the magnitudes of these forces were significantly affected by the water free-surface elevation on the seaward side of the bridge. In addition, bridge decks with a downward seaward slope did not experience significant uplift forces at initial tsunami impact. Trapped air was shown to be responsible for more than half of the total uplift force in the numerical simulations.

Comparisons of the deck-girder Schooner Creek Bridge with an analogous box-girder configuration revealed that the maximum horizontal loads were slightly larger, the downward vertical forces were smaller, and the uplift forces were significantly larger for the box-girder case. The authors recommended minimum criteria for bridges to be designed for the buoyancy force as the minimum tsunami uplift force and that design of connections to the substructure also account for the simultaneous occurrence of the uplift force with the maximum horizontal force. Equations to estimate the maximum horizontal force, maximum downward vertical force, and maximum uplift force were developed. The equations were not compared with experimental data.

In addition to the numerical simulation of tsunami loads on Oregon coastal bridges, Azadbakht and Yim (2015) performed similar numerical simulations for five California coastal bridges. Tsunami flow conditions were provided by Caltrans for the Mad River Slough Bridge (precast I-girder), Salmon Creek Bridge (concrete slab), Old Creek Bridge (T-girder), Malibu Lagoon Bridge (cast-in-place box-girder), and Agua Hedionda Lagoon Bridge (concrete slab). The flow fields were based on various return periods considering earthquake sources (Thio et al., 2010).

Simulations for initial impact and full inundation were performed as separate analyses using LS-DYNA. The causes of downward vertical force and the conditions for net uplift force were examined for the five bridges. Downward vertical force during overtopping was found to be a combination of hydrostatic load due to the weight of the overtopping water and various hydrodynamic effects. Entrapped air was found to amplify the uplift force after initial impact and partial inundation prior to full inundation. For fully inundated bridges, the uplift force was dominated by buoyancy.

For the precast I-girder Mad River Slough Bridge, the effect of failure of the first seaward girder was examined via numerical simulation where the girder was removed from the finite element model. For this particular case, the girder removal led to a small reduction (15%) in the maximum horizontal force and increase (25%) in the maximum uplift force compared to the undamaged bridge superstructure for the same tsunami flow conditions. Equations for the estimation of tsunami loads (maximum horizontal, maximum downward vertical, and maximum uplift) were proposed; however, the equations were not compared with experimental data in this work.

Parallel to the wave flume experiments conducted by Istrati et al (2016), Xiang (2016) performed detailed numerical simulations using LS-DYNA with the experimental data. Analysis of the experimental data revealed two types of fluid forces that are important for developing tsunami design guidelines: 1) a high frequency, impulsive slamming force and 2) a lower frequency quasi-static force. The elevation of the deck above the initial, or standing, water level was found to have a significant influence on the wave forces and a “deck clearance” parameter was defined.

After reviewing other empirical tsunami load estimation equations, Xiang (2016) proposed a new empirical approach that accounted for the slamming and quasi-static fluid forces, as well as the “deck clearance” effect. The proposed approach was an extension of the load estimation equations developed by Azadbakht and Yim (2015). Although the proposed load estimation procedure was validated with the experimental data from Istrati et al (2016), the procedure has not yet been validated against other experimental data sets.

5.0 RECOMMENDATIONS FOR LOADING CALCULATIONS

The loads acting on a bridge during tsunami inundation depend on several factors, each with significant uncertainty. In addition to flow depth and speed based on probabilistic tsunami hazard analysis (PTHA), the following factors contribute to the tsunami-induced loads on bridges:

- Bridge deck orientation in three dimensions
- Debris in the tsunami flow

The basic approach to estimating tsunami loading is to compute reference horizontal, uplift, and downward forces based on two-dimensional equations developed by Azadbakht and Yim (2015, 2016). The flow depth and speed used in these equations will be based on site-specific PTHA. Then, simulation-based factors based will account for three-dimensional effects of skew and super elevation. Allowances for debris are also included.

5.1 NOMENCLATURE FOR LOAD EQUATIONS

The following symbols, shown in Figure 5.1, describe each load estimation equation:

ρ – density of water (1000 kg/m³)

g – gravitational constant (9.81 m/s²)

h – height from tank floor to standing water level (m)

h_g – height from tank floor to bottom of bridge girder (m)

h_o – flow height relative to bottom of bridge girder (m)

d_g – girder depth (m)

b_g – girder width (m)

N – number of girders

d_d – deck depth or thickness (m)

b_d – deck width (m)

L_b – out-of-plane bridge width (m)

H – total flow depth, measured from tank floor (m)

η – flow depth relative to standing water level (m)

u – horizontal flow speed (m/s)

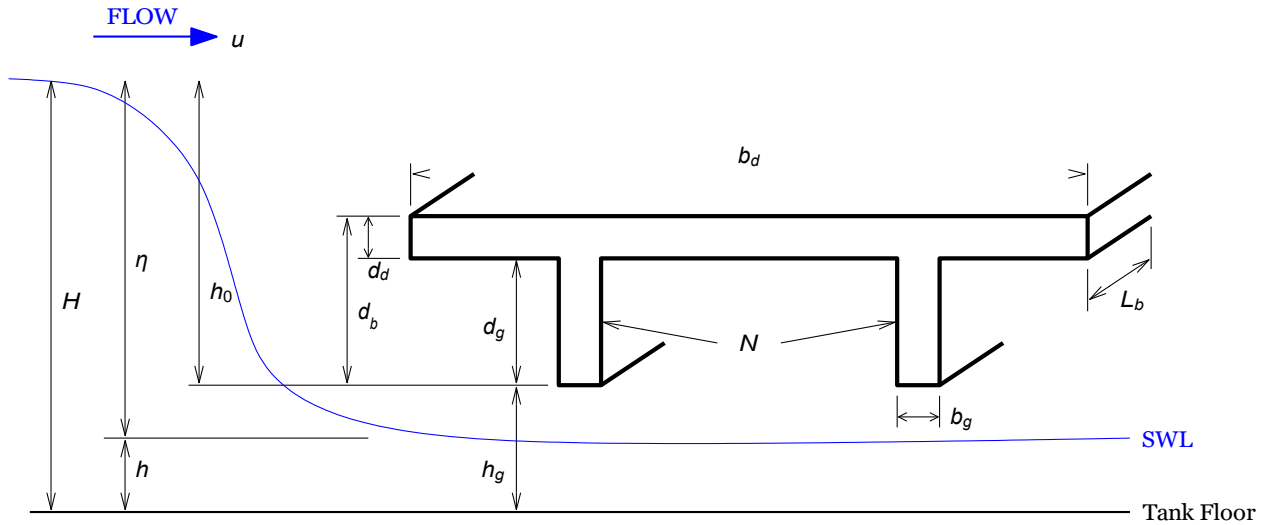


Figure 5.1: Variables that describe load estimation equations for deck-girder bridges.

5.2 LOAD CASES

The loading equations are based on a bore with flow depth, η , and flow speed, u , approaching the bridge superstructure. Other scenarios are possible for a given flow depth and speed; however, the TAC determined a bore to be the controlling case.

The maximum values for flow depth and flow speed, η_{max} and u_{max} , respectively, determined from site-specific PTHA are not likely to occur simultaneously. In addition, loads created by large water-borne debris are not likely to coincide with either η_{max} or u_{max} . Accordingly, three load cases are presented.

5.2.1 Load Case 1

The first load case assumes maximum flow speed, u_{max} , from PTHA with coincident flow depth equal to $(2/3) \eta_{max}$. The factor of $2/3$ is based on simulations where it is observed that the relationship between the maxima of flow depth and flow speed and the maximum value of momentum flux satisfies:

$$\frac{\eta_{max} u_{max}^2}{(\eta u^2)_{max}} > 1.5$$

(5-1)

The lower bound of 1.5 is somewhat conservative and is closer to 3.0. Using this relationship, the upper bound for flow depth at the occurrence of maximum flow speed is then

$$\frac{\eta_{max}}{\eta} > 1.5 \text{ or } \eta < 0.67\eta_{max} \tag{5-2}$$

The values for u_{max} and η_{max} are determined from site-specific PTHA.

5.2.2 Load Case 2

Using a similar approach to the first load case, the upper bound for the flow speed at the occurrence of maximum flow depth is

$$\frac{u_{max}^2}{u^2} > 1.5 \text{ or } \frac{u_{max}}{u} > \sqrt{1.5} \text{ or } u < \sqrt{\frac{2}{3}} u_{max} \approx 0.8u_{max} \tag{5-3}$$

The second load case then corresponds to the flow depth of η_{max} with flow speed of $0.8u_{max}$ where u_{max} and η_{max} are determined from site-specific PTHA.

5.2.3 Load Case 3

The third load case includes large water-borne debris, whose load magnitude, F_{debris} , is computed separately from the loading equations presented herein. Recognizing that bore attack coincident with water-borne debris impact is unlikely, this load case assume flow speed $0.5u_{max}$ with flow depth $0.5\eta_{max}$ occurring with F_{debris} . The values for u_{max} and η_{max} are determined from site-specific PTHA.

5.3 SUMMARY OF LOAD CASES

The flow speed and flow depth for each load case are summarized in Table 5.1. Load case 1 corresponds to maximum flow speed, load case 2 corresponds to maximum flow depth, and load case 3 accounts for large water-borne debris.

Table 5.1: Summary of Three Load Cases for Bore Attack on a Bridge Superstructure using Maximum Flow Speed and Flow Depth Determined from Site-specified PTHA.

Load Case	Flow Speed	Flow Depth	Large Debris
1	u_{max}	$0.67\eta_{max}$	
2	$0.8u_{max}$	η_{max}	
3	$0.5u_{max}$	$0.5\eta_{max}$	F_{debris}

The effect of small debris, or debris-laden sea water, will be taken in to account in the individual load equations for horizontal, uplift, and downward force described in the following sections.

5.4 HORIZONTAL LOAD ESTIMATE

Flow speed, u , and flow depth, η , are based on PTHA. If the flow depth is below the bridge superstructure, the horizontal load estimate is zero, but proceed to substructure loading analysis. For flow depth that will reach the superstructure:

1. Compute the steady state horizontal force per unit bridge length

If the flow height, h_o , relative to the bottom of the bridge superstructure, $h_o = \eta - h_g$, is less than the height of the superstructure ($h_o < d_b$), then the wave is in partial contact with the superstructure and

$$F_{H0} = C_1 \left(\frac{1}{2} \rho g h_o^2 \right) + C_2 \left(\frac{1}{2} \rho h_o u^2 \right) \quad (h_o < d_b) \quad (5-4)$$

Where:

$\rho=1040 \text{ kg/m}^3$ (includes sediments), $g=9.81 \text{ m/s}^2$, and $C_d=2$ in the absence of a bridge specific drag coefficient. When the flow height exceeds the height of the superstructure, i.e., when $h_o > d_b$, then

$$F_{H0} = C_1 \left(\frac{1}{2} \rho g (2h_o - d_b) d_b \right) + C_2 \left(\frac{1}{2} \rho d_b u^2 \right) \quad (h_o > d_b) \quad (5-5)$$

The factors C_1 and C_2 in both equations depend on the bridge type and are based on correlation of the nominal load equations with simulations. The factors also differ for horizontal impact and steady state loads. Recommended values for the coefficients C_1 and C_2 are shown in Table 5.2.

Table 5.2: Coefficients for Steady State Horizontal Load Equation

	Box Beam	Open Girder
C_1	0.77	0.73
C_2	0.46	0.40

2. Use multipliers to account for impact loading as well as three-dimensional bridge orientation (skew and superelevation) and small debris, and add additional force for large debris impact (for load case 3 only)

$$F_H = C_{skew} C_{super} C_{debris} C_{impact} F_{H0} + F_{debris} \quad (5-6)$$

The factors C_{skew} and C_{super} are given in Figure 5.6 and Figure 5.8, respectively, while the debris-laden water factor, C_{debris} , should be taken as 1.06 and is applied only to the horizontal load estimates. The water-borne debris force, F_{debris} , is described in Section 5.8. Note that the 4% increase in fluid density ($\rho=1040 \text{ kg/m}^3$) and the use of $C_{debris}=1.06$ satisfy the ASCE 7-10 recommendation for a 10% increase in fluid density to account for small debris.

The impact loading factor, C_{debris} , depends on the bridge type and is based on comparison of peak horizontal loads to peak impact loads from numerical simulations of box beam and open girder bridges. Recommended values for the horizontal impact load factor are shown in Table 5.3. Note that steady state horizontal force accounting for skew, super elevation, and debris can be computed using Eq. (5-6) with $C_{debris} = 1$ and $F_{debris} = 0$.

Table 5.3: Coefficients for Horizontal Impact Load.

	Box Beam	Open Girder
C_{impact}	2.5	2.1

5.5 UPWARD LOAD ESTIMATE

Flow speed, u , and flow depth, η , are based on PTHA. If the flow depth is below the bridge superstructure, the upward (vertical impact) load estimate is zero, but proceed to substructure loading analysis.

1. Compute the upward load per unit bridge length

$$F_{U0} = C_3(\rho gV) + C_4(\rho b_d u^2 L_b) \tag{5-7}$$

Where:

$\rho=1040 \text{ kg/m}^3$ (includes sediments), $g=9.81 \text{ m/s}^2$, V is the volume of a unit length slice of the superstructure, b_d is the width of the superstructure, and L_b is the bridge length.

The factors C_3 and C_4 in the upward load equation depend on the bridge type and are based on correlation of the nominal load equations with simulations. Recommended values for C_3 are shown in Table 5.4.

Table 5.4: Coefficient C_1 for upward load equation.

	Box Beam	Open Girder
C_1	1.0	0.7

The factor C_4 in Eq. (5-8) accounts for clearance of the bridge above the standing water level,

$$C_4 = C_5 \left(\frac{h_0}{h_g - h} \right)^{C_6} \quad (5-8)$$

Where:

h_0 is the flow depth relative to the bottom of the bridge deck and h_g is the height from the tank floor to the bottom of the bridge deck. The constants C_5 and C_6 depend on the bridge type as shown in Table 5.5.

Table 5.5: Coefficients for C_4 Clearance Factor in Upward Load Equation

	Box Beam	Open Girder
C_5	0.5	0.65
C_6	0.4	0.5

2. Use multipliers to account for three-dimensional bridge orientation (skew and superelevation) and small debris

$$F_U = C_{skew} C_{super} F_{U_0} \quad (5-9)$$

The factors C_{skew} and C_{super} are given in Figure 5.6 and Figure 5.8, respectively. If vertical impact forces from water-borne debris are to be included, additional calculations should be performed.

5.6 DOWNWARD LOAD ESTIMATE

Flow speed, u , and flow depth, η , are based on PTHA. If the factored flow depth is below the bridge superstructure, the downward load estimate is zero, but proceed to substructure loading analysis.

1. Compute the downward force per unit bridge length

$$F_{Do} = \rho g (h_o - d_b) b_d \quad (5-10)$$

Where:

$\rho=1040 \text{ kg/m}^3$ (includes sediments), $g=9.81 \text{ m/s}^2$, and d_b and b_d are the height and width, respectively, of the superstructure.

2. Use multipliers to account for three-dimensional bridge orientation (skew and superelevation) and small debris, and add additional force for large debris impact

$$F_D = C_{skew}C_{super}F_{Do} \quad (5-11)$$

The factors C_{skew} and C_{super} are given in Figure 5.6 and Figure 5.8, respectively. If impact forces from water-borne debris are to be included, additional calculations should be performed.

5.7 BRIDGE DECK ORIENTATION

Three angles describe the orientation of a bridge deck: superelevation, skew, and slope, as shown in Figure 5.2. Motley et al (2016) performed three-dimensional simulations using OpenFOAM to assess the effect of orientation on the total horizontal and vertical forces imparted on the superstructure. Additional analyses to support these results have been performed or are in progress.

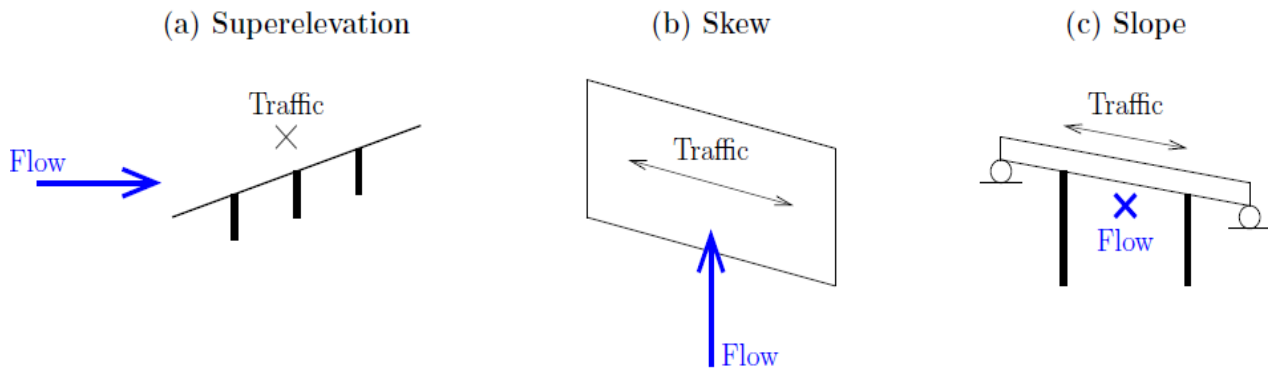


Figure 5.2: Three descriptors of bridge deck orientation: (a) superelevation, (b) skew, and (c) slope.

5.7.1 Skew

Plan view of a skewed bridge deck is shown in Figure 5.3.

Where:

θ measures the skew angle between the piers (or abutments) and the girders.

The direction of tsunami flow is parallel to the piers/abutments. Four corners of the bridge deck are identified based on front vs. back relative to flow and acute and obtuse skew angle.

Based on the OpenFOAM analyses, it was found that the skew angle did not significantly affect the total horizontal impact force; however, there are localized effects due to the wave impacting the FA-BO side of the bridge deck before the FO-BA side. As the skew angle increases, the local reaction forces increase for the FA and BO locations but decrease for the FO and BA locations, as shown in Figure 5.4. In addition, there will be a component of force acting along the girders of a skewed bridge.

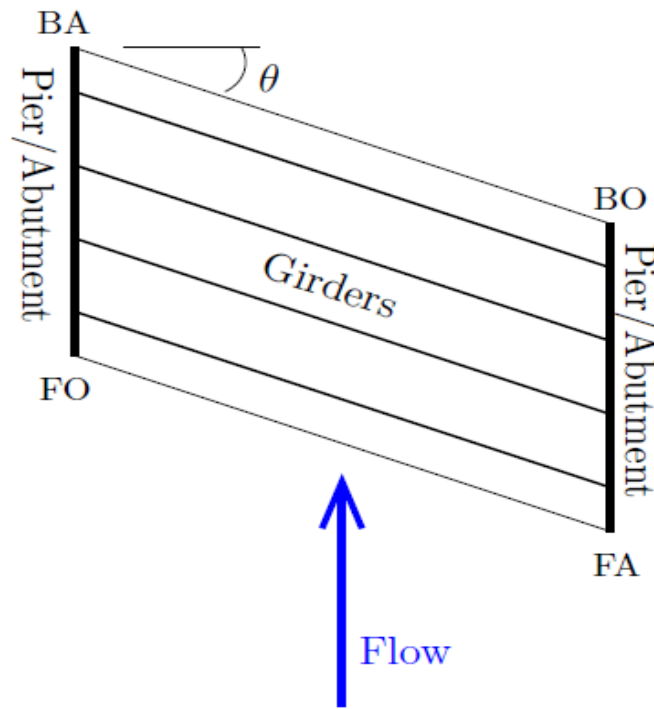


Figure 5.3: Plan view of skewed bridge analyzed by Motley et al (2016)]. Corners of the superstructure are identified: front acute (FA); front obtuse (FO); back acute (BA); and back obtuse (BO).

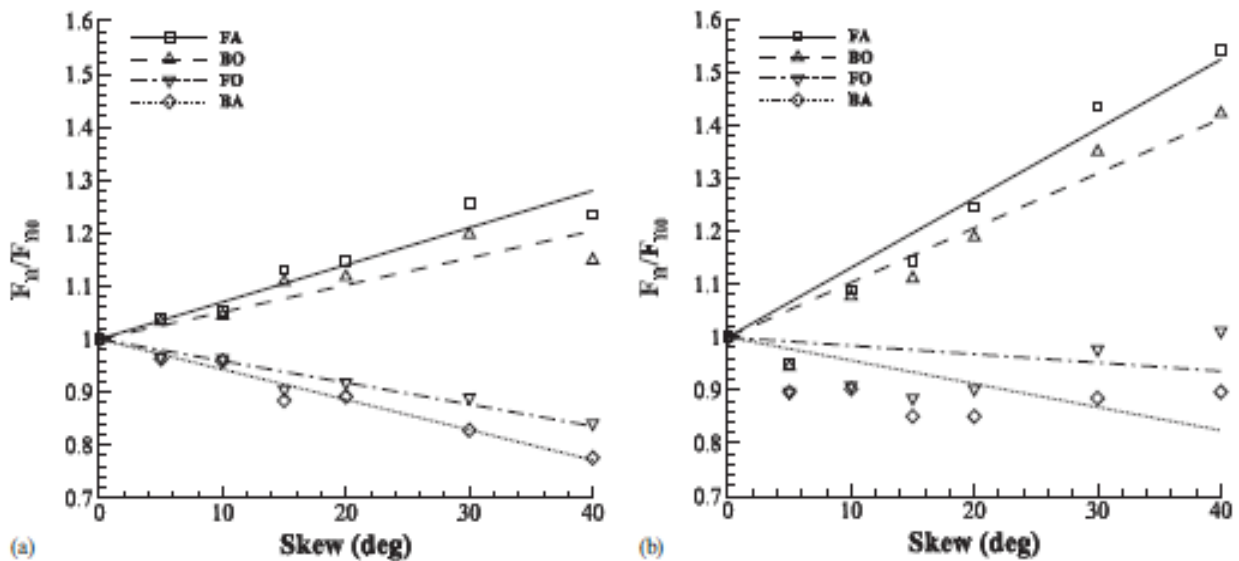


Figure 5.4: Effect of skew angle on horizontal tsunami forces: (a) impact and (b) steady state. (Image from Motley et al (2016)).

For vertical forces (uplift impact and downward steady state), skew angle was found to have little effect on uplift forces, both total and localized, even for large skew angles as shown in Figure 5.5(a). In addition, Figure 5.5(b) shows that the magnitude of downward steady state force tends to decrease as the skew angle increases.

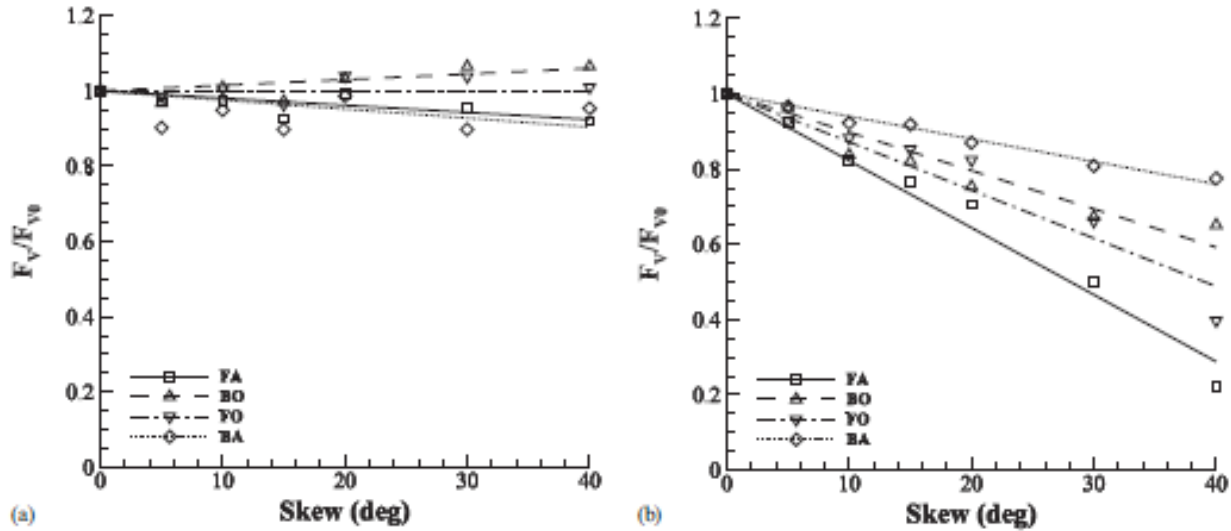


Figure 5.5: Effect of skew angle on vertical tsunami forces: (a) uplift impact and (b) downward steady state. (Image from Motley et al (2016)).

The effect of skew angle on the total, or resultant, horizontal and vertical forces are summarized in Figure 5.6 via the modification factor, C_{skew} . These trends are found by summing the trends shown in Figure 5.4 and Figure 5.5. It may be advantageous for a bridge engineer to first determine the total forces acting on the superstructure using Figure 5.6, then use Figure 5.4 and Figure 5.5 to determine the localized forces that must be resisted at the connections on the front and back faces of the bridge deck. Additional simulations and comparisons with experimental data for skewed bridges are underway at UNR (Istrati and Buckle).

5.7.2 Superelevation

Additional OpenFOAM analyses were performed in order to assess the effect of superelevation (Xiang, 2016). As shown in Figure 5.7, cases of the road surface turned away (negative superelevation) and turned toward (positive superelevation) tsunami flow are examined in the range of -10° to $+10^\circ$. Due to the two-dimensional nature of tsunami flow relative to superelevation, additional OpenSees PFEM simulations were conducted in order to corroborate the OpenFOAM analyses.

Due to the increase in surface area exposed to tsunami flow, positive and negative superelevation had similar effects on the total horizontal force as shown in Figure 5.8(a). With the road surface turned away from tsunami flow (negative superelevation), there is a significant increase in the uplift force shown in Figure 5.8(b). This result matches intuition that bridge superstructures with negative superelevation are prone to unseating during a tsunami. On the other hand, there is little effect on uplift force for positive superelevation. As shown in Figure 5.8(c), positive superelevation

leads to an increase in the downward force, which can be beneficial in preventing unseating. For negative superelevation, the downward force decreases significantly, approaching uplift, because the road surface is turned away from the flow.

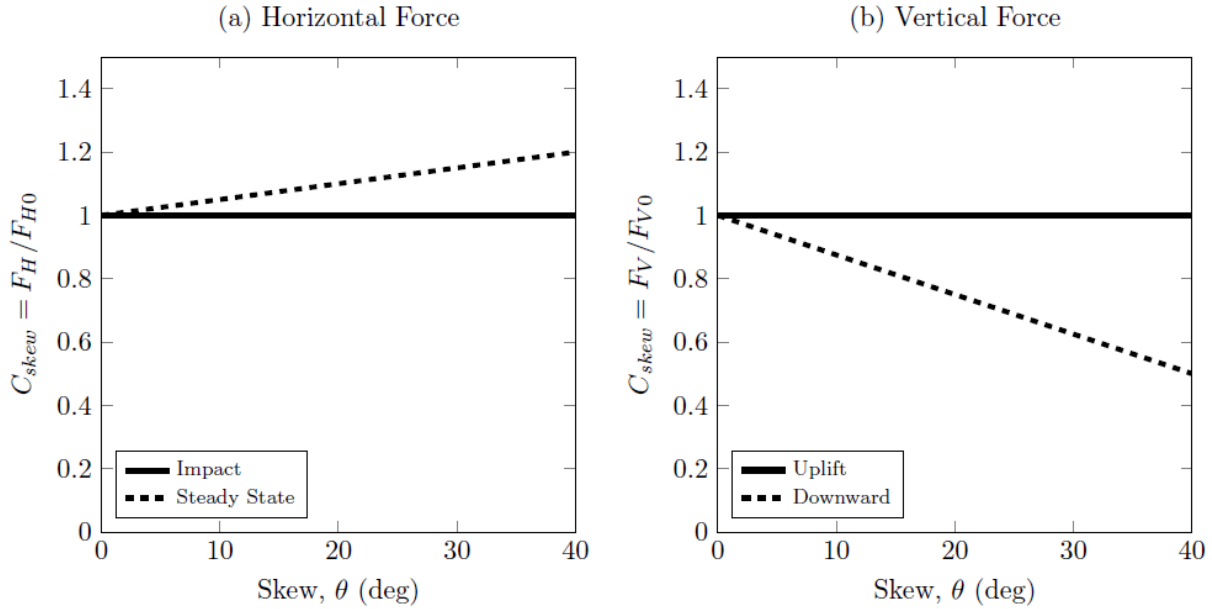


Figure 5.6: Modification of total bridge force, compared to the non-skew case, based on skew angle: (a) horizontal force, (b) vertical force.

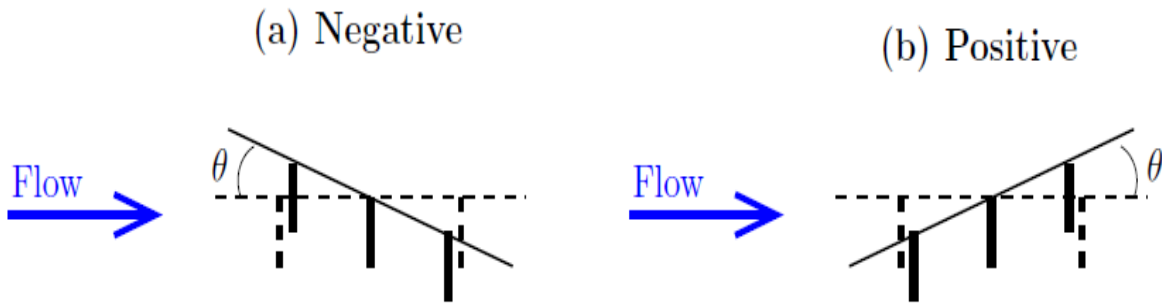


Figure 5.7: Super elevation angle relative to tsunami flow: (a) negative; (b) positive.

5.7.3 Slope

Further three-dimensional OpenFOAM analyses performed by Motley’s research group showed no significant effect of sloped bridge decks on the total horizontal and vertical forces. This result is based on the conservative assumption that the tsunami flow depth is sufficient to reach the high end of the deck. Analyses were performed for slopes of up to $\pm 8\%$ grade. Slope does however introduce rolling, pitching, and spinning moments due to the waves not impacting the bridge uniformly.

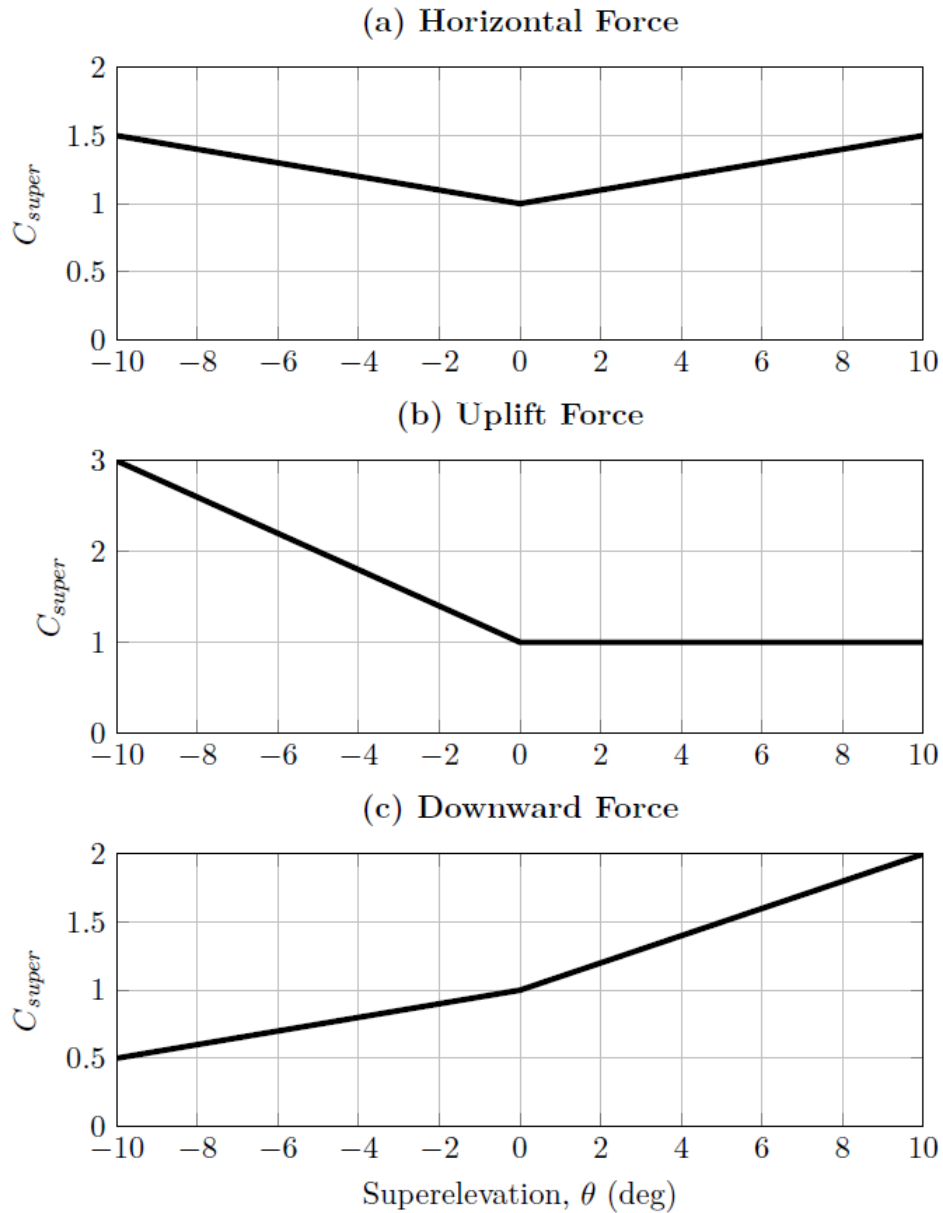


Figure 5.8: Multiplier of total bridge force based on superelevation: (a) horizontal force, (b) uplift force, and (c) downward force.

5.8 DEBRIS

Compared to debris-laden seawater, water-borne debris, e.g., vehicles and shipping containers, can impart much larger horizontal impact forces to coastal bridges. Several methods have been proposed to estimate the impact force of water-borne debris. For the bridge design equations discussed here, these impact forces are considered separately from the reference horizontal load, F_{H_0} .

The impulse-momentum method described ASCE 7-10 computes the debris impact force as

$$F_{debris} = \frac{\pi mu}{2\Delta t} \quad (5-12)$$

Where:

m is the mass of the debris, u is the velocity of the debris, and Δt is the debris impact duration. Haehnel and Daly proposed a debris impact force equation based on the work-energy method

$$F_{debris} = \frac{mu^2}{S} \quad (5-13)$$

Where:

S is the stopping distance of the debris.

Since it is difficult to obtain the impact duration time and stopping distance, FEMA (2012) proposed an alternative approach based on flexible impact

$$F_{debris} = 1.3u\sqrt{km(1+c)} \quad (5-14)$$

Where:

1.3 is the importance factor for critical infrastructure such as bridges and c is the added mass coefficient.

Naito et al (2014) applied Eq. (5-14) to various debris flowing at $u=4$ m/s with zero for the added mass coefficient and estimated that moderate sized debris such as a passenger vehicle or utility pole would lead to an impact force of about 130 kN (30 kip). An empty shipping container would impart a force of about 1800 kN (405 kip) at the 4 m/s speed while a full container would generate a force of approximately 6400 kN (1440 kip). These calculations are based on elastic impact; thus, the impact force should be capped by the crushing strength of the debris, e.g., 620 kN (140 kip) for a shipping container.

Although slamming of large debris can lead to significant downward forces, the effects of water-borne debris on vertical forces (uplift and downward) are not considered here. If these effects are important, additional analyses are required.

6.0 GEOTECHNICAL CONSIDERATIONS

This section identifies key geotechnical issues related to bridge performance during a design tsunami event consisting of multiple inundation and retreat sequences. Performance goals are discussed and design guidance provided.

6.1 DESIGN ISSUES

The primary geotechnical issues can be partitioned into those that directly affect the bridge's foundations and abutments, and those that affect approach embankments.

6.1.1 Foundations and abutments

A bridge's ability to withstand hydrodynamic forces and possible debris impacts is dependent upon being able to transfer those loads to its foundations. These loads are depicted in Figure 6.1 for the cases of deep and shallow foundations. The foundations must withstand these load demands for inundation cycles lasting as long as 20 minutes and in potentially extreme scour conditions.

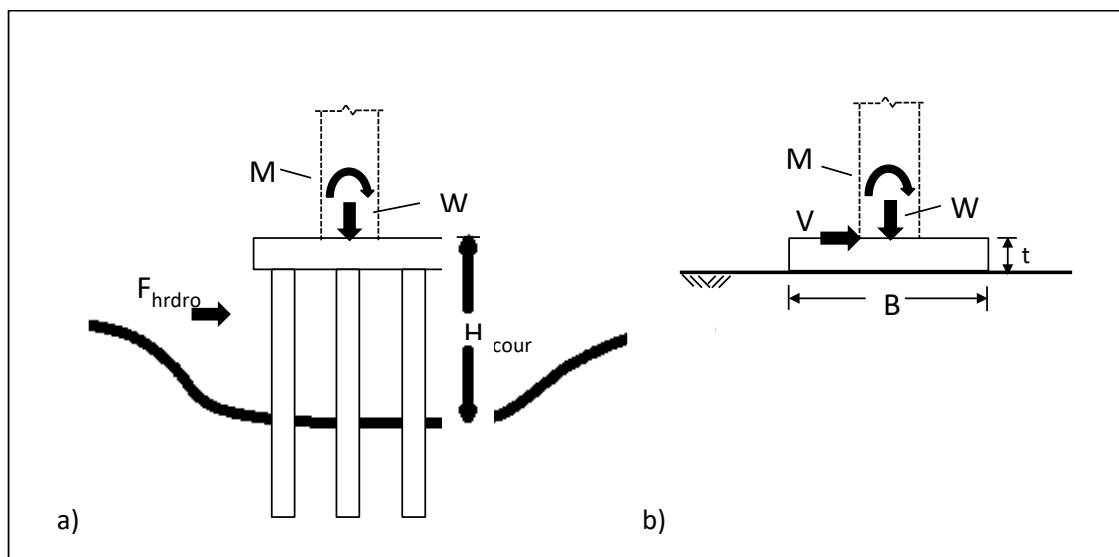


Figure 6.1: Tsunami induced foundation loading on a) deep foundations and b) shallow foundations.

6.1.2 Approach embankments

If performance goals include limited use of the bridge following the tsunami event, the approach embankments must:

- maintain stable slopes and functional geometry by resisting erosion

- maintain stable slopes during drawdown

6.2 PERFORMANCE GOALS

Required and optional bridge performance goals are discussed in Section XX. Table 6.1 and Table 6.2 translate those goals into foundation performance requirements for an unfactored load case.

Table 6.1: Foundation Design Requirements for Different Performance Goals

Performance Goal	Pile cap/shaft translation (in)	Pile cap rotation (rad)	Max ductility demand (piles/shaft)
Deep foundations (piles/shafts)			
No collapse or washout	12	0.02	2
Limited functionality	6	0.01	2
Shallow foundations			
No collapse or washout	0	0	-
Limited functionality	0	0	-

Table 6.2: Design Requirements for Approach Embankments.

Performance Goal	Moderate erosion	Slope stability under drawdown
Approach embankments		
No bridge collapse or washout	No mitigation	No mitigation
Limited functionality	Mitigation per <i>Bridge Scour and Stream Instability Countermeasures: Experience, Selection, and Design Guidance-Third Edition</i> (Lagasse, et al, 2009)	FS>1.3 per Army Corp EM 1110-2-1902

For deep foundations, the allowable deformations were selected based on a desire to avoid excessive superstructure deformation while not imposing overly restrictive, uneconomical requirements. Project specific criteria that differ from the recommended values are acceptable if based on analysis. The maximum ductility demand (μ_D) requirement reflects the difficulty of achieving elastic performance in piles and shafts under large lateral loading. A μ_D of 2 corresponds to moderate cracking of concrete and will not adversely affect the pile or shaft performance in the short term.

For shallow foundations, sliding or overturning could lead to catastrophic failure. Load and resistance factors for these design checks were selected to be consistent with an approximate

Factor of Safety of 2.5. If approach embankment survival is an objective, erosion mitigation will be needed. See *Bridge Scour and Stream Instability Countermeasures: Experience, Selection, and Design Guidance-Third Edition* (Lagasse, et al, 2009) for a discussion of options and design methods. To estimate slope stability under rapid drawdown see Army Corp EM 110-2-1902 for guidance. A chart-based solution is available in Moregenstern (1963).

6.3 FOUNDATION TYPE SELECTION

6.3.1 Deep foundation

For new bridges, deep foundations are preferred since they can be extended to depths well below potential scour depth. Large diameter piles or shafts have the benefit of large lateral stiffness and capacity even when surficial sediments are lost due to scour. Such foundations also tend to be smaller, for a given lateral capacity, and thus reduce scour and hydrodynamic loads relative to larger footings utilizing smaller pilings.

6.3.2 Shallow foundation

Spread footings should NOT be used when constructed on top of potentially erodible soils. Undermining, where some or all of the soil directly below the footing is eroded away, can lead to catastrophic footing failure.

Spread footings can be used when placed directly on rock not susceptible to erosion.

Due to potentially low sliding resistance, keying the footing into the rock or use of tie down anchors should be considered.

6.4 LOAD CASES

Generally, the structural load case that results in the largest lateral demand on the superstructure will develop peak foundation demands. The structural load case that results in maximum uplift forces should also be used to evaluate foundation loads. In both cases, maximum scour depths should be assumed.

6.5 EVALUATION OF FOUNDATION RESISTANCE

The external loading of deep and shallow foundations are depicted in Figure 6.1. These loads can be estimated following the procedures of Chapter 5 based on flow depths and velocity prescribed procedures in Chapter 3. In addition to the performance goals described in Section 6.2, geotechnical resistance must be evaluated to ensure basic limit-equilibrium requirements are satisfied with suitable reliability.

6.5.1 Deep foundations

Compressive, uplift, and moment demands on piles and shafts are calculated using p-y spring models for lateral soil resistance and t-z curves for vertical resistance. Guidance on p-y and t-z curve selection can be found in Hannigan et al. (2016). The analysis should assume all soil to a

depth below footing of H_{scour} is removed by scour. Compressive and uplift pile demands are compared to nominal compressive and uplift capacities according to:

$$\gamma Q < \phi R_N \tag{6-1}$$

Where:

γ = load factor for foundation loading in an extreme event and set = 1

Q = compression or uplift demand

ϕ = resistance factor for pile or shaft resistance

R_N = nominal compressive or uplift resistance of the pile or shaft

Note that the selection of the correct resistance factor is a complicated issue. ϕ is usually set = 1 for extreme event loading. This ignores the bias (usually positive) of each method.

6.5.2 Shallow foundations

Resistance to sliding is evaluated according to:

$$\gamma V < \phi W \tan \theta \tag{6-2}$$

Where:

γ = load factor for foundation loading in an extreme event and set = 1

V = shear demand

ϕ = resistance factor for sliding resistance and set to 0.4

W = normal force acting on the footing

θ = friction angle of the rock-footing interface (taken as 20 degrees)

Resistance to overturning is evaluated according to:

$$\gamma(M + Vt) < \phi WB/2 \tag{6-3}$$

Where:

γ = load factor for foundation loading in an extreme event and set = 1

M = moment demand

V = shear demand

t = footing thickness

ϕ = resistance factor for overturning and set to 0.4

W = normal force acting on the footing

B = footing width

Pile group and shaft analysis should follow the recommendations of AASHTO LRFD Bridge Design Specifications 8th Edition, Section 10.7.2.4 – Horizontal Foundation Movement.

In calculating the geotechnical resistance of soils, a saturated condition should be assumed. Effective stresses should be calculated using buoyant unit weights for soil. Due to the low permeability of clayey soils, unsaturated clay strengths do not need to be modified as a result of submersion caused by tsunami inundation.

In calculating the normal force W , it should be conservatively assumed that hydrostatic water pressure is transmitted to the bottom of the footing.

6.6 SCOUR AND EROSION

A tsunami event typically consists of multiple inundation and retreat cycles. The relative size of each cycle varies unpredictably and for design these cycles are considered equally large. Scour that occurs in one cycle degrades the foundation performance in the next cycle. For design, foundation performance shall be evaluated for a total scour condition that includes:

- local scour at the foundation caused by the tsunami inundation
- long-term degradation of the river bed
- contraction scour

Estimation of potential scour shall follow the procedures described in *Evaluating Scour at Bridges, Fifth Edition* (Arneson, et al, 2012). Scour mitigation and design methods are described in *Bridge Scour and Stream Instability Countermeasures: Experience, Selection, and Design Guidance-Third Edition* (Lagasse, et al, 2009).

6.7 RAPID DRAWDOWN

Retreat of tsunami inundation may lead to rapid drawdown of water levels. If the drawdown occurs faster than the embankments slopes can drain, the resulting hydraulic gradient imposes a downslope force that can result in slope instability. If survivability of approach embankments is

a performance goal, the stability of these slopes must be evaluated for the effects of rapid drawdown.

Army Corp EM 110-2-1902 Slope Stability Appendix G provides procedures and design examples for the case of rapid drawdown. A chart-based solution is available in Moregenstern (1963).

Mitigation approaches include use of free draining embankment material, placement of an impervious near surface layer, or use of flatter more stable slopes. Rock buttresses can be used to both improve stability and provide armoring against scour.

7.0 REFERENCES

- American Association of State Highway and Transportation Officials (AASHTO). (2017). *LRFD bridge design specifications* (8th ed.). Washington, DC: American Association of State Highway and Transportation Officials.
- Arcos, M.E.M., LeVeque, R.J. (2015). Validating velocities in the GeoClaw tsunami model using observations near Hawaii from the 2011 Tohoku tsunami. *Pure Appl. Geophys.*, 172, 849-867. doi:10.1007/s00024-014-0980-y
- Arneson, L., Zevenbergen, L., Lagasse, P., & Clopper, P. (2012). *Evaluating Scour at Bridges Fifth Edition* (Publication No. FHWA-HIF-12-003). Washington, D.C.: Office of Bridge Technology.
- American Society of Civil Engineers (ASCE). (2017). *Minimum design loads for buildings and other structures* (ASCE/SEI 7-16). Reston, VA: ASCE, American Society of Civil Engineers.
- Azadbakht, M., & Yim, S. (2015). Simulation and estimation of tsunami loads on bridge superstructures. *Journal of Waterway, Port, Coastal, and Ocean Engineering*, 141(2). doi:10.1061/(ASCE)WW.1943-5460.0000262
- Azadbakht, M., & Yim, S. (2016). Estimation of Cascadia local tsunami loads on Pacific Northwest bridge superstructures. *Journal of Bridge Engineering*, 21(2). doi:10.1061/(ASCE)BE.1943-5592.0000755
- Becker, J. J., Sandwell, D. T., Smith, W. H., Braud, J., Binder, B., Depner, J., . . . Weatherall, P. (2009). Global Bathymetry and Elevation Data at 30 Arc Seconds Resolution: SRTM30_PLUS. *Marine Geodesy*, 32(4), 355-371. doi:10.1080/01490410903297766
- Berger, M., George, D., LeVeque, R., & Mandli, K. (2011). The GeoClaw software for depth-averaged flows with adaptive refinement. *Advances in Water Resources*, 34(9), 1195-1206. doi:10.1016/j.advwatres.2011.02.016
- Bradner, C., Schumacher, T., Cox, D., & Higgins, C. (2011). Experimental setup for a large-scale bridge superstructure model subjected to waves. *Journal of Waterway, Port, Coastal, and Ocean Engineering*, 137(1). doi:10.1061/(ASCE)WW.1943-5460.0000059
- Bricker, J., Kawashima, K., & Nakayama, A. (2011). CFD analysis of bridge deck failure due to tsunami. In *International Symposium on Engineering Lessons Learned from the 2011 Great East Japan Earthquake* (pp. 1398-1409). Tokyo, Japan.
- California Probabilistic Tsunami Hazard Analysis Work Group. (2015). *Evaluation and Application of Probabilistic Tsunami Hazard Analysis in California* (Special Report: 237). Sacramento, CA: California Department of Conservation California Geological Survey.

- Casey, T. (2014). *Multi-hazard framework and analysis of soil-bridge systems: Long duration earth-quake and tsunami loading* (Doctoral dissertation, Oregon State University, 2014). Corvallis, OR: Oregon State University. Retrieved from https://ir.library.oregonstate.edu/concern/graduate_thesis_or_dissertations/9593v082s.
- Chen, R., Frankel, A., Petersen, M., Moschetti, M., & Sherrod, B. (2015). 2014 Update of the Pacific Northwest Portion of the U.S. National Seismic Hazard Maps. *Earthquake Spectra*, 31(1_suppl). doi:10.1193/111314eqs193m
- Douglass, S., Chen, Q., Olsen, J., Edge, B., & Brown, D. (2006). *Waves Forces on Bridge Decks* (Publication). Washington, D.C.: Federal Highway Administration Office of Bridge Technology.
- Eakins, B., & Taylor, L. (2010). Seamlessly integrating bathymetric and topographic data to support tsunami modeling and forecasting efforts. In 956284079 744791856 J. Breman (Author), *Ocean globe* (pp. 37-56). Redlands, CA: ESRI Press Academic.
- Earthquake Research Committee. (2005). *National Seismic Hazard Maps for Japan* (Publication). Tokyo, Japan: Headquarters for Earthquake Research Promotion. Retrieved from https://www.jishin.go.jp/main/chousa/06mar_yosoku-e/NationalSeismicHazardMaps.pdf.
- Eisner, R. K., Borrero, J. C., & Synolakis, C. (2001). *Inundation maps for the State of California*. Seattle, WA: NOAA/Pacific Marine Environmental Laboratory.
- Fluck, P., Hyndman, R., & Wang, K. (1997). Three-dimensional dislocation model for great earthquakes of the Cascadia subduction zone. *Journal of Geophysical Research: Solid Earth*, 102(B9). doi:10.1029/97JB01642
- Frankel, A., & Petersen, M. (2012). *Appendix P—Models of Earthquake Recurrence and Down-Dip Edge of Rupture for the Cascadia Subduction Zone* (Publication No. Ofr2013-1165). Reston, VA: U.S. Geological Survey. Retrieved from https://pubs.usgs.gov/of/2013/1165/pdf/ofr2013-1165_appendixP.pdf
- Geist, E. L., & Parsons, T. (2006). Probabilistic Analysis of Tsunami Hazards. *Natural Hazards*, 37(3), 277-314. doi:10.1007/s11069-005-4646-z
- George, D. L. (2008). Augmented Riemann solvers for the shallow water equations over variable topography with steady states and inundation. *Journal of Computational Physics*, 227(6), 3089-3113. doi:10.1016/j.jcp.2007.10.027
- George, D., & LeVeque, R. (2006). Finite volume methods and adaptive refinement for global tsunami propagation and local inundation. *Science of Tsunami Hazards*, 24(5), 319-328. Retrieved from <https://digital.lib.washington.edu/researchworks/bitstream/handle/1773/4639/tsunami06.pdf?sequence=1&isAllowed=y>
- Goldfiner, C., Nelson, C., Morey, A., Johnson, J., Patton, J., Karabanov, E., . . . Vallier, T. (2012). *Turbidite Event History—Methods and Implications for Holocene*

- Paleoseismicity of the Cascadia Subduction Zone* (Ser. 1661, Publication No. 1661- F). Reston, VA: U.S. Geological Survey. doi:10.3133/pp1661F
- Gonzalez, F., Bernard, E., Dunbar, P., Geist, E., Jaffe, B., Kanoglu, U., . . . Weiss, R. (2007). *Scientific and technical issues in tsunami hazard assessment of nuclear power plant sites* (Publication No. OAR PMEL-136). Seattle, WA: Pacific Marine Environmental Laboratory.
- González, F. I., Geist, E. L., Jaffe, B., Kânoğlu, U., Mofjeld, H., Synolakis, C. E., . . . Yalciner, A. (2009). Probabilistic tsunami hazard assessment at Seaside, Oregon, for near- and far-field seismic sources. *Journal of Geophysical Research*, 114(C11). doi:10.1029/2008jc005132
- Gonzalez, F., LeVeque, R., & Adams, L. (2013). *Probabilistic Tsunami Hazard Assessment (PTHA) for Crescent City, CA. Final Report for Phase I* (Tech.). Seattle, WA: University of Washington Department of Applied Mathematics.
- Gonzalez, F., LeVeque, R., Chamberlain, P., Hirai, B., Varkovitzky, J., & George, D. (2011). GeoClaw results for the NTHMP tsunami benchmark problems. In *2011 NTHMP Model Benchmarking Workshop*. Boulder, Colorado: National Tsunami Hazard Mitigation Program.
- Hannigan, P., Rausche, F., Likins, G., Robinson, B., & Becker, M. (2016). *Geotechnical Engineering Circular No. 12 – Volume I Design and Construction of Driven Pile Foundations* (Publication No. FHWA-NHI-16-009). Washington, D.C.: National Highway Institute U.S. Department of Transportation Federal Highway Administration.
- Hayatdavoodi, M., Seiffert, B., & Ertekin, R. C. (2014). Experiments and computations of solitary-wave forces on a coastal-bridge deck. Part II: Deck with girders. *Coastal Engineering*, 88, 210-228. doi:10.1016/j.coastaleng.2014.02.007
- Hayes, G. P., Wald, D. J., & Johnson, R. L. (2012). Slab1.0: A three-dimensional model of global subduction zone geometries. *Journal of Geophysical Research: Solid Earth*, 117(B1). doi:10.1029/2011jb008524
- Hoshikuma, J., Zhang, G., Nakao, H., & Sumimura, T. (2013). Tsunami-induced effects on girder bridges. In *International Symposium for Bridge Earthquake Engineering in Honor of Retirement of Professor Kazuhiko Kawashima, Tokyo, Japan* (Vol. 15).
- Istrati, D., Buckle, I., & Itani, A. (2016). Experimental study of connection forces in bridges during tsunami inundation. In *PEER Annual Meeting*. Berkeley, CA: University of California. doi:10.13140/RG.2.2.26463.30886
- Koshimura, S., & Hayashi, S. (2012). Tsunami flow measurement using the video recorded during the 2011 Tohoku tsunami attack. *2012 IEEE International Geoscience and Remote Sensing Symposium*, 6693-6696. doi:10.1109/igarss.2012.6352063

- Kriebel, D. L., Lynett, P. J., Cox, D. T., Petroff, C. M., Robertson, I. N., & Chock, G. Y. (2017). Energy Method for Approximating Overland Tsunami Flows. *Journal of Waterway, Port, Coastal, and Ocean Engineering*, 143(5). doi:10.1061/(asce)ww.1943-5460.0000393
- Lagasse, P., Clopper, P., Pagan-Ortiz, J., Zevenbergen, L., Arneson, L., Schall, J., & Girard, L. (2009). *Bridge Scour and Stream Instability Countermeasures: Experience, Selection, and Design Guidance-Third Edition* (Vol. 1 & 2, Publication No. FHWA NHI HEC-23). Washington, D.C.: Office of Bridge Technology.
- Lehrman, J. B., Higgins, C., & Cox, D. (2012). Performance of Highway Bridge Girder Anchorages under Simulated Hurricane Wave Induced Loads. *Journal of Bridge Engineering*, 17(2), 259-271. doi:10.1061/(asce)be.1943-5592.0000262
- Leveque, R. J. (1997). Wave Propagation Algorithms for Multidimensional Hyperbolic Systems. *Journal of Computational Physics*, 131(2), 327-353. doi:10.1006/jcph.1996.5603
- LeVeque, R. J. (2002). *Finite volume methods for hyperbolic problems*. Cambridge: Cambridge Univ. Press. doi:10.1017/CBO9780511791253
- LeVeque, R. J., & George, D. L. (2008). High-Resolution Finite Volume Methods For The Shallow Water Equations With Bathymetry And Dry States. *Advances in Coastal and Ocean Engineering Advanced Numerical Models for Simulating Tsunami Waves and Runup*, 43-73. doi:10.1142/9789812790910_0002
- Liu, P. L., Cho, Y., Briggs, M. J., Kanoglu, U., & Synolakis, C. E. (1995). Runup of solitary waves on a circular Island. *Journal of Fluid Mechanics*, 302, 259-285. doi:10.1017/s0022112095004095
- Løvholt, F., Glimsdal, S., Harbitz, C. B., Zamora, N., Nadim, F., Peduzzi, P., . . . Smebye, H. (2012). Tsunami hazard and exposure on the global scale. *Earth-Science Reviews*, 110(1-4), 58-73. doi:10.1016/j.earscirev.2011.10.002
- Lynett, P. J., Borrero, J. C., Weiss, R., Son, S., Greer, D., & Renteria, W. (2012). Observations and modeling of tsunami-induced currents in ports and harbors. *Earth and Planetary Science Letters*, 327-328, 68-74. doi:10.1016/j.epsl.2012.02.002
- Lynett, P. J., Borrero, J., Son, S., Wilson, R., & Miller, K. (2014). Assessment of the tsunami-induced current hazard. *Geophysical Research Letters*, 41(6), 2048-2055. doi:10.1002/2013gl058680
- Lynett, P. J., Gately, K., Wilson, R., Montoya, L., Arcas, D., Aytore, B., . . . Zhang, Y. (2017). Inter-model analysis of tsunami-induced coastal currents. *Ocean Modelling*, 114, 14-32. doi:10.1016/j.ocemod.2017.04.003
- Lynett, P., & Thio, H. (2020). *Validation of Tsunami Design Guidelines for Coastal Bridges*. Retrieved from Tsunami Database Files. doi:10.9753/TPF.suppl.1

- Mandli, K. T., Ahmadi, A. J., Berger, M., Calhoun, D., George, D. L., Hadjimichael, Y., . . . Leveque, R. J. (2016). Clawpack: Building an open source ecosystem for solving hyperbolic PDEs. *PeerJ Computer Science*, 2. doi:10.7717/peerj-cs.68
- Mccrory, P. A., Blair, J. L., Waldhauser, F., & Oppenheimer, D. H. (2012). Juan de Fuca slab geometry and its relation to Wadati-Benioff zone seismicity. *Journal of Geophysical Research: Solid Earth*, 117(B9). doi:10.1029/2012jb009407
- McGuire, R. K. (2004). *Seismic hazard and risk analysis*. Oakland: Earthquake Engineering Research Institute.
- McPherson, R. L. (2008). *Hurricane induced wave and surge forces on bridge decks* (Master's thesis, Texas A&M University, 2008). Collage Station: Texas A&M University.
- Mofjeld, H. O., González, F. I., Titov, V. V., Venturato, A. J., & Newman, J. C. (2007). Effects of Tides on Maximum Tsunami Wave Heights: Probability Distributions*. *Journal of Atmospheric and Oceanic Technology*, 24(1), 117-123. doi:10.1175/jtech1955.1
- Moregenstern, N. (1963). Stability Charts for Earth Slopes During Rapid Drawdown. *Géotechnique*, 13(2), 121-131. doi:10.1680/geot.1963.13.2.121
- Mori, N., Takahashi, T., Yasuda, T., & Yanagisawa, H. (2011). Survey of 2011 Tohoku earthquake tsunami inundation and run-up. *Geophysical Research Letters*, 38(7). doi:10.1029/2011gl049210
- Motley, M. R., Wong, H. K., Qin, X., Winter, A. O., & Eberhard, M. O. (2016). Tsunami-Induced Forces on Skewed Bridges. *Journal of Waterway, Port, Coastal, and Ocean Engineering*, 142(3), 04015025. doi:10.1061/(asce)ww.1943-5460.0000328
- Murotani, S., Miyake, H., & Koketsu, K. (2008). Scaling of characterized slip models for plate-boundary earthquakes. *Earth, Planets and Space*, 60(9), 987-991. doi:10.1186/bf03352855
- Murotani, S., Satake, K., & Fujii, Y. (2013). Scaling relations of seismic moment, rupture area, average slip, and asperity size for M ~9 subduction-zone earthquakes. *Geophysical Research Letters*, 40(19), 5070-5074. doi:10.1002/grl.50976
- Naito, C., Cercone, C., Riggs, H. R., & Cox, D. (2014). Procedure for Site Assessment of the Potential for Tsunami Debris Impact. *Journal of Waterway, Port, Coastal, and Ocean Engineering*, 140(2), 223-232. doi:10.1061/(asce)ww.1943-5460.0000222
- Nakao, H., Zhang, G., Sumimura, T., & Hoshikuma, J. I. (2013). Numerical assessment of tsunami-induced effect on bridge behavior. In *Proceedings of the 29th US-Japan Bridge Engineering Workshop, Tsukuba, Japan* (pp. 11-13).
- Okada, Y. (1992). Internal deformation due to shear and tensile faults in a half-space. *Bulletin of the Seismological Society of America*, 82(2), 1018-1040.

- Petersen, M. D., Moschetti, M., Powers, P., Mueller, C. S., Haller, K. M., Frankel, A., . . . Olsen, A. (2008). Documentation for the 2014 update of the United States National Seismic Hazard Maps. *Open-File Report, 2014-1091*. doi:10.3133/ofr20141091
- Scott, M., Yeh, H., & Cressman, L. (2014, December 15). UJNR Tsunami Modeling Workshop. In *UJNR Tsunami Modeling Workshop*. Retrieved from <https://secure.engr.oregonstate.edu/wiki/tsunamiworkshop/index.php?n=Main.HomePage>
- Seiffert, B., Hayatdavoodi, M., & Ertekin, R. C. (2014). Experiments and computations of solitary-wave forces on a coastal-bridge deck. Part I: Flat Plate. *Coastal Engineering, 88*, 194-209. doi:10.1016/j.coastaleng.2014.01.005
- Shennan, I., Bruhn, R., & Plafker, G. (2009). Multi-segment earthquakes and tsunami potential of the Aleutian megathrust. *Quaternary Science Reviews, 28*(1-2), 7-13. doi:10.1016/j.quascirev.2008.09.016
- Synolakis, C., Bernard, E., Titov, V., Kanoglu, U., & Gonzalez, F. (2007). *Standards, criteria, and procedures for NOAA evaluation of tsunami numerical models* (Publication No. OAR PMEL-135). Seattle, WA: Pacific Marine Environmental Laboratory.
- Mori, N., & Takahashi, T. (2012). Nationwide Post Event Survey and Analysis of the 2011 Tohoku Earthquake Tsunami. *Coastal Engineering Journal, 54*(1). doi:10.1142/s0578563412500015
- Thio, H. K., Somerville, P., & Ichinose, G. (2007). Probabilistic Analysis Of Strong Ground Motion And Tsunami Hazards In Southeast Asia. *Journal of Earthquake and Tsunami, 01*(02), 119-137. doi:10.1142/s1793431107000080
- Thio, H., Somerville, P., & Polet, J. (2010). *Probabilistic tsunami hazard in California* (Publication No. 2010/108). Berkeley, CA: Pacific Earthquake Engineering Research Center.
- Thio, H., Somerville, P., & Polet, J. (2012). Probabilistic tsunami hazard analysis. In *15th World Conference on Earthquake Engineering* (Vol. 38, pp. 30334-30342). Lisbon, Portugal: Sociedade Portuguesa de Engenharia Sismica.
- Thio, H., Wei, Y., Chock, G., & Li, W. (2017). Development of Offshore Probabilistic Tsunami Exceedance Amplitudes for ASCE 7-16. In *16th World Conference on Earthquake Engineering*. Santiago, Chile: International Association for Earthquake Engineering.
- Titov, V., & Synolakis, C. (1995). Modeling of Breaking and Nonbreaking Long-Wave Evolution and Runup Using VTCS-2. *Journal of Waterway, Port, Coastal, and Ocean Engineering, 121*(6), 308-316.
- Titov, V., & Gonzalez, F. (1997). *Implementation and testing of the Method of Splitting Tsunami (MOST) Model* (Publication No. ERL PMEL-112). Seattle, WA: NOAA/Pacific Marine Environmental Laboratory.

- Titov, V. (2009). Tsunami Forecasting. In *The Sea Tsunamis* (Vol. 15, pp. 371-400). Crambridge, MA: Harvard University Press.
- US Army Corps of Engineers. (2003). *Engineering and Design Slope Stability* (Standard No. EM 1110-2-1902) Retrieved from https://www.publications.usace.army.mil/Portals/76/Publications/EngineerManuals/EM_1110-2-1902.pdf
- Vick, S. G. (2002). *Degrees of belief: Subjective probability and engineering judgment*. Reston, VA: American Society of Civil Engineers.
- Wang, R. (2003). Computation of deformation induced by earthquakes in a multi-layered elastic crust—FORTRAN programs EDGRN/EDCMP. *Computers & Geosciences*, 29(2), 195-207. doi:10.1016/s0098-3004(02)00111-5
- Wang, K., Wells, R., Mazzotti, S., Hyndman, R. D., & Sagiya, T. (2003). A revised dislocation model of interseismic deformation of the Cascadia subduction zone. *Journal of Geophysical Research: Solid Earth*, 108(B1). doi:10.1029/2001jb001227
- Wei, Y., Chamberlin, C., Titov, V. V., Tang, L., & Bernard, E. N. (2012). Modeling of the 2011 Japan Tsunami: Lessons for Near-Field Forecast. *Pure and Applied Geophysics*, 170(6-8), 1309-1331. doi:10.1007/s00024-012-0519-z
- Wei, Y., Thio, H.K., Titov, V., Chock, G., Zhou, H., Tang, L., & Moore, C. (2017). Inundation Modeling to Create 2,500-Year Return Period Tsunami Design Zone Maps for the Asce 7-16 Standard. In *16th World Conference on Earthquake Engineering*. Santiago, Chile: International Association for Earthquake Engineering.
- Wesson, R. L., Boyd, O. S., Mueller, C. S., Bufe, C. G., Frankel, A. D., & Petersen, M. D. (2007). Revision of Time-Independent Probabilistic Seismic Hazard Maps for Alaska. *Open-File Report*. doi:10.3133/ofr20071043
- Winter, A. O., Motley, M. R., & Eberhard, M. O. (2018). Tsunami-Like Wave Loading of Individual Bridge Components. *Journal of Bridge Engineering*, 23(2), 04017137. doi:10.1061/(asce)be.1943-5592.0001177
- Witter, R. C., Carver, G. A., Briggs, R. W., Gelfenbaum, G., Koehler, R. D., Selle, S. L., . . . Hill, T. D. (2016). Unusually large tsunamis frequent a currently creeping part of the Aleutian megathrust. *Geophysical Research Letters*, 43(1), 76-84. doi:10.1002/2015gl066083
- Xiang, T. (2016). *Large-Scale Laboratory Experiment and Numerical Simulation of Tsunami Forces on a Bridge Deck* (Master's thesis, Oregon State University, 2016). Corvallis: Oregon State University.
- Yeh, H. H., Ghazali, A., & Marton, I. (1989). Experimental study of bore run-up. *Journal of Fluid Mechanics*, 206, 563-578. doi:10.1017/s0022112089002417
- Yokota, Y., Koketsu, K., Fujii, Y., Satake, K., Sakai, S., Shinohara, M., & Kanazawa, T. (2011). Joint inversion of strong motion, teleseismic, geodetic, and tsunami datasets for the

rupture process of the 2011 Tohoku earthquake. *Geophysical Research Letters*, 38(7).
doi:10.1029/2011gl050098

APPENDIX A: SOURCE CODE FOR MATLAB TRANSECT TOOL

The source code for the developed program is provided here, in entirety.

master.m

```
% This is the master script used to access the transect analysis tool
% Developed by Patrick Lynett, USC

% clear memory
fclose all;
clear all

% Inputs
suppress_figs=0; % =1, do not plot various transect and EM figs

% structure location - input lat, lon
%xs=-124.057108; % longitude CA
%ys=41.556267; % latitude CA
%xs=-122.4350; % longitude CA
%ys=37.47; % latitude CA
%xs=-157.9450; % longitude OAHU
%ys=21.330; % latitude OAHU
%xs=-146.2500; % longitude AK
%ys=61.09; % latitude AK
%xs=-122.4100; % longitude WA
%ys=48.545; % latitude WA
%xs=-124.0660; % longitude OR
%ys=43.7049; % latitude OR

% or, have Matlab prompt for the design site location
disp('USER INPUT: Specify the site information');
ys=input('USER INPUT: Enter site latitude (degrees N, 0-90): ');
xs=input('USER INPUT: Enter site longitude (degrees W, -180-0): ');

% should not need to change anything below this

home_dir=cd; % store current working directory
database_dir='runup_data'; % name of subdir where tsunami database files are located

% plot grid database map
plot_database=0; % change to 1 for debugging or curiosity purposes, will show locations of
inundation grids
if plot_database==1
    cd(database_dir)
    figure(1)
    close(1)
    openfig('TsunamiGrids.fig');
    cd(home_dir)
end

% check to see if database grid that covers the datapoint exists
cd(database_dir)
load box_coords.mat % data file that contains the coordinates of all the inundation grids
[m,n]=size(box_coords);
find_grid=0; % check boolean
char_names=char(fname_TD{1}); % object that contains the database grid names
for i=1:m
    coords_c=box_coords(i,:); % x and y limits of the current inundation grid
    if xs>=coords_c(1) & xs<=coords_c(2) & ys>=coords_c(4) & ys<=coords_c(3) % does site
location exist inside the inundation grid?
        find_grid=i;
        disp(['Structure location exists in database grid: ' char_names(i,:)]);
        break
    end
end

if find_grid==0 % if site location isnt in an inundation grid, spit out error
    error('ERROR: Structure location does not exist within the bounds of any database grid')
end

% load proper database file
```

```

disp('Loading raw bathytopo and runup file')
fname=strtrim(char_names(i,:));
fname_mat=[fname(1:length(fname)-3) 'mat'];
load(fname_mat)
fname_bathytopo=fname;

% pull subsidence values nearest to site
cd subsidence
load subsidence_database.mat
dist=sqrt( (xs-data_sub(:,1)).^2 + (ys-data_sub(:,2)).^2);
subsidence=data_sub(find(dist==min(dist),1),3);
if subsidence<0 | isnan(subsidence)==1
    subsidence=0;
end
disp(['Subsidence at site (m) = ' num2str(subsidence)])
fname=fname_bathytopo;

cd(home_dir)

% set dry areas to flowdepth of 0
dry_nodes=find(flowdepth<=0);
flowdepth(dry_nodes)=flowdepth(dry_nodes)*0;

% plot offshore, shoreline, and inundation line contours.
% plot bathy/topo
figure(2)
clf
subcols=4;
subplot(1,subcols,1:subcols-1)

% reduce plotting size, in case of large surfaces
max_pcolor_pts=300;
int_x=1;
n_lon=length(lon);
if n_lon>max_pcolor_pts
    int_x=round(n_lon/max_pcolor_pts);
end
int_y=1;
n_lat=length(lat);
if n_lat>max_pcolor_pts
    int_y=round(n_lat/max_pcolor_pts);
end

pcolor(lon(1:int_x:n_lon),lat(1:int_y:n_lat),bathytopo(1:int_y:n_lat,1:int_x:n_lon));
shading interp
axis equal
x_s=max(min(lon),xs-0.025);
x_e=min(max(lon),xs+0.025);
y_s=max(min(lat),ys-0.025);
y_e=min(max(lat),ys+0.025);
axis([x_s x_e y_s y_e])
caxis([-10 25])
colorbar
hold on
xlabel('Longitude (degrees)')
ylabel('Latitude (degrees)')
title(['Bathy/Topo from Tsunami Grid Database File ' fname], 'Interpreter', 'none')

% plot initial shoreline and runup inundation limit
plot(shoreline_ts(:,3),shoreline_ts(:,4),'r.')
plot(runup_ts(:,3),runup_ts(:,4),'k.')

% plot structure location, make it look like a bullseye with 4 circles
plot(xs,ys,'w.','MarkerSize',20)
plot(xs,ys,'wo','MarkerSize',10)
plot(xs,ys,'wo','MarkerSize',15)
plot(xs,ys,'wo','MarkerSize',20)

% check to see if site is in inundation zone
H_site=interp2(lon,lat,flowdepth,xs,ys,'Nearest'); % find the flowdepth at the site location
Vel_site=interp2(lon,lat,flowdepth,xs,ys,'Nearest'); % find the flowdepth at the site location
if H_site<=0 % if dry
    error('ERROR: Structure location is not in tsunami inundation zone')

```

```

elseif Vel_site<=0
    disp('WARNING: Site is on Edge of Inundation Zone, with Non-Physical Velocity. Database
velocity values should not be used.')
end

% check to see if site is on initially dry land
d_site=interp2(lon,lat,bathytopo,xs,ys); % find the ground/seafloor elevation
if d_site<=0 % if site location is initially wet
    disp('WARNING: Structure location is over ocean water, EGL approach may not work. Use
database values if possible.')
end

% pull database values of flow elevation and depth
gridsize_site=median(diff(lon)); % grid size of inundation grid where site location exists
speed_site=interp2(lon,lat,flowvelocity,xs,ys,'Nearest'); % speed from database
momflux_site=interp2(lon,lat,momflux,xs,ys,'Nearest'); % momentum flux from database

%%% generate user defined, riverine transect
click_count=0; % general loop counter
site_click=0; % checks if user has clicked on site (becomes =click_count when clicked on site)
dry_click=0; % checks if user has clicked on a dry (non-inundated) area (becomes 1)

disp('Click on map for riverine transect. Hit right mouse button to snap to site')
% Display instructions
txt_x=x_e+0.1*(x_e-x_s);
txt_y=y_e-0.2*(y_e-y_s);
h_txt1=text(txt_x, txt_y,'Click on map for riverine transect. Hit right mouse button to snap to
site');

while dry_click==0 % as long as user is working in an inundated area, continue

    click_count=click_count+1;
    [xr(click_count) yr(click_count), button] = ginput(1); % user clicks and ginput stores the
click position

    if site_click~=0 % check for dry click. but only after site has been clicked
        H_c=interp2(lon,lat,flowdepth,xr(click_count),yr(click_count)); % find flowdepth at
current click location
        if H_c<=0 % if dry
            dry_click=1;
        end
    end

    if button~=1 % snap to site with right mouse button click
        xr(click_count)=xs; % over-write clicked locations with site locations
        yr(click_count)=ys;
        site_click=click_count; % store site_click point
        delete(h_txt1)
        disp('Click on map for riverine transect. Click on dry point to terminate transect')
        h_txt1=text(txt_x, txt_y,'Click on map for riverine transect. Click on dry point to
terminate transect');

    end

    % plot transect points as transect is being created
    plot(xr,yr,'w.','MarkerSize',5)
    plot(xr,yr,'g','LineWidth',3)
end
delete(h_txt1)
%%% riverine transect created

%%% generate straight transects
% user defined direction for transect, should be representative of the
% compass heading direction towards the nearest or most relevant open ocean
% shoreline, North=0, East=90, South=180, West=270
disp('Click on Open Ocean Shoreline Location to be used to Generate Straight Transects')
disp('Right-click on mouse when happy with the line orientation')

% Display instructions
txt_y=y_e-0.2*(y_e-y_s);
h_txt1=text(txt_x, txt_y,'Click on Open Ocean Shoreline Location to be used to Generate Straight
Transects');

```

```

txt_y=y_e-0.25*(y_e-y_s);
h_txt2=text(txt_x, txt_y, 'Right-click on mouse when happy with the line orientation');

button=1;
while button==1 % continue until user right clicks mouse button
    [x_shore,y_shore,button] = ginput(1); % user clicks and ginput stores the click position
    if button==1
        if exist('trans_handle')~=0 % clear old figure handle if it exists
            delete(trans_handle)
        end
        transect_heading=acotd( (y_shore-ys)/(x_shore-xs)); % determine heading

        sector_spread=10; % this is the spread angle of the upper and lower straight transects
        nx=length(lon);
        ny=length(lat);

        % center transect coordinates
        xt=[x_shore xs xs+10*(xs-x_shore)];
        yt=[ys-(xs-xt(1))*cotd(transect_heading) ys ys-(xs-xt(3))*cotd(transect_heading)];

        % +sector_spread transect coordinates
        xt_u=xt;
        yt_u=[ys-(xs-xt(1))*cotd(transect_heading+sector_spread) ys ys-(xs-
xt(3))*cotd(transect_heading+sector_spread)];

        % -sector_spread transect coordinates
        xt_l=xt;
        yt_l=[ys-(xs-xt(1))*cotd(transect_heading-sector_spread) ys ys-(xs-
xt(3))*cotd(transect_heading-sector_spread)];

        % plot the three lines
        trans_handle=plot(xt,yt,'w',xt_u,yt_u,'w--',xt_l,yt_l,'w--','LineWidth',3);
    end

    % create transects with small grid length
    % all transects should be generated with offshore part of transect in first row/column, i.e.
    transect profile starts offshore and moves inland
    if suppress_figs~=1
        figure(3)
        clf
    end

    n_trans=2000; % create transect with 2000 points for straight segments

    % shore-normal, center transect

    [s_trans,z_trans,H_trans,site_s,site_z]=create_transects(xt,yt,lon,lat,bathytopo,flowdepth,xs,ys,
n_trans); % create transect with n_trans points
    if suppress_figs~=1 % plot transect
        subplot(4,1,1)
        plot(s_trans,z_trans+H_trans,s_trans,z_trans)
        title('Shore-normal Straight Transect')
        hold on
        plot(site_s,site_z,'g.','MarkerSize',20)
        legend('Database-Extracted Flow Elevation','Database Transect Profile','Site Location')
    end

    % check transect

    [s_trans,z_trans,H_trans,dist_runup,profile_check]=check_transects(s_trans,z_trans,H_trans,site_s
); % check transect see if any "wet" points in the transect are higher elevation than the runoff
point

    if suppress_figs~=1
        if profile_check==1 % plot modified transect, if modification was needed
            plot(s_trans,z_trans,'r--')
            legend('Database-Extracted Flow Elevation','Database Transect Profile','Site
Location','Modified Transect for EM Calc')
        end
        axis([-Inf dist_runup+100 -20 50])
    end

    % shore-normal upper straight

```

```

[s_trans_u,z_trans_u,H_trans_u,site_s_u,site_z_u]=create_transects(xt_u,yt_u,lon,lat,bathytopo,fl
owdepth,xs,ys,n_trans); % create transect with n_trans points

    if suppress_figs~=1
        subplot(4,1,2)
        plot(s_trans_u,z_trans_u+H_trans_u,s_trans_u,z_trans_u)
        title('Upper Straight Transect')
        hold on
        plot(site_s_u,site_z_u,'g.','MarkerSize',20)
        legend('Database-Extracted Flow Elevation','Database Transect Profile','Site Location')
    end

    % check transect

[s_trans_u,z_trans_u,H_trans_u,dist_runup_u,profile_check]=check_transects(s_trans_u,z_trans_u,H_
trans_u,site_s_u); % check transect see if any "wet" points in the transect are higher elevation
than the runup point

    if suppress_figs~=1
        if profile_check==1 % plot modified transect, if modification was needed
            plot(s_trans_u,z_trans_u,'r--')
            legend('Database-Extracted Flow Elevation','Database Transect Profile','Site
Location','Modified Transect for EM Calc')
        end
        axis([-Inf dist_runup_u+100 -20 50])
    end

    % shore-normal lower straight

[s_trans_l,z_trans_l,H_trans_l,site_s_l,site_z_l]=create_transects(xt_l,yt_l,lon,lat,bathytopo,fl
owdepth,xs,ys,n_trans); % create transect with n_trans points

    if suppress_figs~=1
        subplot(4,1,3)
        plot(s_trans_l,z_trans_l+H_trans_l,s_trans_l,z_trans_l)
        title('Lower Straight Transect')
        hold on
        plot(site_s_l,site_z_l,'g.','MarkerSize',20)
        legend('Database-Extracted Flow Elevation','Database Transect Profile','Site Location')
    end

    % check transect

[s_trans_l,z_trans_l,H_trans_l,dist_runup_l,profile_check]=check_transects(s_trans_l,z_trans_l,H_
trans_l,site_s_l); % check transect see if any "wet" points in the transect are higher elevation
than the runup point

    if suppress_figs~=1
        if profile_check==1 % plot modified transect, if modification was needed
            plot(s_trans_l,z_trans_l,'r--')
            legend('Database-Extracted Flow Elevation','Database Transect Profile','Site
Location','Modified Transect for EM Calc')
        end
        axis([-Inf dist_runup_l+100 -20 50])
    end

    %%%%%%%%%%%%%%%%%%%%%%%%%%%%%%%%%%%%%%%%%%%%%%%%%%%%%%%%%%%%%%%%%%%%%%%%%
    % Create riverine transect with small grid length
    n_river=length(xr); % number of points in riverine transect
    n_trans=round(n_trans/(n_river-1)); % number of points to put in each linear segment
    site_s_rv=0;
    for i=1:n_river-1
        xtc=xr(i:i+1);
        ytc=yr(i:i+1);

[s_c,z_c,H_c,site_c,site_z_rv]=create_transects(xtc,yc,lon,lat,bathytopo,flowdepth,xs,ys,n_trans
); % use same function to create a piece of the transect, for each set of sequentially clicked
points

        % combine segments into single transect
        if i==1
            s_trans_c=s_c;

```

```

        z_trans_c=z_c;
        H_trans_c=H_c;
    else
        % chop off first point to prevent duplicate locations in combined vectors
        n_c=length(s_c);
        s_c=s_c(2:n_c);
        z_c=z_c(2:n_c);
        H_c=H_c(2:n_c);

        s_trans_c=[s_trans_c s_c+s_trans_c(length(s_trans_c))];
        z_trans_c=[z_trans_c z_c];
        H_trans_c=[H_trans_c H_c];
    end

    end

    if i<=site_click-1
        site_s_rv=site_s_rv+ s_c(length(s_c));
        site_z_rv=interp1(s_trans_c,z_trans_c,site_s_rv);
    end
end

% since spacing for each segment is different, interp combined vectors to regular spaced grid
ave_ds=mean(diff(s_trans_c));
s_trans_rv=[s_trans_c(1):ave_ds:s_trans_c(length(s_trans_c))];
z_trans_rv=interp1(s_trans_c,z_trans_c,s_trans_rv);
H_trans_rv=interp1(s_trans_c,H_trans_c,s_trans_rv);

%plot riverine transect
if suppress_figs~=1
    subplot(4,1,4)
    plot(s_trans_rv,z_trans_rv+H_trans_rv,s_trans_rv,z_trans_rv)
    title('Riverine Transect')
    hold on
    plot(site_s_rv,site_z_rv,'g.','MarkerSize',20)
    legend('Database-Extracted Flow Elevation','Database Transect Profile','Site Location')
end

% check transect

[s_trans_rv,z_trans_rv,H_trans_rv,dist_runup_rv,profile_check]=check_transects(s_trans_rv,z_trans_rv,H_trans_rv,site_s_rv);% check transect see if any "wet" points in the transect are higher elevation than the runup point

if suppress_figs~=1
    if profile_check==1 % plot modified transect, if modification was needed
        plot(s_trans_rv,z_trans_rv,'r--')
        legend('Database-Extracted Flow Elevation','Database Transect Profile','Site Location','Modified Transect for EM Calc')
    end
    axis([-Inf dist_runup+100 -20 50])
end

% run Energy Grade Line Method over the four transects created above
disp('Running Energy Grade Line Method on Transects')
for i_trans=1:4
    if i_trans==1
        z=z_trans;
        s=s_trans;
        dist=dist_runup;
        site=site_s;
        title_txt='Shore-normal Straight Transect';
        river_flag=0;
        fig_ind=4;
    elseif i_trans==2
        z=z_trans_u;
        s=s_trans_u;
        dist=dist_runup_u;
        site=site_s_u;
        title_txt='Upper Straight Transect';
        river_flag=0;
        fig_ind=5;
    elseif i_trans==3
        z=z_trans_l;
        s=s_trans_l;

```

```

        dist=dist_runup_l;
        site=site_s_l;
        title_txt='Lower Straight Transect';
        river_flag=0;
        fig_ind=6;
    elseif i_trans==4
        z=z_trans_rv;
        s=s_trans_rv;
        dist=dist_runup_rv;
        site=site_s_rv;
        title_txt='Riverine Transect';
        river_flag=1;
        fig_ind=7;
    end

[flow_depth(i_trans),flow_elevation(i_trans),flow_speed(i_trans),momentum_flux(i_trans)]=run_EM(z
,s,dist,site,0,river_flag,fig_ind,title_txt,suppress_figs,subsidence); % Run EGL method
end

% Average the middle two estimates to determine design values
sorted_flow_depth=sort(flow_depth,'descend');
sorted_flow_speed=sort(flow_speed,'descend');

design_flow_depth=mean(sorted_flow_depth(2:3));
design_flow_speed=mean(sorted_flow_speed(2:3));

% Important output
disp('-----')
disp('Energy Grade Line Outputs:')
disp('          Values from:  Shore Transect | Upper Transect | Lower Transect | River
Transect')
disp(['TRANSECT Flow depths (m) @ structure site = ' num2str(flow_depth)])
disp(['TRANSECT Flow elevations (m, MHW) @ structure site = ' num2str(flow_elevation)])
disp(['TRANSECT Flow speeds (m/s) @ structure site = ' num2str(flow_speed)])
%disp(['TRANSECT Momentum Fluxes (m^3/s^2) @ structure site = ' num2str(momentum_flux)])
disp('-----EGL DESIGN VALUES-----')
disp(['DESIGN Flow depth (m) @ structure site = ' num2str(design_flow_depth)])
disp(['DESIGN Flow speed (m/s) @ structure site = ' num2str(design_flow_speed)])
disp(['Ground Elevation (m, MHW) @ structure site, including subsidence = '
num2str(site_z_rv-subsidence)])
disp('-----')
disp('-----DATABASE DESIGN VALUES-----')
disp(['Grid size of database grid (arcsec) = ' num2str(gridsize_site*3600)])
disp(['DATABASE Flow depth (m) @ structure site = ' num2str(H_site)])
disp(['DATABASE Flow speed (m/s) @ structure site = ' num2str(speed_site)])
disp(['DATABASE Flow momentum flux (m^3/s^2) @ structure site = ' num2str(momflux_site)])
disp('-----')

figure(2)

if exist('h2_txt1')~=0
    for ii=1:9
        eval(['delete(h2_txt' num2str(ii) ')'])
    end
end

txt_x=x_e+0.125*(x_e-x_s);
inc=0.04;
txt_y=y_e-0.35*(y_e-y_s);
h2_txt1=text(txt_x, txt_y,'Energy Grade Line Outputs:');
txt_y=y_e-(0.35+1*inc)*(y_e-y_s);
h2_txt2=text(txt_x, txt_y,'
Transect Values from:
Shore | Upper | Lower | River ');
txt_y=y_e-(0.35+2*inc)*(y_e-y_s);
h2_txt3=text(txt_x, txt_y,['TRANSECT Flow depths (m) @ structure site = '
num2str(flow_depth)]);
txt_y=y_e-(0.35+3*inc)*(y_e-y_s);
h2_txt4=text(txt_x, txt_y,['TRANSECT Flow elevations (m, MHW) @ site = '
num2str(flow_elevation)]);
txt_y=y_e-(0.35+4*inc)*(y_e-y_s);
h2_txt5=text(txt_x, txt_y,['TRANSECT Flow speeds (m/s) @ structure site = '
num2str(flow_speed)]);
txt_y=y_e-(0.35+5*inc)*(y_e-y_s);

```

```

h2_txt6=text(txt_x, txt_y, '-----EGL DESIGN VALUES-----');
txt_y=y_e-(0.35+6*inc)*(y_e-y_s);
h2_txt7=text(txt_x, txt_y, ['DESIGN Flow depth (m) @ structure site = '
num2str(design_flow_depth)];
txt_y=y_e-(0.35+7*inc)*(y_e-y_s);
h2_txt8=text(txt_x, txt_y, ['DESIGN Flow speed (m/s) @ structure site = '
num2str(design_flow_speed)];
txt_y=y_e-(0.35+8*inc)*(y_e-y_s);
h2_txt9=text(txt_x, txt_y, ['Ground Elevation (m, MHW) @ structure site, including subsidence
= ' num2str(site_z_rv-subsidence)];
txt_y=y_e-(0.35+9*inc)*(y_e-y_s);
h2_txt10=text(txt_x, txt_y, '-----');
txt_y=y_e-(0.35+10*inc)*(y_e-y_s);
if gridsize_site*3600<0.35
h2_txt11=text(txt_x, txt_y, ['--DATABASE DESIGN VALUES-- FINE GRID, CAN USE FOR DESIGN']);
else
h2_txt11=text(txt_x, txt_y, ['--DATABASE DESIGN VALUES-- COARSE GRID, DO NOT USE FOR
DESIGN']);
end
txt_y=y_e-(0.35+11*inc)*(y_e-y_s);
h2_txt12=text(txt_x, txt_y, ['Grid size of database grid (arcsec) = '
num2str(gridsize_site*3600)];
txt_y=y_e-(0.35+12*inc)*(y_e-y_s);
h2_txt13=text(txt_x, txt_y, ['DATABASE Flow depth (m) @ structure site = ' num2str(H_site)];
txt_y=y_e-(0.35+13*inc)*(y_e-y_s);
h2_txt14=text(txt_x, txt_y, ['DATABASE Flow speed (m/s) @ structure site = '
num2str(speed_site)];
txt_y=y_e-(0.35+14*inc)*(y_e-y_s);
h2_txt15=text(txt_x, txt_y, ['DATABASE Flow momentum flux (m^3/s^2) @ structure site = '
num2str(momflux_site)];
txt_y=y_e-(0.35+15*inc)*(y_e-y_s);
h2_txt16=text(txt_x, txt_y, '-----');
end % restart transect generation and calc process unless user right clicks

delete(h_txt1)
delete(h_txt2)
set(gcf, 'PaperPosition', [0 0 14 8]*1.35);
print -djpeg100 transect_summary.jpg

```

run_EM.m

```
function [flow_depth,flow_elevation,flow_speed,momentum_flux]=
run_EM(h_trans,s_trans,dist_runup,dist_struct,z_struct_bathy,river_flag,fig_ind,title_txt,suppres
s_figs)
% this function runs the EGL method
% this function runs the EGL method
% Note that since our transect inputs are shoreline and inundation limit
% location, and not runup elevation, we should not use the subsidence to
% shift the topo profile. Inundation limit already takes into account the
% subsidence. Subsidence should be used to correct any runup or site elevation
% that is extracted from the uncorrected bathytopo

% Hardcored Inputs
mannings_n=0.025; % mannings friction coef
alpha=1.0; % Froude number at shoreline
% end Inputs

if river_flag==1
    shore_i=1;
else
    shore_i=find(h_trans>=0,1); % shoreline i index on transect
end
runup_i=find(s_trans>=dist_runup,1)-1; % runup i index on transect

% init EM variables
hASCE=s_trans*0; % flow depth variable
FrASCE=hASCE; % Froude number
E=hASCE; % total energy
uASCE=hASCE; % speed

err=1; % init to large error

hASCE(shore_i)=max(0.1,h_trans(shore_i)); % init to some non-zero value
xASCE=(s_trans-s_trans(shore_i)); % x vector, equal to zero at shoreline

thres=0.01; % error threshold, in m
iter_count=0; % init iteration count
while iter_count<=10 & err>thres % continue if error too large and iterations less than 10
    iter_count=iter_count+1; % step up iteration count

    % shoreline values
    FrASCE(runup_i)=0; % still water at runup point, Fr, E, u, H=0
    E(runup_i)=0;
    uASCE(runup_i)=0;
    hASCE(runup_i)=E(runup_i);
    E_old=E; % previous iteration values of E
    % loop through all points in profile
    for i=runup_i-1:-1:shore_i
        dx=(xASCE(i+1)-xASCE(i)); % location horizontal grid size
        m=(h_trans(i+1)-h_trans(i))/dx; % local bottom slope
        FrASCE(i)=alpha*(1-xASCE(i)/xASCE(runup_i))^0.5; % local Fr, based on x^0.5 rule

        hm=(hASCE(i+1)+hASCE(i))/2; % local H
        Frm=(FrASCE(i+1)+FrASCE(i))/2.; % local Fr

        % calc local friction slope
        if hm>0
            S=9.81*mannings_n^2*Frm^2/(hm^(1/3)); % spreadsheet method, this is actually semi-
implicit
        else
            S=0; % force S to zero if flow depth is zero -> 1/0 problems
        end
        E(i)=max(0.001,E(i+1)+(m+S)*dx); % new E value, keep above zero
        hASCE(i)=E(i)/(1+0.5*FrASCE(i)^2); % new H
        uASCE(i)=FrASCE(i)*sqrt(9.81*hASCE(i)); % new u
    end

    if iter_count==1
        E_old=E;
    end
end
```

```

E=(E+E_old)/2; % use a corrector method, updated value is average of last old and new value.
Will converge slowly but stability
% loop through all points in profile
for i=runup_i-1:-1:shore_i % update H and u
    hASCE(i)=E(i)/(1+0.5*FrASCE(i)^2);
    uASCE(i)=FrASCE(i)*sqrt(9.81*hASCE(i));
end

err=abs(hASCE(runup_i));

if err>thres
    hASCE(shore_i)=hASCE(shore_i)-hASCE(runup_i)/2; % correct for next guess
end

end

% plot data
mom_fluxASCE=hASCE.*uASCE.^2;
if suppress_figs~=1
    figure(fig_ind)
    clf
    subplot(2,1,1)
    hold on
    plot(s_trans(runup_i),h_trans(runup_i),'r.','MarkerSize',20)
    plot(s_trans,hASCE+h_trans,'r')
    plot(dist_struct,z_struct_bathy,'g.','MarkerSize',20)
    plot(s_trans,h_trans)
    legend('Runup Point','EM Flow Elevation','Structure Location','Ground Elevation')
    xlabel('Distance along transect (m)')
    ylabel('Elevation (m)')
    title(title_txt)
    axis([s_trans(shore_i) s_trans(runup_i)+10 -1 30])

    subplot(2,1,2)
    hold on
    plot(dist_struct,0,'g.','MarkerSize',20)
    [AX,H1,H2] = plotyy(s_trans,uASCE,s_trans,mom_fluxASCE);
    legend('Structure Location','EM Speed (m/s)','EM Momentum Flux (m^3/s^2)')
    xlabel('Distance along transect (m)')
    set(AX(1),'XLim',[s_trans(shore_i) s_trans(runup_i)+10])
    set(AX(2),'XLim',[s_trans(shore_i) s_trans(runup_i)+10])
end

% Hydro values at Structure
flow_depth=interp1(s_trans,hASCE,dist_struct);
flow_elevation=interp1(s_trans,hASCE+h_trans,dist_struct);
flow_speed=interp1(s_trans,uASCE,dist_struct);
momentum_flux=interp1(s_trans,mom_fluxASCE,dist_struct);

```

check_transects.m

```
function [s_trans,z_trans,H_trans,runup_site_s,profile_check]=
check_transects(s_trans,z_trans,H_trans,site_s)
% Checks transect to see if any points along the transect have a higher
% elevation than the runup elevation. This situation creates problems with
% the EGL method, and must be avoided. If any locations have an elevation
% greater than the runup elevation, then these points are artificially
% lower to the runup elevation
%% inputs
% s_trans - distance vector along transect where s=0 is the offshore starting point
% z_trans - ground elevation vector along transect
% H_trans - simulated flow depth vector along transect
% site_s - site location distance along transect
%% outputs
% s_trans - distance vector along transect where s=0 is the offshore starting point
% z_trans - ground elevation vector along transect
% H_trans - simulated flow depth vector along transect
% site_s - site location distance along transect
% runup_site_s - the runup at the inundation limit along transect
% profile_check - if ==0 profile needed no modification, if ==1 then profile needed modification
%%

% checking transects
% find runup point to the right (inland) of site
i_site=find(s_trans>=site_s,1); % site index
runup_site_i=length(s_trans); % init runup limit index at end of transect
for i=i_site:length(s_trans) % search for inundation limit
    if H_trans(i)<=0
        runup_site_i=i;
        break
    end
end

runup_site_s=s_trans(runup_site_i); % distance to inundation limit
runup_site_z=z_trans(runup_site_i); % ground elevation at inundation limit, runup

% search profile, see if points need to be lowered
profile_check=0;
for i=1:runup_site_i
    if z_trans(i)>runup_site_z
        profile_check=1;
        z_trans(i)=runup_site_z; % lower site to runup elevation
        H_trans(i)=max(H_trans(i),0.1); % create small flow depth if site is dry in simulation
    end
end

% display message if transect needed fixing
if profile_check==1
    disp('Transect has dry points between shoreline and site. Lowering ground')
    disp('elevation of these dry points to runup elevation landward of site.')
end
```

create_transects.m

```
function [s_trans,z_trans,H_trans,site_s,site_z]=
create_transects(xtc,yc,lon,lat,bathytopo,flowdepth,xs,ys,n_trans)

% Creates a transect with n_trans points of bathy and flowdepth from points in xtc and ytc
% Requires deg2utm.m function in same directory or path-linked
%% inputs
% xtc - longitude coordinates of transect
% ytc - latitude coordinates of transect, should be same size as xtc
% lon - longitude vector of database grid file
% lat - latitude vector of database grid file
% bathytopo - database file containing bathy/topo data, should be size(length(lat),length(lon))
% flowdepth - database file containing simulated flow depth data, should be
size(length(lat),length(lon))
% xs - site longitude
% ys - site latitude
% n_trans - number of points to make transect, typically large >1000
%% outputs
% s_trans - distance vector along transect where s=0 is the offshore starting point,
size(n_trans)
% z_trans - ground elevation vector along transect, size(n_trans)
% H_trans - simulated flow depth vector along transect, size(n_trans)
% site_s - site location distance along transect
% site_z - site elevation
%%

range_lon=max(xtc)-min(xtc);
range_lat=max(yc)-min(yc);

if range_lon>=range_lat
    dx_trans=range_lon/n_trans;
    lon_trans=[min(xtc):dx_trans:max(xtc)];
    lat_trans=interp1(xtc,yc,lon_trans);
else
    dx_trans=range_lat/n_trans;
    lat_trans=[min(yc):dx_trans:max(yc)];
    lon_trans=interp1(yc,xtc,lat_trans);
end

z_trans=interp2(lon,lat,bathytopo,lon_trans,lat_trans);

H_trans=interp2(lon,lat,flowdepth,lon_trans,lat_trans);

[x_trans,y_trans,~] = deg2utm(lat_trans,lon_trans);
s_trans=sqrt( (x_trans-x_trans(1)).^2+ (y_trans-y_trans(1)).^2 )';

[xs_m,ys_m,~] = deg2utm(ys,xs);
site_s=sqrt( (xs_m-x_trans(1)).^2+ (ys_m-y_trans(1)).^2 );

if xtc(1)>xtc(length(xtc))
    site_s=s_trans(length(s_trans))-site_s;
    s_trans=-fliplr(s_trans);
    s_trans=s_trans-s_trans(1);
    z_trans=fliplr(z_trans);
    H_trans=fliplr(H_trans);
end

site_z=interp1(s_trans,z_trans,site_s);
```

load_database_files.m

```
% Script file to load all the HK Thio's simulation output, and convert to a
% format easily used by the transect tool.

fclose all
clear all
clf

% names of netCDF files used for Pacific bathy/topo, not simulation output files
fname_map={'AK_etopo.nc';
           'CA1_crm.nc';
           'CA2_crm.nc';
           'CA3_crm.nc';
           'HI1_crm.nc';
           'HI2_crm.nc';
           'OR_crm.nc';
           'WA_crm.nc'};

numfname_map=size(fname_map);
numfname_map=numfname_map(1);

% get listing of Thio's map files in the current directory, write to dir.txt
! dir *.xyz /B > dir.txt

% open map file listing, load to file
fileID = fopen('dir.txt');
fname_TD=textscan(fileID,'%s');
fclose(fileID);

numfname=size(char((fname_TD{1}{:})));
numfname=numfname(1);

reload=1; % =1 to reload all datafiles and convert to mat (this is time consuming)

if reload==1
    for ifname=1:numfname
        fname=char(fname_TD{:}{ifname})
        fname_mat=[fname(1:length(fname)-3) 'mat'];

        if exist(fname_mat,'file')==0 % if the convert Matlab mat file doesnt already exist,
create it

            clear data
            data=load(fname);

            [a,b]=size(data);

            if b~=6 % data should have six columns
                fname
                error('Error, Expecting six columns')
            end

            latvec=data(:,2);

            for i=2:a
                if latvec(i-1)~= latvec(i)
                    n=i-1;
                    break
                end
            end

            m=a/n;

            if mod(a,n)~=0 % data needs to be rectangular
                [a,n,m]
                error('Error, Expecting regular matrix m x n')
            end

            lon=data(1:n,1); % first column lon
    end
end
```

```

lat=data(1:n:a-1,2); % second column lat
flowdepth=reshape(data(:,3),n,m); % third column H
flowvelocity=reshape(data(:,4),n,m); % fourth column speed
momflux=reshape(data(:,5),n,m); % fifth column momentum flux
bathytopo=reshape(data(:,6),n,m); % sixth column bathymetry and topography data

clf
pcolor(lon,lat,flowdepth)
shading interp
caxis([0 50])
hold on

% find bounding coordinates for each grid
nx=length(lon);
ny=length(lat);

box_coords(ifname,:)=[lon(1) lon(nx) lat(1) lat(ny)];

% find runup points
count=0;
clear runup_ts
for i=2:nx-1
    for j=2:ny-1
        if flowdepth(j,i)>0
            if min(min(flowdepth(j-1:j+1,i-1:i+1)))<=0
                count=count+1;
                runup_ts(count,:)=j,i,lon(i),lat(j),flowdepth(j,i),bathytopo(j,i)];
            end
        end
    end
end
plot(runup_ts(:,3),runup_ts(:,4),'r.')

% find shoreline points
count=0;
clear shoreline_ts
for i=2:nx-1
    for j=2:ny-1
        if bathytopo(j,i)>0
            if min(min(bathytopo(j-1:j+1,i-1:i+1)))<=0
                count=count+1;
            end
        end
    end
end
shoreline_ts(count,:)=j,i,lon(i),lat(j),flowdepth(j,i),bathytopo(j,i)];
end
plot(shoreline_ts(:,3),shoreline_ts(:,4),'y.')

fname_mat=[fname(1:length(fname)-3) 'mat'];
save(fname_mat,
'lon','lat','flowdepth','flowvelocity','bathytopo','momflux','runup_ts','shoreline_ts');
else
    load(fname_mat,'lon','lat')
    box_coords(ifname,:)=[lon(1) lon(length(lon)) lat(1) lat(length(lat))];
end
pause(.1)
end

save box_coords.mat box_coords fname_TD
end

%%%%%%%%%%%%%%%%%%%%%%%%%%%%%%%%%%%%%%%%%%%%%%%%%%%%%%%%%%%%%%%%%%%%%%%%

plot_all=1; % plot all grids

if plot_all==1
    figure(1)
    clf

    surf_int=10;

    for ifname=1:numfname_map

```

```

fname=char(fname_map(ifname,1))

lat_crm=ncread(fname,'lat');
lon_crm=360+ncread(fname,'lon');
bathytopo_crm=ncread(fname,'Band1');

contour(lon_crm,lat_crm,bathytopo_crm,[0 0],'r')
hold on
end

for ifname=1:numfname
fname=(fname_TD){ifname}
fname_mat=[fname(1:length(fname)-3) 'mat'];
load(fname_mat,'lon','lat','bathytopo')
nx=length(lon);
ny=length(lat);
pcolor(lon(1:surf_int:nx),lat(1:surf_int:ny),bathytopo(1:surf_int:ny,1:surf_int:nx))
shading interp
caxis([0 50])

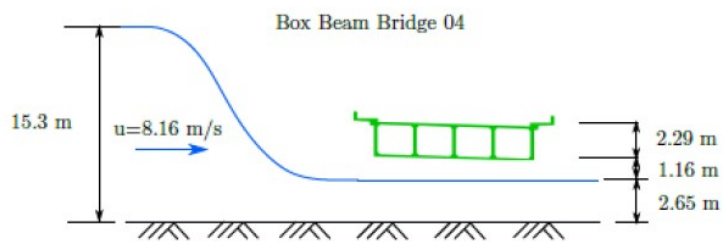
%
% axis([235.4 236.3 41.5 46.5])
pause(.1)
hold on
end

axis equal
savefig('TsunamiGrids.fig')
end

```


APPENDIX B: EXAMPLE BRIDGE LOADING CALCULATIONS

Bridge Bb04



Units for calculations

```
In [42]: kN = 1.0
          m = 1.0
          s = 1.0

          g = 9.81*m/s**2
          N = kN/1000.0
          kg = N*s**2/m

          ft = m/3.28
          kip = kN/0.225
```

Superstructure dimensions

The source code for the developed program is provided here, in entirety.

```

In [43]: db = 2.29*m
         hg = 3.81*m
         bd = 5.82*m

         h = 2.65*m # standing water level

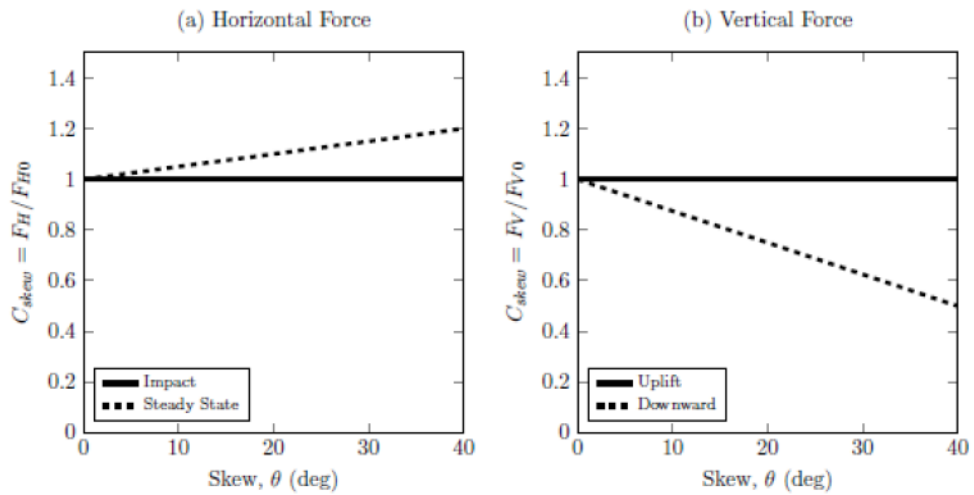
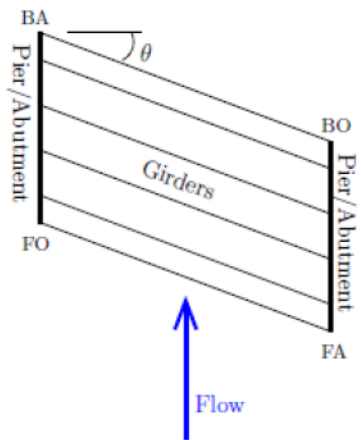
         A = 4.34*m**2

         skew = 20
         superelev = -2

         Cd = 2.0
         rho = 1040*kg/m**3

```

Factors for skew

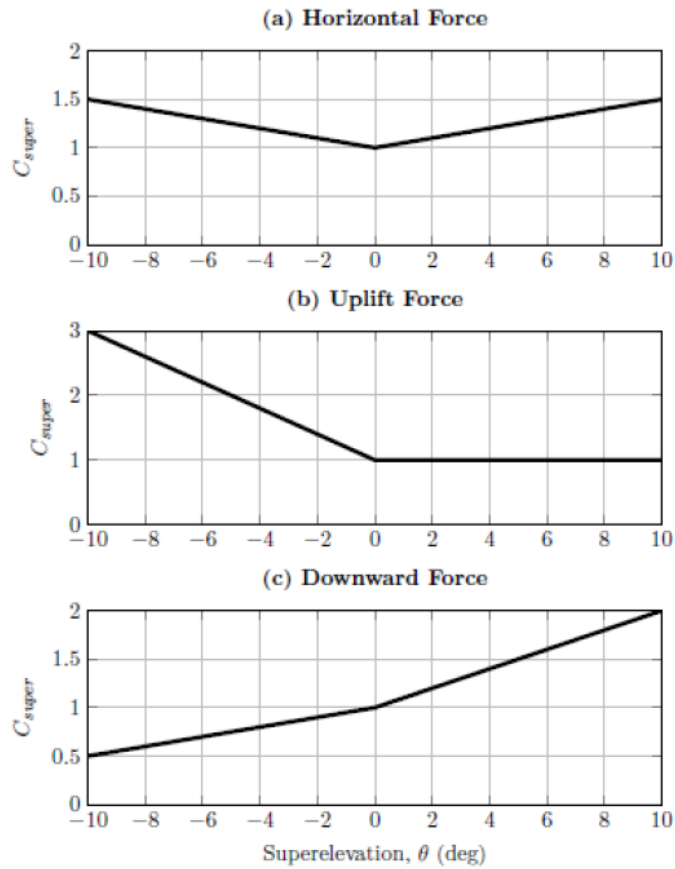
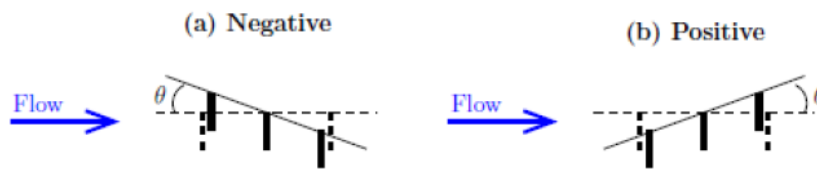


```
In [44]: def CskewFactors (angle):
         angle = abs(angle)

         Himpact = 1.0
         Hsteady = 1.0+angle*0.2/40
         Uplift = 1.0
         Downward = 1.0-angle*0.5/40

         return [Himpact,Hsteady,Uplift,Downward]
```

Factors for superelevation



```
In [45]: def CsuperFactors (angle):
Himpact = 1.0+abs(angle)*0.5/10
Hsteady = Himpact
if angle > 0.0:
    Uplift = 1.0
    Downward = 1.0+angle*1.0/10
else:
    Uplift = 1.0-angle*2.0/10
    Downward = 1.0+angle*0.5/10

return [Himpact,Hsteady,Uplift,Downward]
```

Small debris factor (applied to horizontal loads only)

```
In [46]: def Cdebris():
return 1.06
```

Static component of horizontal load

```
In [47]: def FHstatic (rho, db, hg, eta):
global g

h0 = eta-hg

if h0 < db:
    return 0.5*rho*g*h0**2
else:
    return 0.5*rho*g*(2*h0-db)*db
```

Dynamic component of horizontal load (with unit value for drag coefficient, i.e., Cd=1)

```
In [48]: def FHdynamic (rho, db, hg, eta, u):
h0 = eta-hg
Cd = 1.0

if h0 < db:
    return 0.5*Cd*rho*h0*u**2
else:
    return 0.5*Cd*rho*db*u**2
```

Static component of uplift load

```
In [49]: def FUstatic (rho, A):
         global g
         return rho*g*A
```

Dynamic component of uplift load

```
In [50]: def FUdynamic (rho, bd, u):
         return 0.5*rho*bd*u**2
```

Static component of downward load

```
In [51]: def FDstatic (rho,bd,hg,eta):
         global g
         h0 = eta-hg
         return rho*g*h0*bd
```

Factors for skew and superelevation

```
In [52]: Cskew = CskewFactors(skew)
         Csuper = CsuperFactors(superelev)
```

Loading coefficients for box bridges

```
In [53]: # Horizontal Load and impact
         C1 = 0.77
         C2 = 0.46
         Cimpact = 2.5

         # Uplift Load
         C3 = 1.0
         # C4 will be computed from C5 and C6
         C5 = 0.5
         C6 = 0.65
```

Maximum flow depth and speed from PTHA

```
In [54]: etamax = 15.3*m
         umax = 8.16*m/s
```

Load Cases

```
In [55]: # Load Case 1
#u = umax
#eta = 0.67*etamax

# Load Case 2
u = 0.8*umax
eta = etamax

# Load Case 3 (consider with large debris, Fdebris)
#u = 0.5*umax
#eta = 0.5*etamax
```

Horizontal Steady State Load

```
In [56]: FHs = FHstatic(rho,db,hg,eta)
FHD = FHdynamic(rho,db,hg,eta,u)

FH0 = C1*FHs + C2*FHD

FH = Cskew[0]*Csuper[0]*Cdebris()*FH0

print('Horizontal Steady State Load, FH = %.1f kip/ft' % (FH/(kip/ft)))
```

Horizontal Steady State Load, FH = 16.8 kip/ft

Horizontal Impact Load

```
In [57]: FHi = Cimpact*FH

print('Horizontal Impact Load, FHi = %.1f kip/ft' % (FHi/(kip/ft)))
```

Horizontal Impact Load, FHi = 41.9 kip/ft

Uplift Load

```
In [58]: FUs = FUstatic(rho,A)
FUd = FUs*(1+u)

h0 = eta-hg
C4 = C5*(h0/(hg-h))*C6

FU0 = C3*FUs + C4*FUd

FU = Cskew[2]*Csuper[2]*FU0

print('Uplift Load, FU = %.1f kip/ft' % (FU/(kip/ft)))
```

Uplift Load, FU = 31.7 kip/ft

Downward Load

```
In [59]: FDs = FDstatic(rho,bd,hg,eta)
FD0 = FDs

FD = Cskew[3]*Csuper[3]*FD0

print('Downward Load, FD = %.1f kip/ft' % (FD/(kip/ft)))
```

Downward Load, FD = 31.6 kip/ft

APPENDIX C: DEFINITIONS AND NOTATIONS

DEFINITIONS AND NOTATIONS

B : variable used for the topography or bathymetry elevation, given relative to a specified datum, typically either NAVD88 or Mean High Water for tsunami modeling

E : hydraulic head (units of length) in the tsunami flow, or the sum of potential and kinetic energy in the tsunami.

F_r : Froude number; a dimensionless number which indicates the relative water particle speed to the speed of the wave. A Froude number of 1.0 or greater indicates the water is moving faster than the wave, and breaking is likely occurring.

g : gravitational acceleration; assumed constant $9.81 \text{ m}^2/\text{s}$

h : the fluid depth; a flow thickness measured from the solid bottom boundary to the free water surface

n : Manning's "n"; a roughness factor used in the estimation of bottom friction

R : tsunami runup, or the vertical elevation of land at the maximum extent of tsunami inundation; not equal to the maximum flow thickness over land, which may be either larger or smaller than the runup. At the point of maximum runup, the flow thickness is zero.

u, v : the water particle velocities, measured in the x- and y-directions, respectively. In the context of tsunami modeling, these are depth-averaged velocities, and so are not a function of the vertical coordinate